André Leonide

SOFC Modelling and Parameter Identification by means of Impedance Spectroscopy

André Leonide

**SOFC Modelling and Parameter Identification
by means of Impedance Spectroscopy**

Schriften des Instituts für Werkstoffe der Elektrotechnik,
Karlsruher Institut für Technologie
Band 18

SOFC Modelling and Parameter Identification by means of Impedance Spectroscopy

by
André Leonide

KIT Scientific Publishing

Karlsruher Institut für Technologie

Fakultät für Elektrotechnik und Informationstechnik, 2010

SOFC Modelling and Parameter Identification

by means of Impedance Spectroscopy

Zur Erlangung des akademischen Grades eines

DOKTOR-INGENIEURS

von der Fakultät für

Elektrotechnik und Informationstechnik

der Universität Karlsruhe (TH)

genehmigte

DISSERTATION

von

Dipl.-Ing. André Leonide

geb. in: Karlsruhe

Tag der mündlichen Prüfung: 10.02.2010

Hauptreferentin: Prof. Dr.-Ing. Ellen Ivers-Tiffée

Korreferent: Prof. Dr. rer. nat. Detlev Stöver

meinen Eltern

Danksagung

Die vorliegende Doktorarbeit entstand während meiner Forschungstätigkeit am Institut für Werkstoffe der Elektrotechnik der Universität Karlsruhe (TH). An erster Stelle gilt mein Dank der Institutsleiterin Frau Prof. Ellen Ivers-Tiffée für die stete Betreuung meiner Arbeit und die Förderung meiner beruflichen Entwicklung. Für das Interesse an meiner Arbeit und die Übernahme des Korreferats bedanke ich mich vielmals bei Herrn Prof. Detlev Stöver vom Forschungszentrum Jülich.

All meinen ehemaligen studentischen Mitarbeitern gilt mein Dank für ihr Engagement und die ausgezeichnete Zusammenarbeit. Ferner bedanke ich mich bei allen Institutsangehörigen für ihre Unterstützung und das angenehme Arbeitsklima.

Ein außerordentlicher Dank gilt meinen Eltern und Geschwistern, die mich stets mit allen Kräften unterstützt haben.

André Leonide

Karlsruhe, im Juli 2010

.

Zusammenfassung

Das Interesse an Festelektrolytbrennstoffzellen (SOFC), die potentiell effiziente Energieerzeugung mit flexibler Brenngaszusammensetzung koppeln, hat in den letzten Jahren deutlich zugenommen. Zu den wichtigsten Entwicklungszielen zählt natürlich neben der Langzeitbeständigkeit die Leistungsfähigkeit der Einzelzellen, welche von drei Verlustmechanismen bestimmt wird: (i) ohmsche Verluste, (ii) Polarisationsverluste durch Gasdiffusion und (iii) Verluste durch Aktivierungspolarisation.

Bis Heute ist eine gezielte Weiterentwicklung von anodengestützten SOFCs (ASC) durch ein unvollständiges Verständnis des physikalischen Ursprungs der einzelnen Verlustprozesse und deren Beitrag zum Innenwiderstand der Zelle erschwert worden.

Deshalb war das vorrangige Ziel der vorliegenden Dissertation die eindeutige Identifikation und gleichzeitige physikalische Interpretation aller in einer anodengestützten Zelle ablaufenden Polarisationsprozesse.

Im Folgenden wird eine Zusammenfassung der maßgeblichen Ergebnisse gegeben.

Entwicklung eines Ersatzschaltbildmodells (Kapitel 4.1)

ASC-Einzelzellen wurden mittels Impedanzspektroskopie charakterisiert. Eine hochauflösende Messdatenauswertung ermöglichte eine eindeutige Identifizierung aller zum Gesamtwiderstand der Einzelzelle beitragenden Verlustprozesse. Durch eine gezielte Analyse der Verteilungsfunktionen der Relaxationszeiten (DRT) bei gleichzeitiger Variation der Betriebsbedingungen war es möglich bis zu fünf Verlustprozesse zu identifizieren. Zwei Prozesse sind der Kathode zuzuschreiben (P_{1C}, P_{2C}). P_{1C} beschreibt die Gasdiffusionsverluste in den Poren des Kathodenmaterials. Der schnellere Prozess von beiden (P_{2C}) ist elektrochemischer Natur, und beschreibt den Sauerstoffeinbau und -Transport im Kathodenfestkörper der gemischtleitenden Kathode (LSCF). Drei Prozesse können der Anode zugeordnet werden (P_{1A}, P_{2A}, P_{3A}). P_{1A} wird durch die Gasdiffusionshemmung innerhalb der Poren des Ni/YSZ Anodensubstrates hervorgerufen. Die beiden höherfrequenten Prozesse P_{2A} und P_{3A} stehen im Zusammenhang mit dem Ladungstransferwiderstand bei der Elektrooxidation des Wasserstoffes, dem Ladungstransport in der Ni/YSZ – Anodenstruktur und der Gasdiffusion in der Anodenfunktionsschicht.

<u>Ermittlung von Diffusions- und Oberflächenaustauschkoeffizienten (Kapitel 4.2)</u>

Das in der vorliegenden Arbeit entwickelte elektrische Ersatzschaltbildmodell wurde zur Bewertung der Leistungsfähigkeit von gemischtleitenden Kathodenmaterialien des Typs $(La_x,Sr_{1-x})(Co_y,Fe_{1-y})O_{3-\delta}$ eingesetzt. Es wurde erstmals gezeigt, dass die chemischen Oberflächenaustausch- und Diffusionskoeffizienten (k^δ und D^δ) dieses Materialtyps direkt aus Impedanzmessungen an ganzen anodengestützten Einzelzellen (ASC-Einzelzellen) ermittelt werden können. Voraussetzung war die Identifikation des Gerischer-Impedanzbeitrags durch eine kombinierte DRT- und CNLS-Analyse (vgl. Kapitel 4.1). Auf diese Weise konnten der Flächenspezifische Widerstand (R_{chem}) und die charakteristische Zeitkonstante (t_{chem}), die in Zusammenhang mit der Oberflächenkinetik und den Ladungstransporteigenschaften der entsprechend Materialien stehen, ermittelt werden. k^δ und D^δ wurden, schließlich, aus R_{chem} und t_{chem} unter Verwendung notwendiger thermodynamischer und mikrostruktureller Parameter (ε, a_S, τ_s, c_O, c_{mc}, γ_{TD}) ermittelt.

Die Unsicherheit bei der Berechnung des Oberflächenaustauschkoeffizienten k^δ sind hauptsächlich auf den großen Fehlerbereich der effektiven Oberflächendichte (a [m/m^3]) zurückzuführen. Jedoch lassen neueste Entwicklungen auf dem Gebiet der Mikrostrukturmodellierung von Elektroden für Festelektrolytbrennstoffzellen [12, 13, 26, 27] vermuten, dass in näherer Zukunft die erforderlichen Strukturparameter mit viel größerer Genauigkeit ermittelt/abgeschätzt werden können.

Andererseits ist der Fehler bei der Berechnung des Diffusionskoeffizienten D^δ fast ausschließlich auf die Ungenauigkeit bei der Bestimmung des thermodynamischen Faktors γ_{TD} zurückzuführen.

In der vorliegenden Dissertation wurde die entwickelte Methode auf zwei alternative Materialzusammensetzungen (L68SCF: La-reich, und LSF: ohne Co) angewendet und mit Ergebnissen an $La_{0.58}Sr_{0.4}Co_{0.2}Fe_{0.8}O_{3-\delta}$ (L58SCF) Standard-Kathoden, verglichen. Die letzteren weisen im Betrieb bei 750°C eine starke Erhöhung des Polarisationswiderstands auf (310 % in 700 h) [67].

Die dabei erzielten Ergebnisse bestätigen, dass die ungealterte Standardkathode (L58SCF) den kleinsten flächenspezifischen Widerstand (ASR) besitzt. Jedoch, ist dieser nach 700 h doppelt so hoch wie der ASR der ungealterten LSF Kathode. Im Gegensatz dazu, ist der ASR der L68SCF Kathode ca. 30% höher als der, der bereits gealterten L58SCF Kathode.

Dies lässt die Vermutung zu, dass die hier untersuchte LSF-Zusammensetzung als Kathode für eine IT-SOFC in Frage kommen könnte. Eine endgültige Aussage darüber können, jedoch, nur zukünftige Langzeitexperimente liefern.

Die Auswertung der ermittelten k^δ und D^δ Werte ergab u. A. folgende Erkenntnisse:

1. Die starke Alterung der L58SCF Kathode ist hauptsächlich auf eine starke Abnahme des chemischen Diffusionskoeffizienten D^δ zurückzuführen (fast eine Dekade).

2. Die hohen Aktivierungsenergien der ASRs (1.8 eV für LSF und 1.69 eV für L68SCF) ergeben sich durch die außergewöhnlich hohen Aktivierungsenergien (> 2.46 eV) der entsprechenden Diffusionskoeffizienten D^δ.

3. Die anfänglich niedrigere Leistungsfähigkeit von LSF und L68SCF, verglichen mit L58SCF, ist hauptsächlich auf die niedrigeren D^δ-Werte zurückzuführen.

Zudem birgt dieser Ansatz das Potential, Alterungsphänomene, die durch eine Veränderung der Mikrostruktur und/oder der chemischen Zusammensetzung hervorgerufen werden, direkt an „realen" Kathoden (im Zellverbund der ASC-Einzelzelle) zu identifizieren.

<u>Modellierung des Stationären Verhaltens (Kapitel 4.3)</u>

Es wurde ein nulldimensionales stationäres Modell zur Vorhersage des Strom/Spannungsverhaltens von planaren anodengestützten SOFC Einzelzellen entwickelt. Die Simulationsresultate wurden mittels experimentell aufgenommenen Strom/Spannungskennlinien validiert. Die Messungen erstreckten sich über einen Bereich von 621°C bis 821°C, Stromdichten bis zu 2 A/cm^2 und Betriebsspannungen nicht unterhalb von 0.6 V. Dem entwickelten Modell liegen die Butler-Volmer-Gleichung zur Bestimmung der Aktivierungspolarisation und das Fick'sche Model mit der Berechnung der Strukturparameter (Ψ_{an} und Ψ_{cat}) zur Bestimmung der Diffusionspolarisation und das Ohmsche Gesetz zur Bestimmung der ohmschen Überspannung zugrunde. Die benötigten Modellparameter, mit Ausnahme der Ladungstransferkoeffizienten α_{an} und α_{cat}, wurden aus Impedanzmessungen im Leerlauf bestimmt, die unter gezielt variierten Betriebsbedingungen, wie Brenngas-Zusammensetzung an der Anode, Oxydationsgas-Zusammensetzung an der Kathode sowie Temperatur, durchgeführt wurden.

Die aufgenommenen Impedanzkurven wurden mittels des, in dieser Arbeit, entwickelten detaillierten Ersatzschaltbildmodells angepasst. Mit Hilfe der so erhaltenen Widerstände konnten durch Anpassung von semi-empirischen Modellgleichungen (Potenzansatz) die Partialdruck- und Temperatur-Abhängigkeit der kathodischen und anodischen Austauschstromdichte bestimmt werden. So konnten erstmals die Parameter a und b, die die Exponenten der Partialdruckabhängigkeit von H_2 und H_2O der anodenseitigen Austauschstromdichte darstellen, unabhängig voneinander bestimmt werden. Ebenso wurde der Parameter m, der den Exponenten für die Sauerstoffpartialdruckabhängigkeit der kathodenseitigen Austauschstromdichte darstellt, erhalten. Die Ladungstransferkoeffizienten wurden abweichend durch Impedanzmessungen unter Last und durch Anpassung der BV-Gleichung an die so erhaltenen stromabhängigen Aktivierungsüberspannungen bestimmt. Durch die Verwendung der Parameter a, b und m (a = -0.10, b = 0.33, m = 0.22),

α_{an} und α_{cat} (α_{an} = 0.590, α_{cat} = 0.650) sowie der temperaturabhängigen Vorfaktoren γ_{an} und γ_{cat} (γ_{an} = 1.82527·10^6·T A/m^2, γ_{cat} = 1.51556·10^8·T A/m^2) ermöglicht das Modell eine bessere Vorhersage der Aktivierungspolarisation über einen weiten Temperatur- und Gaszusammensetzungsbereich. Im analysierten Temperaturbereich (621-821 °C) und für alle Stromdichten, liegt die Abweichung Δ zwischen simulierter und gemessener Strom/Spannungskennlinie innerhalb der folgenden Grenzen: 0.01 % ≤ Δ ≤ 4.75 %.

Im Unterschied zu anderen bekannten Modellierungsansätzen gelingt so die getrennte Betrachtung aller einzelnen Verlustanteile (diffusive und elektrochemische an der Anode/Kathode oder ohmsche) im gesamten Strombereich ohne die Notwendigkeit von pauschal abgeschätzten Parametern. Damit kann das Optimierungspotential einer Zelle für jeden beliebigen Arbeitspunkt beurteilt werden, oder unterschiedliche Zellen an einem bestimmten Arbeitspunkt miteinander verglichen werden. Außerdem unterstützen die identifizierten Parameter (siehe Tabelle 12) und Modellgleichungen künftige Systemmodellierungsaufgaben.

Das Modell liefert allerdings nur unter der Vorraussetzung einer konstanten Stromdichte- und Temperaturverteilung über der aktiven Elektrodenfläche eine genaue Vorhersage, so dass für die Impedanzmessung kleine Zellen (1cm^2-Elektroden) erforderlich sind. Nach bisherigen Erfahrungen sind insgesamt etwa 25 Impedanzmessungen unter Variation der Betriebsparameter Temperatur und Brenngaszusammensetzung erforderlich.

In einem weiteren Schritt soll das Modell auf den Reformatbetrieb angewandt werden, dazu sind weitere Impedanzmessungen mit CO/CO_2 und H_2/H_2O geplant.

Außerdem soll das Modell zukünftig zur Vorhersage der Leistungsdaten von größeren Einzelzellen (Stack-„repeating units") eingesetzt werden. Dazu muss das Modell auf ein zweidimensionales erweitert werden, um die ortsabhängige Stromdichte und die daraus resultierende Temperaturverteilung in der Zellebene mitberücksichtigen zu können.

Table of Contents

1   Introduction

Interest in solid oxide fuel cells (SOFC), which combine potentially efficient energy production with flexible fuel composition, has significantly increased in the past few years. Amongst the most important development goals is, besides long-term stability, the single-cell performance which is limited by three loss mechanisms: (i) ohmic losses, (ii) polarisation losses through gas diffusion, and (iii) losses by activation polarisation.

In planar cells, the main part of ohmic losses is due to the solid electrolyte. Here, 8 mol% yttria-doped ZrO_2 (8YSZ) [1-3] still is the state-of-the-art material, its ionic conductivity lies at $\sigma = 5$ S/m at 800 °C [4]. Unlike electrolyte-supported cells where the electrolyte thickness takes on values of up to 200 μm, the electrolyte thickness in anode-supported cells (ASC) usually is only around 10 μm. Therefore, the ohmic resistance can be reduced e.g. at 800 °C in ASCs to theoretically 0.020 $\Omega \cdot cm^2$; even at 600 °C its value of 0.176 $\Omega \cdot cm^2$ still renders cell operation possible. However, the ohmic resistance increases due to the need of an additional layer (Gd-doped CeO_2) when mixed ionic-electronic conducting (MIEC) cathode materials are introduced (cf. chapter 3.1).

During the last decade, continuous advancement of ASCs led to a multi-layer structure of nickel/yttria-stabilised zirconia (Ni/YSZ) substrate (250 to 1500 μm thickness), Ni/YSZ functional layer (anode, 5 to 25 μm thickness), YSZ electrolyte (10 μm), GDC (Gd-doped CeO_2) interlayer (1 to 10 μm) and a mixed-conducting cathode of LSCF $((La_x,Sr_{1-x})(Co_y,Fe_{1-y})O_{3-\delta}$, 25 to 50 μm) with an overall area-specific resistance of less than 0.15 $\Omega \cdot cm^2$ at 800 °C, which corresponds to a maximum power density of more than 2 W/cm^2 in wet (3 % H_2O) hydrogen [5]. In the temperature range between 600 °C and 800 °C, however, activation and diffusion polarisation effects significantly become more important.

The activation polarisation, determined by the activation energy barrier, depends on the structural and catalytic properties of the electrocatalyst/electrolyte couple. These properties can be calculated using the Butler-Volmer equation that considers the current-voltage characteristics (I-U characteristics) for both forward and reverse reaction. To this end, the exchange current densities at the anode and cathode side must be known, as well as the charge transfer coefficient. The exchange current densities are usually determined on symmetrical cells (half-cells) for anode and cathode separately, this approach is valid for electrolyte-supported planar cells within certain limitations. This procedure is not applicable for anode-supported planar cells because identical electrode structures cannot be achieved in a symmetrical cell based on a thin-film electrolyte.

Diffusion polarisation results from gas transport in a flow-field and within a porous electrode structure; in particular, the microstructure of the according (multi-layer, multi-component) electrode plays a decisive role. Diffusion polarisation is generally evaluated by applying Fick's law, thereby considering electrode porosity (ε_p) and tortuosity ($\tau_{tortuosity}$) by the structural parameter $\psi_{an/cat} = \varepsilon_p / \tau_{tortuosity}$.

1.1 Goals of this Work

To this day, the progress for a further improvement of anode supported cells has been partly constrained by an incomplete understanding of the physical origin and share of the individual polarisation processes controlling the cell performance.

The electrochemical impedance spectroscopy (EIS) is one of the most promising methods for unfolding complex electrochemical systems such as a SOFC [6].

Commonly the obtained impedance spectra are analysed by a Complex Nonlinear Least Squares (CNLS) approximation to a model function represented by an equivalent circuit [7]. In this case the equivalent circuit model needs to be defined a priori without any knowledge about the real number of polarisation processes contributing to the overall polarisation loss of the cell. This leads very often to a severe ambiguity of the adopted model [6].

To overcome that disadvantage an alternative approach for analysing impedance spectra will be used in this work. The equivalent circuit model (ECM) and the optimal starting parameters for the CNLS algorithm shall be obtained by a pre-identification of the impedance response by calculating and analysing the corresponding distribution function of relaxation times (DRT).

The equivalent circuit obtained in this way shall be used to assess candidate cathode compositions with regard to the surface exchange kinetics and oxygen ion bulk diffusion, thus enabling the identification of the performance limiting factors.

Furthermore, the ECM should be able to deliver physical meaningful parameters for the development of a zero-dimensional stationary model, which is valid for a wide operating range.

1.2 Outline

In the following chapter 2 an introduction to the fundamentals needed to understand the core of this thesis is given.

Chapter 3 ("Experimental") describes: (i) the cell-design and material composition of the analysed ASC single cells, (ii) the measurement setup used for the electrochemical characterization, (iii) the operating parameter range over which the measurements were carried out, and (iv) the measurement-data-quality assessment of a typical impedance spectrum by applying the Kramers-Kronig relations.

Chapter 4 ("Results and Discussion") is the main chapter of this thesis. In the first part of this chapter the equivalent circuit model (ECM) of the ASC cells, analysed within this work, is developed. In the second part the developed ECM is applied to determine the surface exchange kinetics and oxygen ion bulk diffusion properties (k^δ and D^δ) of mixed ionic-electronic conducting (MIEC) cathodes, directly from electrochemical impedance spectroscopy (EIS) measurements on ASCs. The last part of chapter 4 presents a zero-dimensional stationary model for the current voltage (I-U) characteristics of the ASC.

A brief summary of the essential findings of this work is given in the last chapter 5.

2   Fundamentals

In the first part of this chapter the working principle of a SOFC is described. The loss mechanisms taking place in a SOFC and the resulting current-voltage (I-U) characteristic are discussed from a theoretical view of point.

The second part of the chapter gives a short introduction to the electrochemical impedance spectroscopy (EIS) measurement method. Thereafter, special impedance elements used to model the impedance response of the SOFC single cell analysed within this work are presented.

Finally, the complex non-linear least squares (CNLS) fitting procedure and the distribution of relaxation times (DRT) approach will be discussed.

## 2.1 Working Principle of Solid Oxide Fuel Cells (SOFC)

Fuel cells are galvanic elements, in which the reactants and the products are continuously supplied and removed [8, 9]. These devices convert the chemical energy contained in a fuel electrochemically into electrical energy. Hence in the case of an ideal loss-free fuel cell the change in Gibbs free energy (ΔG) of the underlying combustion reaction would be converted totally in electrical work. For Hydrogen (H_2) as fuel and oxygen (O_2) as oxidant gas, the ΔG of the overall reaction in the fuel cell (Eq. 2.1) is -228.59 kJ/mol at standard conditions (25 °C ,1 atm) [9].

$$\frac{1}{2}O_2(g)+H_2(g) \rightarrow H_2O(g) \qquad \text{Eq. 2.1}$$

Fig. 1 shows a simplified functional principle of a solid oxide fuel cell (SOFC). To prevent a direct combustion of the reactants, the fuel and oxidant gas compartments are separated by a gas-tight but oxygen ion (O^{2-}) conducting electrolyte membrane.

Two porous and electron conducting electrodes (cathode and anode) are applied on both sides of the electrolyte to allow an incorporation and removal of oxygen ions into and from the electrolyte material.

At the cathode O_2 is reduced to O^{2-} by taking up 2 electrons from the cathode material, which in consequence of this will become positively charged. Subsequently the oxygen ion is incorporated into the electrolyte (Eq. 2.2).

$$\frac{1}{2}O_2(g)+2e^- \rightarrow O^{2-}(\text{electrolyte})$$

Eq. 2.2
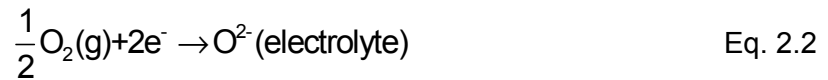
Due to the chemical potential difference between the cathode (high oxygen partial pressure 1 atm>pO_2>0.01 atm) and anode side (very low oxygen partial pressure, 10^{-13} atm>pO_2>10^{-27} atm) the oxygen ion diffuses through the electrolyte towards the anode [11]. At the anode O^{2-} reacts with H_2 forming water by releasing two electrons to the anode material (Eq. 2.3).

$$O^{2-}(\text{electrolyte})+H_2(g) \rightarrow H_2O(g)+2e^-$$

Eq. 2.3
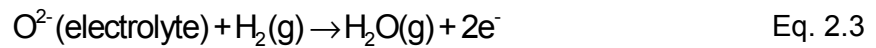
In the last step the electrons from the anode are driven back to the positively charged electrode (cathode) trough an external load thus performing electrical work.
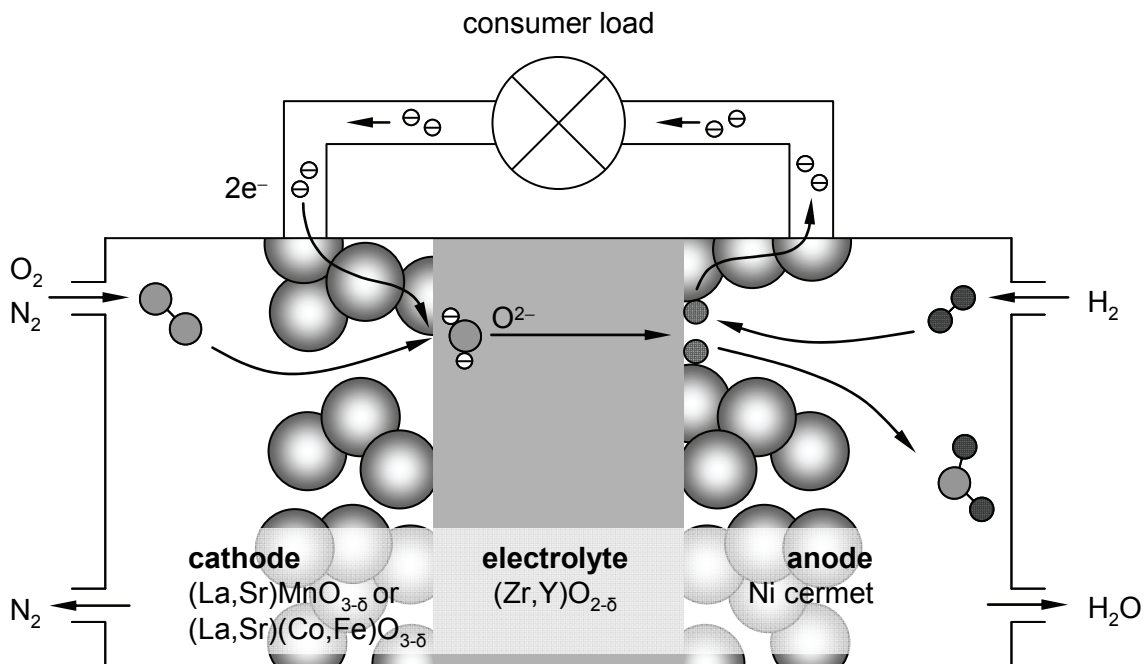
Fig. 1: Oxygen and fuel (here H_2) react via a dense, oxide ion-conducting electrolyte (e.g. yttria-doped zirconia, YSZ); the spatial separation of reduction and oxidation reaction enables the utilization of the electrons involved in the redox process [10].

However in the case of an open circuit, where electrons from the anode are not able to move back to the cathode, after some time an electrochemical equilibrium will be reached. Due to the separation of charge between anode and cathode an electric field force of opposite direction to the diffusion force, but of identical magnitude, will impede a further diffusion of oxygen ions. In this situation the Nernst-voltage U_N arises between cathode and anode [11]:

$$U_N = \frac{RT}{n_e F} \cdot \ln \sqrt{\frac{pO_{2,cat}}{pO_{2,an}}}$$ Eq. 2.4

where R is the universal gas constant, T the absolute temperature, F the Faraday constant, n_e the number of electrons involved in the reaction (n_e = 2 in the case of a SOFC) and pO_2 the respective oxygen partial pressure at the cathode and anode.

The Nernst-voltage can be equally calculated from Gibbs free energy by applying the following equation [11]:

$$U_N = -\frac{\Delta G(T)}{n_e F}$$ Eq. 2.5

ΔG is a function of operating conditions such as operating temperature T and partial pressures and can be written as [11]:

$$\Delta G(T) = \Delta G_0(T) + RT \ln\left(\frac{pH_2O_{an}}{\sqrt{pO_{2,cat}} \, pH_{2,an}} \right)$$ Eq. 2.6

where ΔG_0 is the temperature dependent standard free energy. By introducing Eq. 2.6 in to Eq. 2.5 the following formula for the hydrogen and water partial pressure dependent Nernst voltage is found [11]:

$$U_N = -\frac{\Delta G_0(T)}{n_e F} - \frac{RT}{n_e F} \ln\left(\frac{pH_2O_{an}}{\sqrt{pO_{2,cat}} \, pH_{2,an}} \right)$$ Eq. 2.7

In the typical operation range (600-950 °C) of a SOFC operated on hydrogen (with 1 % H_2O) and air as oxidant Eq. 2.7 gives values of U_N between 1.18 and 1.13 V.

2.2 Loss Mechanisms

When a fuel cell is loaded with an electric current the cell voltage drops bellow the thermodynamically predicted (Nernst-voltage). This is due to several internal irreversible loss mechanisms. In the following subchapters a short description of these losses will be given.

2.2.1 Ohmic Losses

Ohmic losses occur during the electronic or ionic transport through the electrodes and the electrolyte. The overall ohmic resistance is the sum of each individual ohmic contribution R_k. According to Ohm's law, the ohmic overpotential linearly increases with the current density j.

$$\eta_{ohm} = j \cdot \sum_k R_k = j \cdot R_{ohm}$$ Eq. 2.8

In planar cells, the main part of ohmic losses is due to the solid electrolyte. Here, 8 mol% yttria-doped ZrO_2 (8YSZ) [1-3] still is the state-of-the-art material, its ionic conductivity lies at $\sigma = 5$ S/m at 800 °C [4]. Unlike electrolyte-supported cells where the electrolyte thickness takes on values of up to 200 µm, the electrolyte thickness in anode-supported cells usually is only around 10 µm. Therefore, the ohmic resistance can be reduced e.g. at 800 °C in anode-supported cells to theoretically 0.020 $\Omega\cdot cm^2$, even at 600 °C its value of 0.176 $\Omega\cdot cm^2$ still renders cell operation possible. However, as will be shown later, the ohmic resistance increases due to the need of an additional layer (Gd-doped CeO_2) when mixed ionic-electronic conducting (MIEC) cathode materials are introduced (see Fig. 17 in chapter 3.1).

2.2.2 Activation Loss

Activation polarisation describes the electrochemical loss mechanisms taking place mainly at the three-phase boundary (TPB) where ionic-conducting, electronic-conducting and gas phase meet. An activation energy is necessary in order to overcome the energy barrier that prevents a spontaneous reaction. The higher the temperature, the higher the probability for reactants to gain the necessary activation energy, therefore the overpotentials are reduced. A commonly used equation for describing the influence of activation overpotential on current density is the well known Butler-Volmer equation [12].

$$j = j_{0,el}\left[\exp\left(\alpha_{el}\frac{n_e F \eta_{act,el}}{RT}\right) - \exp\left(-\left(1-\alpha_{el}\right)\frac{n_e F \eta_{act,el}}{RT}\right)\right] \qquad \text{Eq. 2.9}$$

Here, $j_{0,el}$ is the (partial pressure and temperature dependent) exchange current density of anode/cathode, n_e the number of exchanged electrons (in our case $n_e = 2$), α_{el} the apparent charge transfer coefficient, and $\eta_{act,el}$ the activation overpotential of the according electrode (anode or cathode). The charge transfer coefficient is an indicator of the symmetry of the activation energy barrier when a positive or negative overpotential is applied [13].

In this work the activation overpotential will be calculated separately for anode and cathode, in both cases using the Butler-Volmer equation (Eq. 2.9). The needed parameters $j_{0,el}$ and α_{el} will be obtained from impedance measurements conducted at open circuit condition and under current load (cp. chapter 4.3.1).

2.2.3 Diffusion Overpotential Loss

High current densities are correlated with an enhanced gas transport and gas conversion in the electrode, which leads to polarisation losses. The so-called diffusion polarisation at the anode results from an undersupply of the three-phase points with fuel. Simultaneously the reaction product (water) is being transported away from the reaction zone too slowly. At the

cathode, losses due to diffusion polarisation occur, too. They are caused by an undersupply with oxidizing gas.

Calculation of the diffusion polarisation overpotential is based on the Nernst-equation (Eq. 2.4), from which the following Eqs. 2.10 and 2.11 can easily be derived [14]:

$$\eta_{conc,an} = \frac{RT}{2F} \ln\left(\frac{pH_2O_{an}^{TPB} \cdot pH_{2,an}}{pH_2O_{an} \cdot pH_{2,an}^{TPB}} \right)$$

Eq. 2.10

$$\eta_{conc,cat} = \frac{RT}{4F} \ln\left(\frac{pO_{2,cat}}{pO_{2,cat}^{TPB}} \right)$$

Eq. 2.11

$\eta_{conc,el}$ (the subscript „el" refers to anode („an") and cathode („cat"), respectively) describes the overpotential resulting from a partial pressure difference between gas atmosphere and TPB. $pH_{2,an}$, pH_2O_{an} and $pO_{2,cat}$ [atm] are the known partial pressures of hydrogen, water and oxygen, respectively, in the gas channel. The unknown partial pressures at the TPB, $pH_{2,an}^{TPB}$, $pH_2O_{an}^{TPB}$, and $pO_{2,cat}^{TPB}$, are determined by applying Fick's first law and assuming a linear concentration gradient as a function of the current density j. In this way the following Eqs. 2.12 and 2.13, which relate the diffusion-based voltage drop $\eta_{conc,el}$ to the current density j, are obtained [15]:

$$\eta_{conc,an} = \frac{RT}{2F} \ln\left(\frac{1 + \dfrac{RTL_{an}}{2FD_{H_2O}^{eff} pH_2O_{an} P_0} \cdot j}{1 - \dfrac{RTL_{an}}{2FD_{H_2}^{eff} pH_{2,an} P_0} \cdot j} \right)$$

Eq. 2.12

$$\eta_{conc,cat} = \frac{RT}{4F} \ln\left(1 \Big/ \left(1 - \frac{RTL_{cat}(1 - pO_{2,cat}/P)}{4FD_{O_2}^{eff} pO_{2,cat} P_0} \cdot j \right) \right)$$

Eq. 2.13

L_{an} and L_{cat} denote the effective thickness of the diffusion layer on the anode and cathode side respectively. D_i^{eff} is the effective molecular diffusion coefficient, which is a function of the microstructural properties (pore-size, porosity and tortuosity) of the underlying diffusion layer (see chapter 4.3.1). P denotes the absolute pressure ($P = 1$ atm) and $P_0 = 101330$ Pa/atm represents a conversion factor from [atm] to [Pa].

2.3 Current/Voltage Characteristics

The effect of the different loss mechanisms, discussed above, on the actual voltage output of a real SOFC during loading is shown qualitatively in the following Fig. 2. As can be seen, even at open circuit condition the cell voltage (U_{OCV}) is less than the thermodynamically predicted Nernst-voltage U_{th}. The difference U_{th}-U_{OCV} is called the "Overpotential" (from the German "Überspannung" [11]). This first drop may be caused by different parasitic losses, like for example undesired electron leaks across the electrolyte or even not perfectly gastight electrolytes. These causes induce an unwanted fuel-utilization already at open circuit, thus lowering the Nernst voltage.
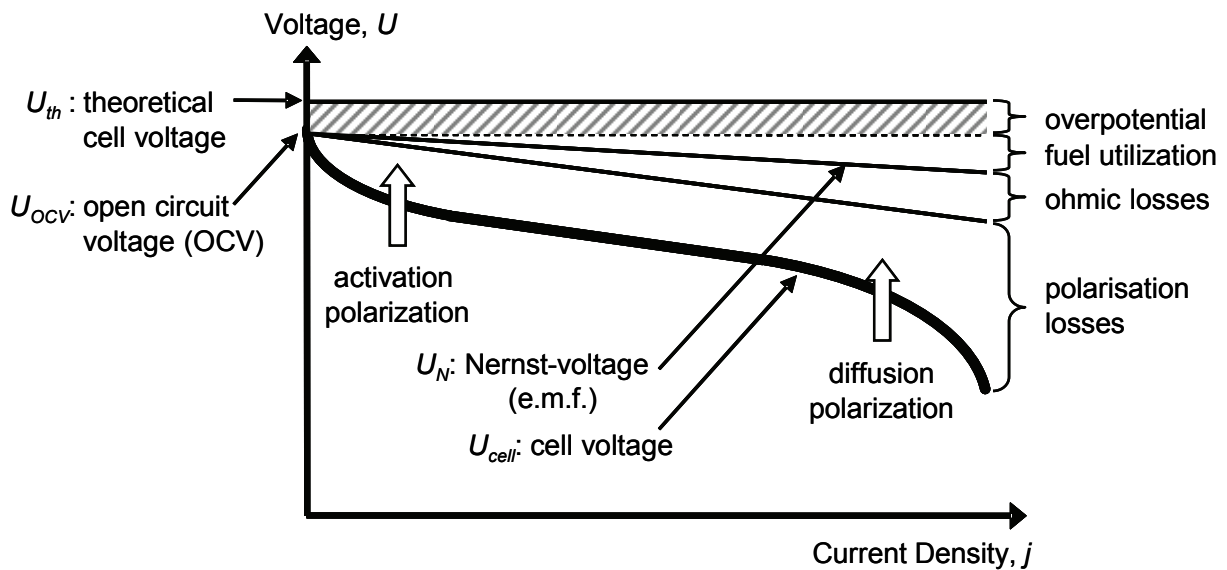
Fig. 2: Schematic plot of voltage versus current density of a SOFC showing different types of polarisations: activation polarisation is dominant at low current densities; diffusion polarisation is dominant at high current densities when the transport of reactive species to the electrolyte / electrode interface becomes a limiting factor for the cell reaction [16, 17].

A second cell voltage drop caused by the fuel utilization is the so-called gas conversion loss. An increasing current density results in an increased consumption of the fuel and oxidant gases. In the anode gas channel the hydrogen partial pressure decreases while the reaction product water increases. This results in an increasing oxygen partial pressure in the fuel gas mixture ($pO_{2,an}$). For the same reason the cathode gas becomes depleted in oxygen ($pO_{2,cat}$ decreases). As a consequence the Nernst-voltage U_N will decrease by increasing current density, following Eq. 2.4. U_N represents the driving force for the overall cell reaction and is therefore also called the "electromotive force" (e.m.f.) [11].

The two remaining losses responsible for the characteristic shape of the current voltage curve (I-U curve) depicted in Fig. 2 are the ohmic and polarisation losses. The polarisation loss is the sum of the activation and diffusion polarisation.

The strong (nonlinear) voltage drop at low current density is mainly caused by activation losses taking place at the TPB of both electrodes. In the medium current range the overall loss is dominated by the ohmic overpotential loss, therefore a more or less linear decrease of the cell voltage with increasing current density is observed. At high current densities, the voltage output of the fuel cell once again drops rapidly due to mass-transport limitations at the electrodes (gas diffusion polarisation).

2.4 Impedance Spectroscopy

In order to develop a physico-chemical model of SOFC single cells and to refine their efficiency and long term stability the performance-related polarisation processes have to be identified and proven. In contrast to I-U curves, where only the overall loss of a cell can be identified, the electrochemical impedance spectroscopy (EIS) is one of the most promising methods for unfolding complex electrochemical systems such as a SOFC.

The EIS method takes advantage from the fact that the polarisation loss mechanisms taking place in an electrochemical system differ in their characteristic time constant and frequency response.

The most common and standard approach to measure the dynamic behaviour (impedance) of an electrochemical system is by applying a sinusoidal current (or voltage) to the interface and measure the phase shift and amplitude, or real and imaginary parts, of the resulting voltage or (current).

Here it should be noted that an impedance is only defined for systems that satisfy the conditions of causality, linearity, and time-invariance. Although many systems, like SOFCs, are usually non-linear, linearity can be assumed when the magnitude of the applied current stimulus is small enough to cause a linear response [18].

In this work the fulfilment of the above mentioned preconditions was verified by applying the Kramers-Kronig relations (cp. Chapter 3.4).

The basic experimental arrangement for impedance measurement is shown in Fig. 3a. A sinusoidal current of small amplitude $i(t) = i_0\sin(\omega t)$ is superposed to a defined bias current I_{load} and the sinusoidal voltage response $u(t) = u_0(\omega)\sin[(\omega t + \varphi(\omega)]$ is measured (Fig. 3b). From the ratio between the complex variables of voltage and current the impedance is calculated as follows [19]:

$$\underline{Z}(\omega) = \frac{\underline{u}(t)}{\underline{i}(t)} = \frac{u_0(\omega)}{i_0}e^{j\varphi(\omega)} = |\underline{Z}(\omega)|e^{j\varphi(\omega)} = \mathrm{Re}\{\underline{Z}(\omega)\} + j\,\mathrm{Im}\{\underline{Z}(\omega)\} \qquad \text{Eq. 2.14}$$

Where $\omega = 2\pi f$ [s^{-1}] represents the angular frequency and $\varphi(\omega)$ the frequency dependent phase shift between voltage and current.

This measurement is generally performed for a discrete quantity of frequency values in a defined frequency range and the recorded impedance values are usually plotted in the complex plane. The resulting curve is also known as Nyquist-plot. Fig. 4 gives an example for a Nyquist plot measured on an anode supported SOFC single cell. The high frequency intercept (for $\omega \to \infty$) with the real axis corresponds to the purely ohmic resistance R_0 of the cell, whereas the intercept at the lower frequency (for $\omega \to 0$) is identical to the differential resistance which can be obtained from the corresponding I-U characteristic at the given operating point. The difference between the low and high frequency intercept is the so-called polarisation resistance R_{pol} of the cell. R_{pol} is the sum of each single polarisation resistance caused by the loss mechanisms explained in chapter 2.2.
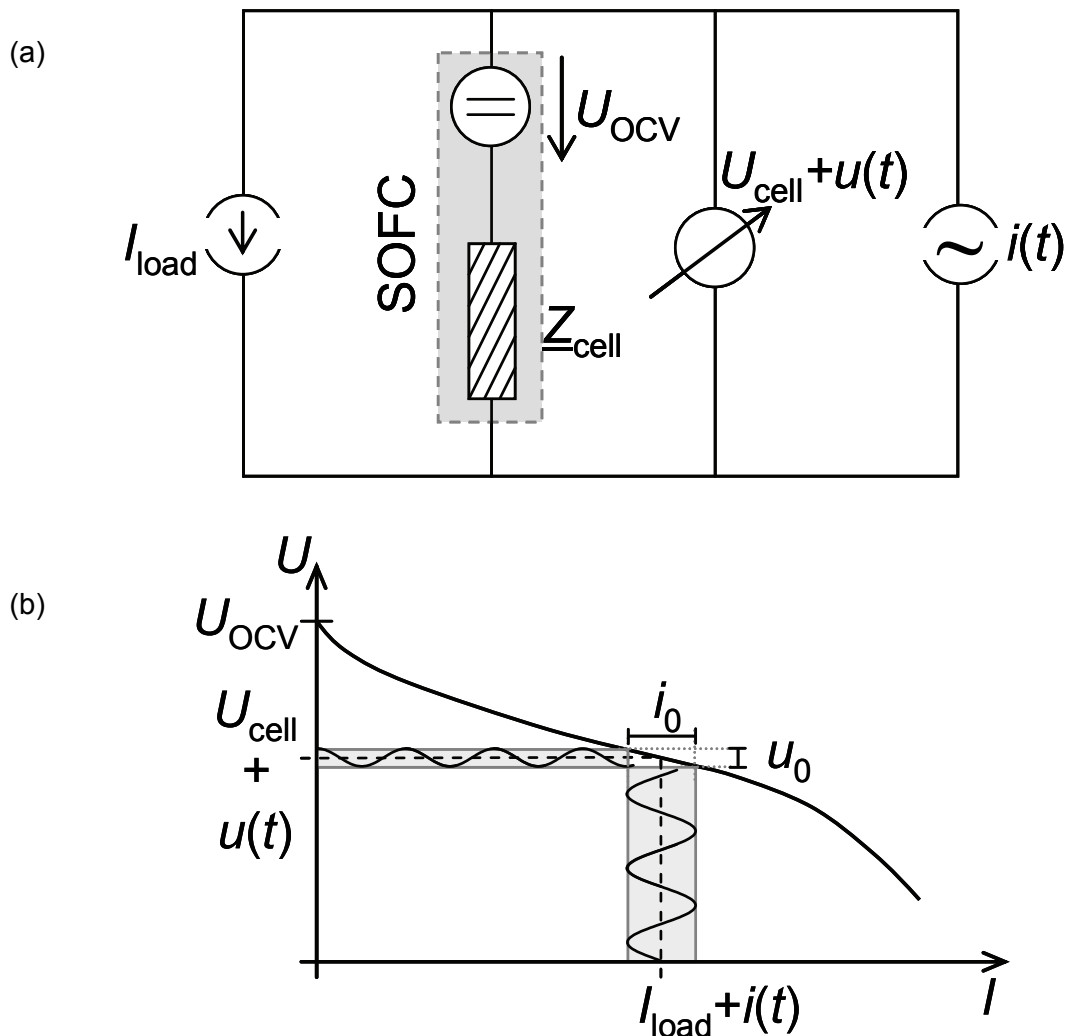
Fig. 3: (a) Basic experimental setup for the impedance measurement of a real SOFC with an internal impedance $\underline{Z}_{cell}$ and (b) corresponding I-U curve. A sinusoidal current of small amplitude $i(t)$ is superposed to a defined bias current I_{load} and the voltage response $u(t)$ is measured [19].
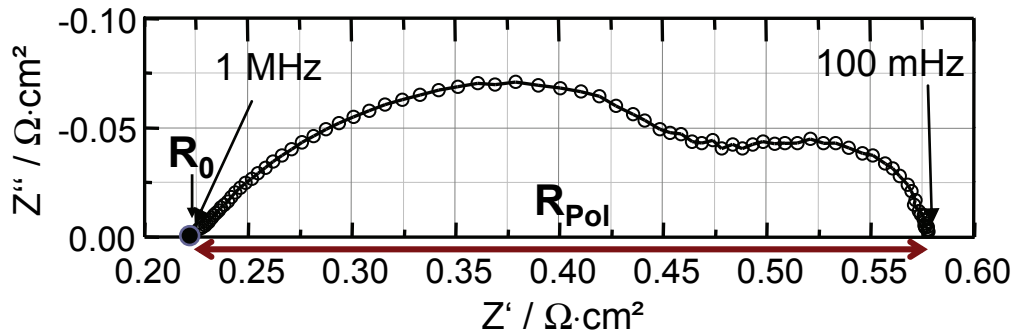
Fig. 4: Typical Nyquist-plot recorded on a real anode supported SOFC single cell. The high frequency intercept (for $\omega \rightarrow \infty$) with the real axis corresponds to the purely ohmic resistance R_0. The difference between the low and high frequency intercept is the so-called polarisation resistance R_{pol} of the cell [cell# Z1_153].

2.5 Equivalent Circuit Elements

A well established method for analysing impedance spectra is the use of impedance elements known from electrical engineering like resistors, capacitances or inductances as well as impedance functions developed specifically for describing processes tanking place in real complex electrochemical systems.

Generally, these impedance elements are connected together in an equivalent circuit describing the transfer function of the analysed system.

In the following special impedance elements, used to model the impedance response of the SOFC single cells analysed within this work, are presented.

2.5.1 RQ Element

Due to the required porosity and 3-dimensional extension of technical SOFC electrodes their complex microstructure differs from the 2-dimensional geometry of an ideal capacitor plate. As a consequence the resistance and capacitance contributions may differ with electrode position and vary over a certain range around a mean, but only their average (macroscopic) effects over the entire electrode surface is observed when measuring the impedance. Hence the electrochemical processes that occur at these electrodes show no perfect RC-behaviour, i.e. a single relaxation time, but are characterised by a distribution of relaxation times around a maximum [6, 19].

In order to describe this type of impedance behaviour the so-called Constant Phase Element (CPE), also known as Q-element, has been proposed [6].

The impedance of the Q-element is defined as follows:

13

$$\underline{Z}_Q(\omega) = \underline{Q}(\omega) = \frac{1}{(j\omega)^{n_Q} Y_Q} = \frac{1}{Y_Q}\omega^{-n_Q}e^{-j\frac{\pi}{2}n_Q} \text{ with } 0 \le n_Q \le 1 \text{ and } Y_Q = const. \qquad \text{Eq. 2.15}$$

with the modulus and the phase angle:

$$\left|\underline{Q}(\omega)\right| = \frac{1}{Y_Q}\omega^{-n_Q} \text{ and } \varphi(\omega) = -n_Q\frac{\pi}{2} \qquad \text{Eq. 2.16}$$

For $n_Q = 1$ the well known impedance expression of a capacitance with $Y_Q = C$ is obtained.

The parallel connection of a Q-element with a resistor R is called RQ-element. The complex impedance expression of an RQ-element is accordingly defined as:

$$\underline{Z}_{RQ}(\omega) = \frac{R}{1 + RQ^{-1}} \qquad \text{Eq. 2.17}$$

The characteristic time constant τ_{RQ} and frequency $f_{max,RQ}$ can be calculated by the following equations [6, 19]:

$$\tau_{RQ} = \sqrt[n_Q]{(RY_Q)} \qquad \text{Eq. 2.18}$$

and

$$f_{max,RQ} = \frac{1}{2\pi\tau_{RQ}} = \frac{1}{2\pi\sqrt[n_Q]{RY_Q}} \qquad \text{Eq. 2.19}$$

The complex plane plots (Nyquist plots) of an RQ-element for various n_Q values are given in Fig. 5. As discussed above, for $n_Q = 1$ the RQ-element is identical to an RC-element, thus the impedance follows a perfect semicircle. By decreasing the n_Q value a progressive broadening of the semicircle is observed, whereas for the special case $n_Q = 0$ the impedance reduces to a simple ohmic resistor R.
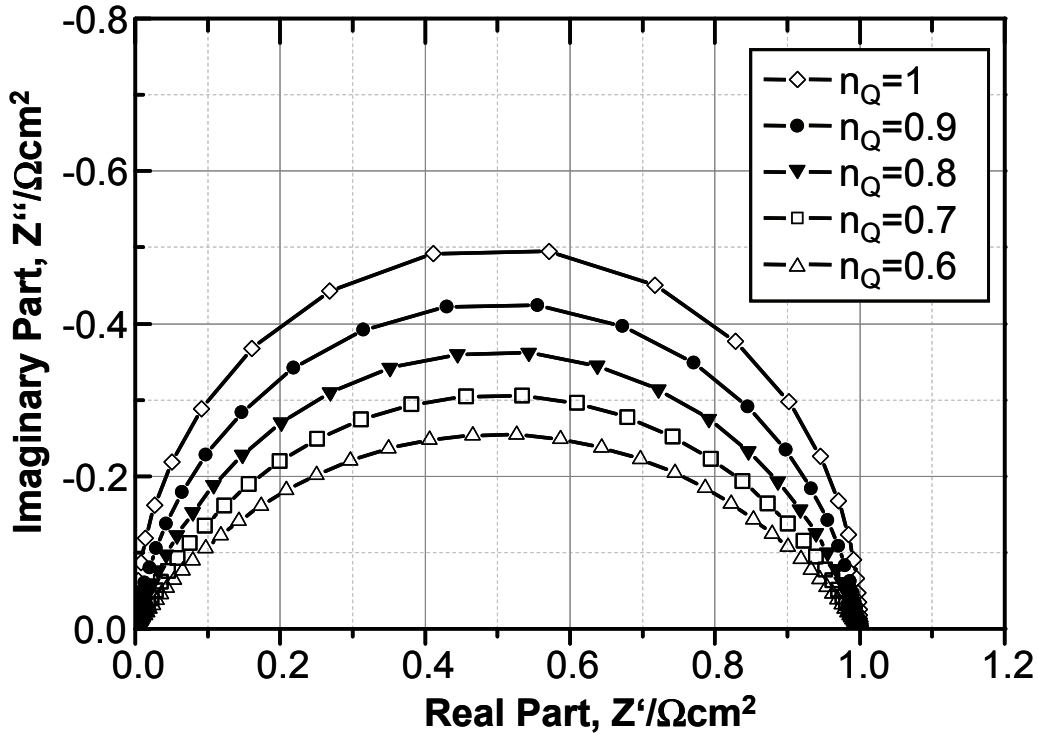
Fig. 5: Nyquist plot of an RQ-element for five different n_Q values (R = 1 $\Omega \cdot cm^2$) [19].

In this work two RQ-elements (RQ_{2A}, RQ_{3A}) connected in series have been identified to be appropriate for describing the impedance response of the activation polarisation process taking place in the anode of the SOFC single cell analysed within this study. A third RQ-element (RQ_{1C}) is used for modelling the impedance associated with the gas diffusion loss inside the cathode structure (cp. subchapter 4.1).

2.5.2 Generalised Finite Length Warburg Element

Another impedance element often encountered in impedance studies, describing diffusion-related processes, is the generalised finite length Warburg (G-FLW) element. The impedance expression for the G-FLW-element is given by [6, 20]:

$$\underline{Z}_{G-FLW}(\omega) = R_W \cdot \frac{\tanh\left[(j\omega T_W)^{n_W}\right]}{(j\omega T_W)^{n_W}}$$

Eq. 2.20

For a perfect one-dimensional diffusion limitation n_W is equal to 0.5 and T_W corresponds to l_d^2/D_i^{eff} with l_d the effective diffusion thickness and D_i^{eff} the effective diffusion coefficient of the diffusing species i. The diffusion resistance R_W is the $\omega \rightarrow 0$ limit of $\underline{Z}_{G-FLW}(\omega)$.

Fig. 6 shows the Nyquist plot of a simulated G-FLW-element with R_W = 21.8 m$\Omega \cdot cm^2$ and T_W = 0.0783 s and n_W = 0.465.

15
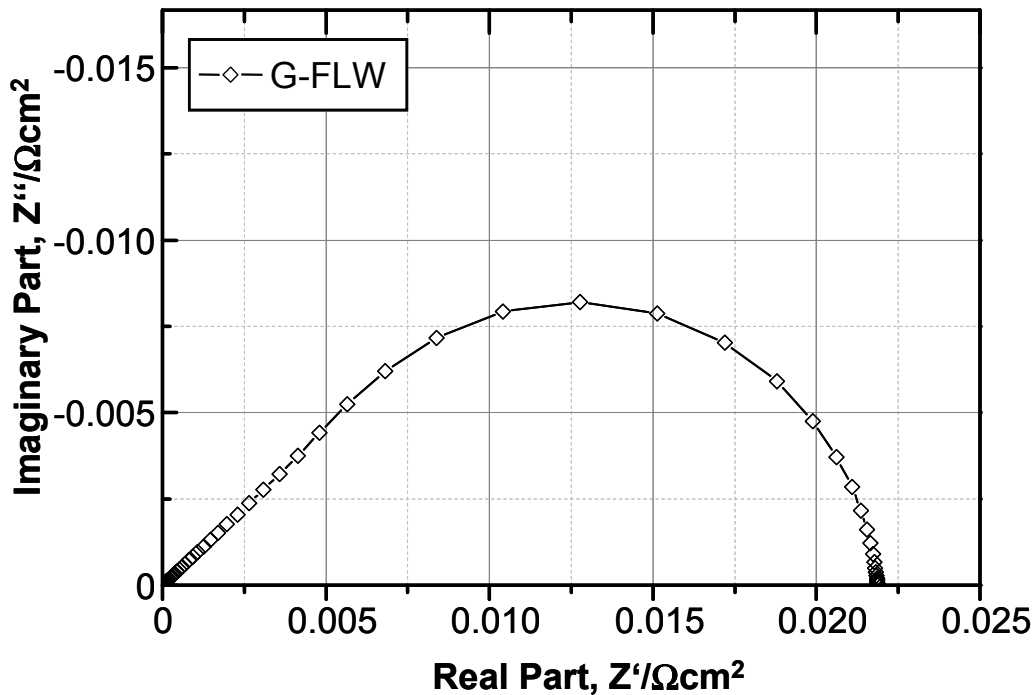
Fig. 6: Nyquist plot of an G-FLW-element with R_W = 21.8 mΩ·cm^2, T_W = 0.0783 s and n_W = 0.465.

In this work the G-FLW-element has been identified as the appropriate impedance element to describe the impedance response correlated with the gas diffusion loss inside the anode substrate of the analysed SOFC cell (cp. subchapter 4.1).

2.5.3 Impedance Model for Mixed-Conducting Cathodes (Gerischer Impedance)

To this day several studies in the literature have treated explicitly the impedance behaviour of mixed-conducting perovskite electrodes [21]. It is generally agreed that for porous mixed conducting (thick) cathodes with fast electronic transport (such as $La_{1-x}Sr_xCo_{1-y}Fe_yO_{3-\delta}$) the impedance is largely dominated by surface chemical exchange of O_2 and solid-state oxygen ion diffusion.

For the coupled processes of solid state diffusion and surface exchange the following impedance expression has been derived by Adler et al. [22]:

$$\underline{Z}_G(\omega) = \frac{R_{chem}}{\sqrt{1 + j\omega t_{chem}}}$$

Eq. 2.21

where R_{chem} and t_{chem} are a characteristic resistance and time constant, respectively, related to the thermodynamic, surface kinetic and transport properties of the mixed conductor [22, 23]:

$$R_{chem} = \left(\frac{RT}{2F^2}\right) \cdot \sqrt{\frac{\tau_s \cdot \gamma_{TD}^2}{(1-\varepsilon) \cdot a_S \cdot c_{mc}^2 \cdot k^\delta \cdot D^\delta}}$$

Eq. 2.22

16

$$t_{chem} = \frac{(1-\varepsilon)}{a_S} \cdot \frac{c_O}{c_{mc}} \cdot \frac{1}{k^\delta} \quad \text{with} \quad \frac{c_O}{c_{mc}} = \frac{3-\delta}{3} \qquad \text{Eq. 2.23}$$

where ε, a_S and τ_s are the porosity, electrochemical active surface area and solid-phase tortuosity, respectively, of the porous mixed conductor. c_O is the concentration of oxygen ions, c_{mc} the concentration of oxygen lattice sites, δ the fraction of oxygen vacancies and γ_{TD} is the so called thermodynamic enhancement factor defined as $1/2(\partial \ln pO_2)/(\partial \ln c_O)$ [24]. k^δ and D^δ are the chemical surface exchange coefficient and chemical diffusion coefficient, respectively. Fig. 7 shows the Nyquist plot of a simulated Gerischer-element with R_{chem} = 20 mΩcm^2 and t_{chem} = 0.004 s.

In this work the Gerischer-element has been identified as the appropriate impedance element to describe the impedance response resulting from oxygen incorporation and oxygen ion transport within the analysed ($La_{1-x}Sr_xCo_{1-y}Fe_yO_{3-\delta}$)-cathode structures (cp. subchapters 4.1 and 4.2).
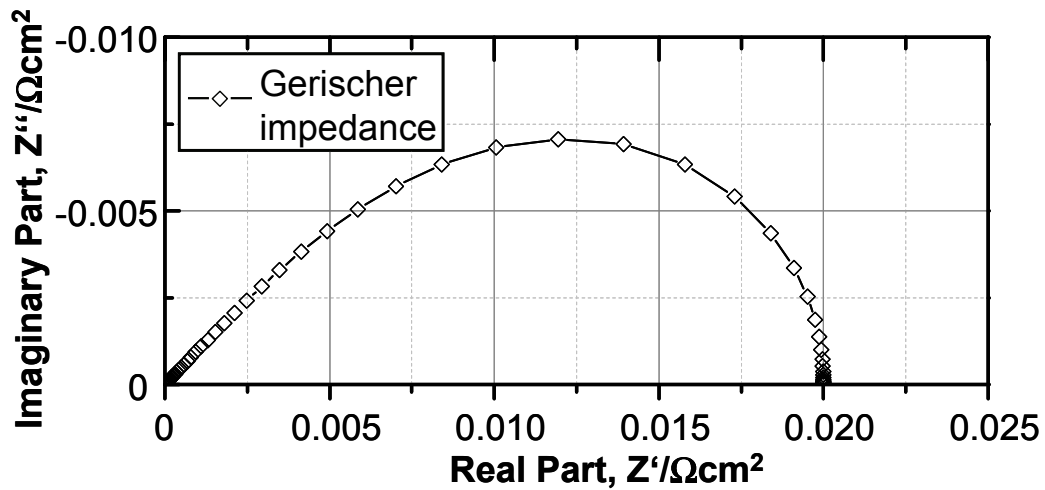
Fig. 7: Simulated Nyquist plot of a Gerischer-element with t_{chem} = 0.004 s and R_{chem} = 0.020 $\Omega \cdot$cm^2.

2.6 Impedance Analysis

2.6.1 Complex Nonlinear Least Squares (CNLS) Fit

From an analysis of the measured Nyquist plots and an appropriate combination of the impedance elements described above now an equivalent circuit model (ECM), which best describes the measured impedance response, may be proposed.

The unknown values of the equivalent circuit elements are generally evaluated by a Non-linear Least Squares (NLS) fitting algorithm. The aim of the least squares fitting procedure is to find a set of parameters which will minimize the sum [6]:

$$Q(\underline{p}) = \sum_{k=0}^{N-1} \left[w_{k,r}(\Phi'(\omega_k,\underline{p}) - Z'(\omega_k))^2 + w_{k,i}(\Phi''(\omega_k,\underline{p}) - Z''(\omega_k))^2 \right] \rightarrow Min \qquad \text{Eq. 2.24}$$

with

$$\underline{\Phi}(\omega_k,\underline{p}) = \Phi'(\omega_k,\underline{p}) + j\Phi''(\omega_k,\underline{p}) \text{ and } \underline{Z}(\omega_k) = Z'(\omega_k) + jZ''(\omega_k) \qquad \text{Eq. 2.25}$$

and

$$\underline{Z}(\omega_k) = Z'(\omega_k) + jZ''(\omega_k) \qquad \text{Eq. 2.26}$$

where $\underline{\Phi}(\omega_k,\underline{p})$ represents the model fit-function and $\underline{p} = (R_0, R_1, R_2, C_1, Q_2, ..., R_N, Q_N)$ the fit parameter-vector [6]. Here $Z'(\omega_k)$ and $Z''(\omega_k)$ are the real and imaginary part of the measured impedance curve $\underline{Z}(\omega_k)$, respectively. The factors $w_{k,r}$ and $w_{k,i}$ are the weighting factors associated with the kth data point.

In the present work the absolute measurement error of the recorded impedance spectra showed no mentionable change in magnitude over the entire frequency range (30 mHz-1 MHz). Therefore all weighting factors were set to unity.

The CNLS-fit of the impedance data was carried out with the commercially available CNLS-fit program ZView® [25].

Fig. 8 shows a typical CNLS-fit procedure that has been carried out on a measured impedance curve [26]. The applied equivalent circuit consists of an ohmic resistor R_0 and three RQ-elements connected in series (Fig. 8a). Before starting the actual fitting procedure, appropriate initial fit parameter values of the respective impedance elements need to be defined (i.e. estimated). Fig. 8b shows the measured impedance curve along with the simulated curve obtained from the equivalent circuit with the estimated initial parameters. Finally the ECM is fitted to the impedance spectra by the CNLS fitting algorithm (Fig. 8c).
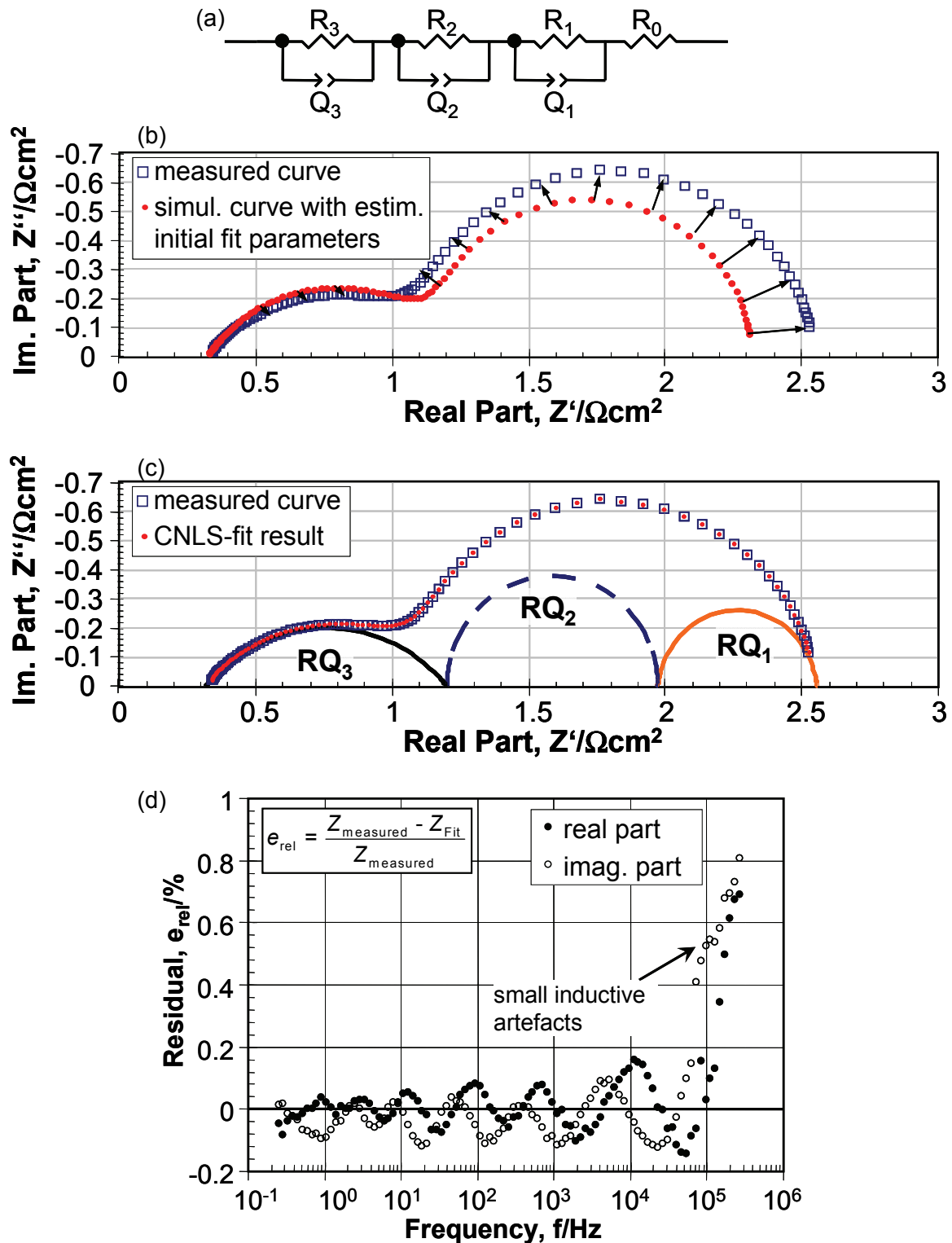
Fig. 8: (a) A priori defined equivalent circuit model consisting of a series connection of three RQ-elements (RQ_1, RQ_2, RQ_3) and an ohmic resistance (R_0). (b) Measured impedance curve along with the simulated curve obtained from the equivalent circuit with the estimated initial parameters. (c) CNLS-fit result. (d) Residual pattern of the CNLS fit [26].

The goodness of the fit is generally evaluated by analysing the relative errors (residuals) between the fit result and the measured curve at each single data point. Fig. 8d shows the

residuals of the CNLS-fit performed above. In this case the residuals are distributed uniformly around the frequency axis yielding errors less than 0.2 %. Only at higher frequencies (>200 kHz) inductive artefacts caused by the wiring becomes noticeable. Nevertheless, the error still lies below a very low value of 1 %. This indicates that the applied ECM is able to reproduce very well the measured impedance spectrum over the recorded frequency range. However, no conclusion about the physical correctness of an ECM can be drawn from the analysis of one single impedance spectrum. The residuals are "only" a mathematical quantity that describes the level of equivalency between the measured curve and the theoretical impedance spectrum of the proposed model. This discussion leads us directly to the weaknesses of the CNLS-fitting approach, which can be summarised as follows [19]:

-Poor resolution in the frequency domain.

-An *a priori* defined electrical equivalent circuit is needed

-Ambiguity of the equivalent circuit.

The poor resolution of Nyquist plots is problematic because the individual impedance-related processes of complex electrochemical systems, like SOFC single cells, are numerous and their contributions to the impedance curve overlap. This problematic is aggravated by the fact that not every process contributes in the same way to the total polarisation loss. Therefore it is very difficult to discover processes with a small contribution, because they are almost totally covered by the processes that show a large polarisation loss. One can only hope that the dispersion maxima of the processes are so far away, that the processes can be identified by optical inspection of the underlying Nyquist plot.

Another important weakness of the CNLS analysis method is the ambiguity of the equivalent circuits, i.e. one and the same impedance spectrum may be obtained from different circuits [6, 19]. Therefore it is hazardous to propose an a priori model without any knowledge about the real number and physical origin of the polarisation processes contributing to the impedance response of the cell

To overcome these disadvantages an alternative approach for analysing impedance spectra will be used in this work. The equivalent circuit model and the optimal starting parameters for the CNLS algorithm will be obtained by a pre-identification of the impedance response by calculating and analysing the corresponding distribution function of relaxation times (DRT) (cf. chapters 2.6.2 and 4.1). The DRT approach is particularly advantageous for the analysis of (anode supported) SOFC single cells coupled to thin electrolytes (thickness less than 20 μm), where reference electrodes are not applicable for the separation of anode and cathode losses [27].

However, in all cases the ultimate evaluation about the physical correctness of a proposed equivalent circuit should be performed by analysing the quantitative dependency of the model-parameters for a wide range of operating conditions.
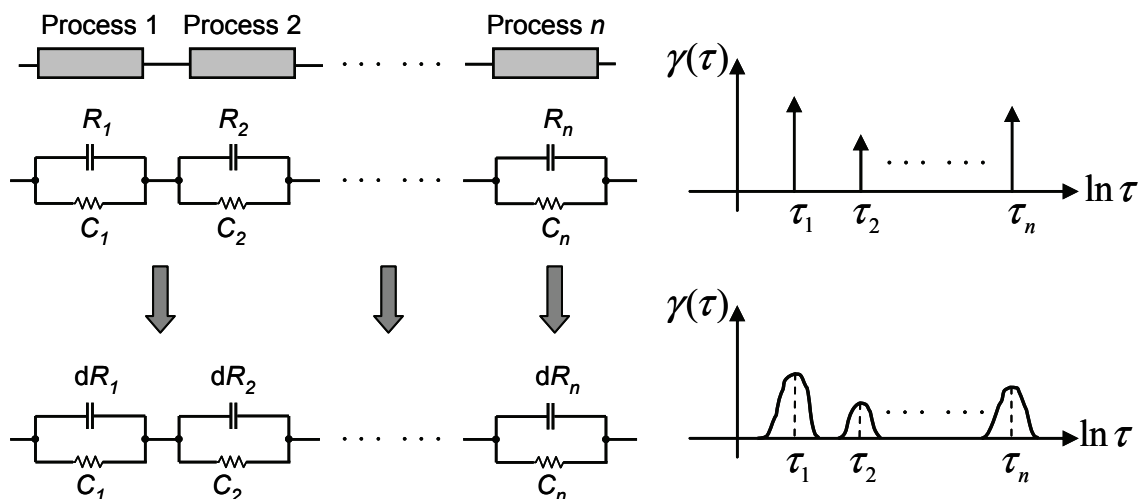
2.6.2 Distribution of Relaxation Times

As will be shown later (in chapter 4), the calculation of the distribution of relaxation times (DRT) represents a valuable approach to the challenge of finding an adequate equivalent circuit model able to describe the physical behaviour of the SOFC single cells analysed within this work.

In the following the concept of the distribution of relaxation times will be introduced and an overview of the analytical and numerical calculated DRTs of selected impedance elements will be given.

Theoretical Background

The DRT-method uses the fact, that every impedance function that obeys the Kramers-Kronig relations can be represented as a differential sum of infinitesimal small RC-elements (Fig. 9). This sum goes from 0 to infinity (∞). [28]

Fig. 9: Interpretation of EIS data in terms of equivalent circuit models and distribution of relaxation times. Dynamic processes are represented in the distribution by peaks: in the case of ideal RC processes by Dirac impulse functions at the corresponding relaxation time [$\delta(\tau\text{-}\tau_n)$], whereas real processes exhibit peaks distributed around a main relaxation time τ_n [28].

Let us consider a serial connection of RC-elements (Fig. 9). Let $R_{pol,n} = \gamma_n \cdot R_{pol}$ be the real part resistance and τ_n the relaxation time of the nth RC-element. R_{pol} represents the total polarisation resistance of the circuit. Hence, for the total impedance the following equation holds [28]:

$$\underline{Z}_{pol}(\omega) = \sum_{n=1}^{N} \frac{R_{pol,n}}{1+j\omega\tau_n} = R_{pol} \sum_{n=1}^{N} \frac{\gamma_n}{1+j\omega\tau_n}$$

Eq. 2.27

with

$$\sum_{n=1}^{N} \gamma_n = 1$$

Eq. 2.28

Where $\omega = 2\pi f$ is the angular frequency, N is the number of RC-elements and j is the imaginary unit. Here γ_n weights the contribution of the nth polarisation process to the total polarisation loss.

Instead of a finite number of RC-elements one can assume now an infinite number with relaxation times ranging continuously from 0 to ∞ and obtain the following integral equation [28]:

$$\underline{Z}_{pol}(\omega) = R_{pol} \int_{0}^{\infty} \frac{\gamma(\tau)}{1+j\omega\tau} d\tau$$

Eq. 2.29

with,

$$\int_{0}^{\infty} \gamma(\tau) d\tau = 1$$

Eq. 2.30

The integral equation 2.29 links the distribution function $\gamma(\tau)$ with the frequency dependent part of the measured impedance $\underline{Z}_{pol}(\omega)$. In Eq. 2.29 $\frac{\gamma(\tau)}{1+j\omega\tau} d\tau$ represents the fraction of the overall polarisation resistance with relaxation times between τ and $\tau+d\tau$. This implies that the area comprised by a peak equals the total polarisation resistance of the respective dynamic process.

The problem now is to obtain $\chi(\tau)$ from $\underline{Z}_{pol}(\omega)$. The real and imaginary parts of the impedance data of a linear, time invariant system are connected by the Kramers-Kronig transformations. Therefore, it is sufficient to consider the imaginary part of the impedance only [28]:

$$\text{Im}\{\underline{Z}_{pol}(\omega)\} = Z''(\omega) = R_{pol} \int_0^\infty \frac{\omega\tau}{1+(\omega\tau)^2} \chi(\tau) d\tau \qquad \text{Eq. 2.31}$$

After the substitution of the frequency variables with the following expressions,

$$x = \ln\frac{\omega}{\omega_0}; \ y = \ln(\omega\tau); \ dy = \frac{1}{\tau}d\tau \qquad \text{Eq. 2.32 -2.34}$$

Eq. 2.31 adopts the following form:

$$Z''(\omega) = -R_{pol} \int_0^\infty \frac{e^y}{1+e^{2y}} \chi(\tau) d\tau \qquad \text{Eq. 2.35}$$

with

$$sech(x) = \frac{2}{e^y + e^{-y}} \ \text{ and } \ \hat{g}(y-x) = \chi(\tau)\tau \qquad \text{Eqs. 2.36.-2.37}$$

Eq. 2.35 is recognizable as the following convolution product:

$$Z''(x) = -\frac{R_{pol}}{2} \int_{-\infty}^\infty sech(y)\hat{g}(y-x)dy = -\frac{R_{pol}}{2}sech(x) * \hat{g}(x) = -\frac{1}{2}sech(x) * g(x) \qquad \text{Eq. 2.38}$$

$$\text{with } g(x) = R_{pol} \cdot \hat{g}(x)$$

Eq. 2.38 can be converted in an algebraic product by Fourier-transformation and, finally, the distribution function $g(x)$ is obtained by back transformation. This inversion problem is controlled by application of digital filters in the Fourier space and an extrapolation technique to enlarge the frequency range of the data. The detailed procedure is described in [19].

However, in the present work the inversion problem shown in Eq. 2.38 was not solved by the above-mentioned Fourier space transformation and subsequent digital filtering. Alternatively, the convolution product (Eq. 2.38) can be regarded as a Fredholm integral equation of the first kind which can be described by the following equation [19, 29]:

$$\int_a^b K(x,y)g(y)dy = z(x)$$

<div align="right">Eq. 2.39</div>

with K representing the Kernel of a given function $z(x)$ and $g(y)$ representing the unknown solution. For the solution of this inverse problem (also called "ill-posed problem"), in this work the Tikhonov regularisation [30-32] method is applied within the program "FTIKREG" [33]. This algorithm has been implemented into a user-friendly Microsoft Excel sheet by Dipl.-Ing. Volker Sonn (IWE). The Tikhonov regularisation method leads, principally, to the same result as the Fourier transformation method.

It is worth to mention that in this study the distributions of relaxation times were calculated from the real part of the spectra, since these were less affected by noise as compared to the imaginary part.

Analytical and Numerical Distribution Functions

In the following an overview of the analytical and numerically calculated DRTs of the impedance elements (cf. chapter 2.5) used within this work to model the impedance response of the ASC single cells are presented.

<u>RQ-element</u>

As derived elsewhere [19, 34], the analytical DRT of an impedance can be calculated by the following formula:

$$g(x) = -\frac{1}{\pi}\left[z\left(x+j\frac{\pi}{2}\right) + z\left(x-j\frac{\pi}{2}\right)\right] \text{ with } x = \ln(\omega), \text{ i.e. } (\omega_0 = 1)$$

<div align="right">Eq. 2.40</div>

Here $z(x)$ represents the analytical expression of the imaginary part of the corresponding impedance element.

By applying Eq. 2.40 the following analytical expression for the DRT of an RQ-element has been derived [19]:

$$g_{RQ}(x) = \frac{R_{pol}}{2\pi} \frac{\sin\left[(1-n_Q)\pi\right]}{\cosh(n_Q x) - \cos\left[(1-n_Q)\pi\right]}$$

<div align="right">Eq. 2.41</div>

In Fig. 10 the analytical DRTs of an RQ-element for five different n_Q-values are shown (the corresponding Nyquist plots were depicted in Fig. 5 before). As can be seen, the theoretical

DRT $g(f)$ of an RC-element (RQ-element with n_Q=1) is represented by a Dirac peak $\delta(f\text{-}f_{max})$ at the respective angular summit frequency ω_{max}. For an RQ-element (n_Q<1) the peak broadens out with decreasing exponent n_Q.
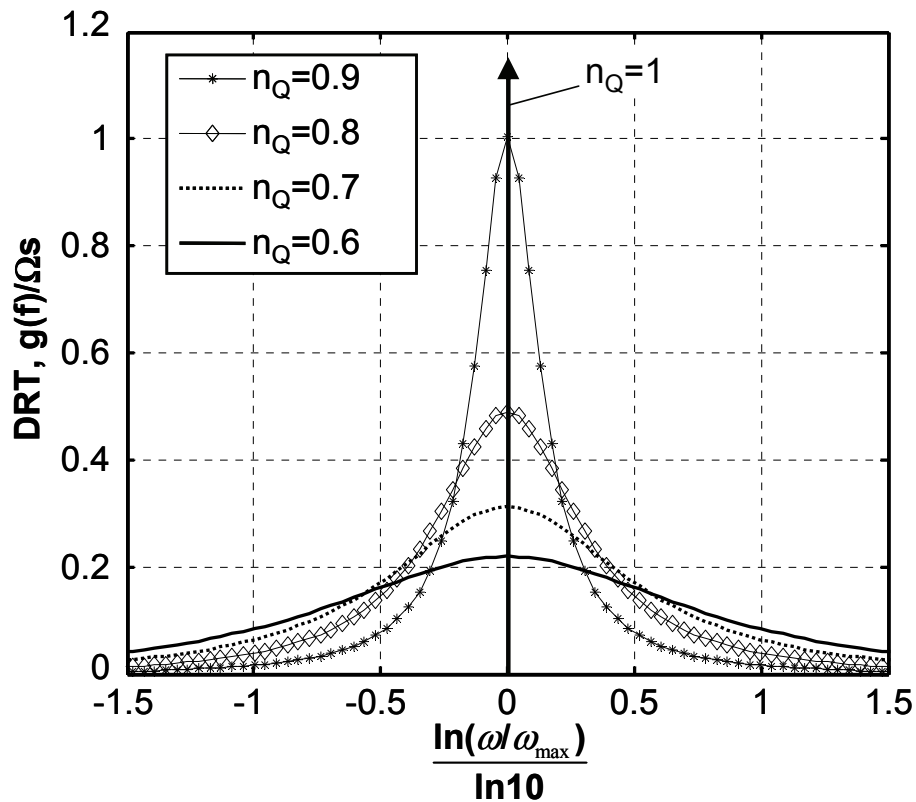
Fig. 10: Theoretical DRTs of an RQ-element for five different n_Q-values. The corresponding Nyquist curves were shown in Fig. 5 before. (The distributions were calculated from the imaginary part of the impedance using Eq. 2.40) [19].

The corresponding numerical DRTs of the RQ-elements calculated from synthetic data by the program "FTIKREG" are shown in Fig. 11. In the case of n_Q=1 the numerical DRT shows no ideal Dirac peak, and even for n_Q<1 the DRTs show generally a broader course compared to the analytical one. This broadening has to be attributed to, both, the finite frequency range and the discrete nature of the underlying synthetic data and can, therefore, not be avoided (the same holds for measured data) [19].
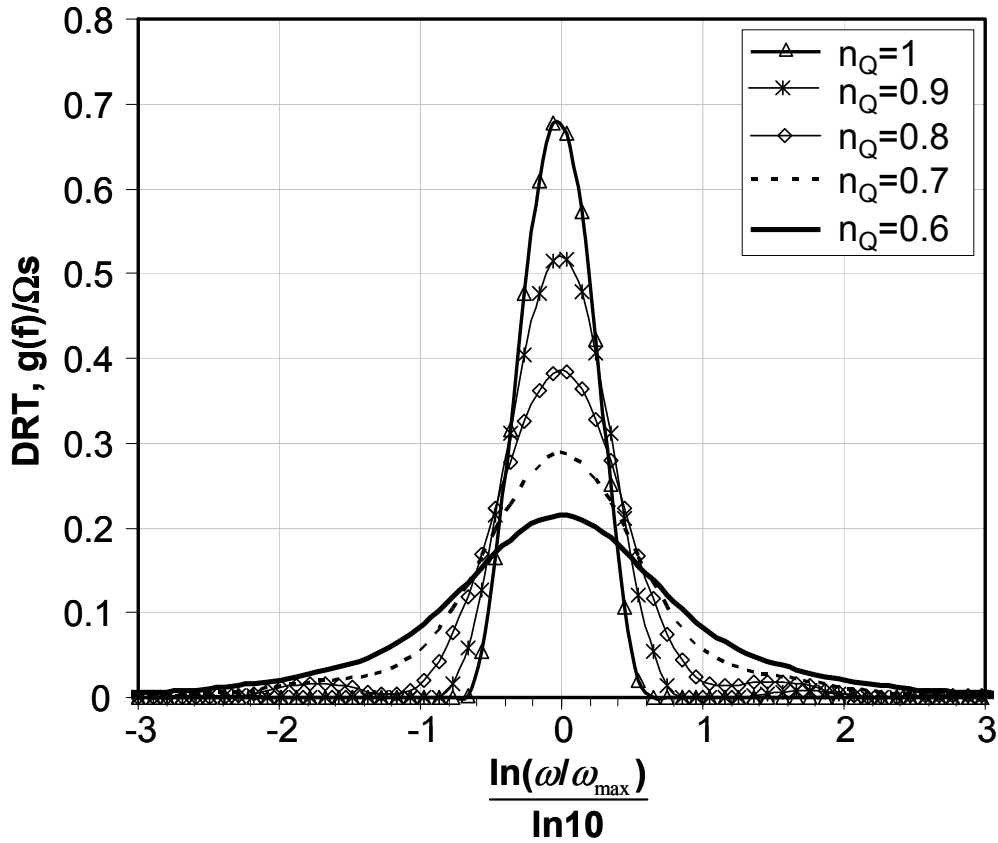
Fig. 11: Numerically calculated DRTs of an RQ-element for five different n_Q-values. The numerical calculation procedure causes a broadening of the distribution (cp. corresponding theoretical DRTs in Fig. 10).

G-FLW-element

From Eq. 2.20 the following analytical expression for the imaginary part of a G-FLW-element can be derived:

$$z_{G-FLW}(x) = \frac{R_W\left[\cos\left(\dfrac{\pi}{2n_W}\right)\sin\left(2\sqrt[n_W]{e^x T_W}\sin\left(\dfrac{\pi}{2n_W}\right)\right) - \sin\left(\dfrac{\pi}{2n_W}\right)\sinh\left(2\sqrt[n_W]{e^x T_W}\cos\left(\dfrac{\pi}{2n_W}\right)\right)\right]}{\sqrt[n_W]{e^x T_W}\left[\cos\left(2\sqrt[n_W]{e^x T_W}\sin\left(\dfrac{\pi}{2n_W}\right)\right) + \cosh\left(2\sqrt[n_W]{e^x T_W}\cos\left(\dfrac{\pi}{2n_W}\right)\right)\right]}$$

Eq. 2.42

By insertion of Eq. 2.42 in Eq. 2.40 and performing the appropriate simplifications, the closed form expression (Eq. 2.43) for the DRT of a G-FLW-element (for $n_W < 2$) is obtained.

$$g_{G-FLW}(x) = -\frac{R_W}{\pi}\left[\begin{array}{l}\dfrac{1}{2}e^{-\frac{j\pi+2x}{2n_W}}\dfrac{1}{\sqrt[n_W]{T_W}}\operatorname{sech}\left(\sqrt[n_W]{e^x T_W}\right)\operatorname{sech}\left(\sqrt[n_W]{e^{j\pi+x}T_W}\right)\\[2mm] \left[\cos\left(\dfrac{\pi}{2n_W}\right)\sin\left(2\sqrt[n_W]{je^x T_W}\sin\left(\dfrac{\pi}{2n_W}\right)\right)-\sin\left(\dfrac{\pi}{2n_W}\right)\sinh\left(2\sqrt[n_W]{je^x T_W}\cos\left(\dfrac{\pi}{2n_W}\right)\right)\right]\\[2mm] -\dfrac{1}{2}j\dfrac{1}{\sqrt[n_W]{e^x T_W}}\left(\tanh\left(\sqrt[n_W]{e^x T_W}\right)-e^{\frac{j\pi}{n_W}}\tanh\left(\sqrt[n_W]{e^{-j\pi+x}T_W}\right)\right)\end{array}\right]$$

with $x = \ln(\omega)$ and for $n_W < 2$

<div align="right">Eq. 2.43</div>

The analytical DRTs of a G-FLW-element with R_W = 21.8 mΩ and T_W = 0.0783 s and for four different n_W-values are shown in Fig. 12 (the corresponding Nyquist plot for the case n_W = 0.465 is depicted in Fig. 6 before). As can be seen, the DRT of a G-FLW-element is highly asymmetric and characterised by a large peak located at the characteristic frequency followed by smaller peaks at higher frequencies. In the same way as for the RQ-element a progressive broadening of all peak is observed by decreasing exponent n_W. Additionally a slight shift of the peaks towards higher frequencies is observable when lowering the n_W-value.
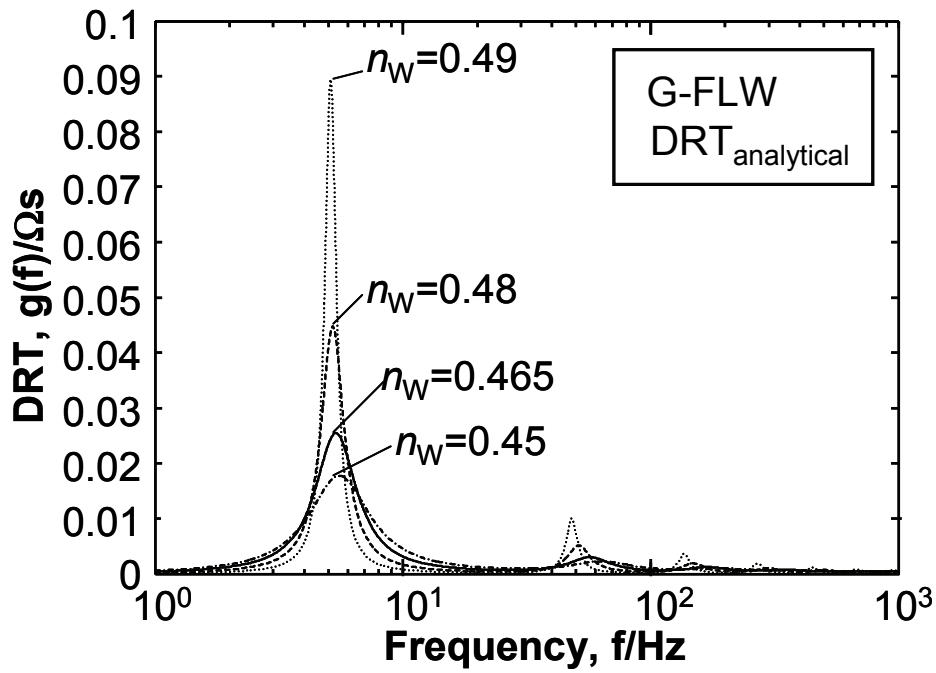
Fig. 12: Theoretical DRTs of an G-FLW-element for four different n_W-values (R_W = 21.8 mΩ, T_W = 0.0783 s). The corresponding Nyquist curve for the case n_W = 0.465 was shown in Fig. 6 before. (The distributions were calculated from the imaginary part of the impedance using Eq. 2.40).

In Fig. 13 the analytical and the numerically calculated DRT for the case n_W = 0.465 are compared. As already discussed above, the numerical calculation procedure causes a broadening of the DRT. Therefore only the first two major peaks are resolvable in the numerically calculated DRT of a G-FLW-element.
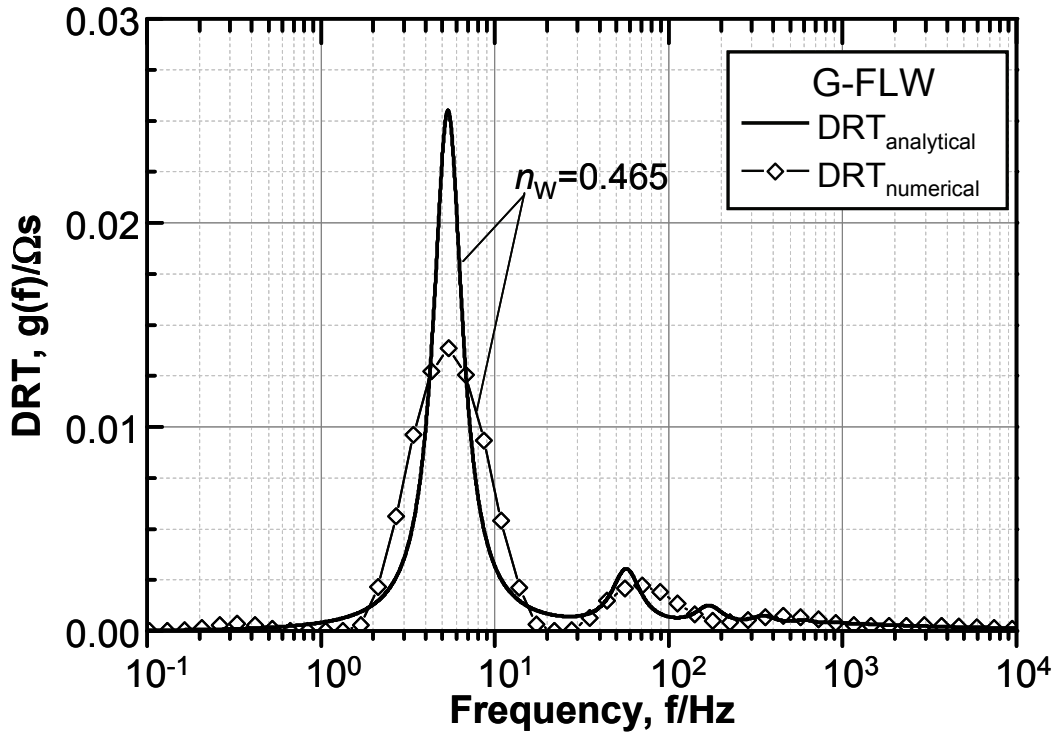
Fig. 13: Theoretical DRT compared with numerically calculated DRT (R_W = 21.8 mΩ, T_W = 0.0783 s n_W = 0.465). The numerical calculation procedure causes a broadening of the distribution.

Gerischer-Impedance

From Eq. 2.21 the following analytical expression for the imaginary part of the Gerischer-element can be derived:

$$\text{Im}\{\underline{Z}_G(\omega)\} = Z_G'' = -\frac{R_{chem}}{\sqrt{2}}\sqrt{\frac{\left(\sqrt{(\omega t_{chem})^2 + 1} - 1\right)}{(\omega t_{chem})^2 + 1}} \qquad \text{Eq. 2.44}$$

By insertion of Eq. 2.44 in Eq. 2.40 and performing the appropriate simplifications, the following closed form expression for the DRT is obtained.

$$\tilde{g}_G(x) = \frac{\sqrt{2}R_{chem}}{\pi}\sqrt{\frac{\left(\sqrt{1 - (e^x t_{chem})^2} - 1\right)}{1 - (e^x t_{chem})^2}} \qquad \text{Eq. 2.45}$$

However, Eq. 2.45 represents a (non-trivial) complex valued function with a singularity at $x = \ln(1/t_{chem})$ (where the denominator of Eq. 2.45 is zero). For R_{chem} = 0.020 Ω and t_{chem} = 0.004 s Eq. 2.45 gives the imaginary and real part curves depicted in Fig. 14 (the

corresponding Nyquist plot was shown in Fig. 7 before). By numerical integration of both components one obtains:

$$\int_{-10}^{10} \text{Re}\{\tilde{g}_G(x)\}dx = 0.020 \ \Omega$$

Eq. 2.46

and

$$\int_{-10}^{10} \text{Im}\{\tilde{g}_G(x)\}dx = 0.0001 \Omega$$

Eq. 2.47

As stated earlier, the area comprised by the DRT of a polarisation process equals the total polarisation resistance of the respective dynamic process. By comparing the integration results shown above (Eq. 2.46 and Eq. 2.47) one can notice that the integral of the real part of $\tilde{g}_G(x)$ (i.e. Eq. 2.46) delivers the total polarisation resistance $R_{chem} = 0.020 \ \Omega$ of the underlying Gerischer-impedance. Therefore, it can be supposed that the analytical DRT $g_G(x)$ of a Gerischer-element is described by only the real component of Eq. 2.45, as follows:

$$g_G(x) \approx \begin{cases} \text{Re}\left\{ \dfrac{\sqrt{2}R_{chem}}{\pi} \sqrt{\dfrac{\left(\sqrt{1-\left(e^x t_{chem}\right)^2} - 1\right)}{1-\left(e^x t_{chem}\right)^2}} \right\} & x \geq \ln\left(\dfrac{1}{t_{chem}}\right) \\ \\ 0 & x < \ln\left(\dfrac{1}{t_{chem}}\right) \end{cases}$$

Eq. 2.48

The approximate equality sign appears in Eq. 2.48 to indicate that the discussion made above should not be seen as a final proof that $g_G(x)$ represents (mathematically) correctly the analytical expression for the DRT of a Gerischer-element. However it is believed that $g_G(x)$ represents, at least, a very good approximation of the analytical DRT of a Gerischer-impedance.
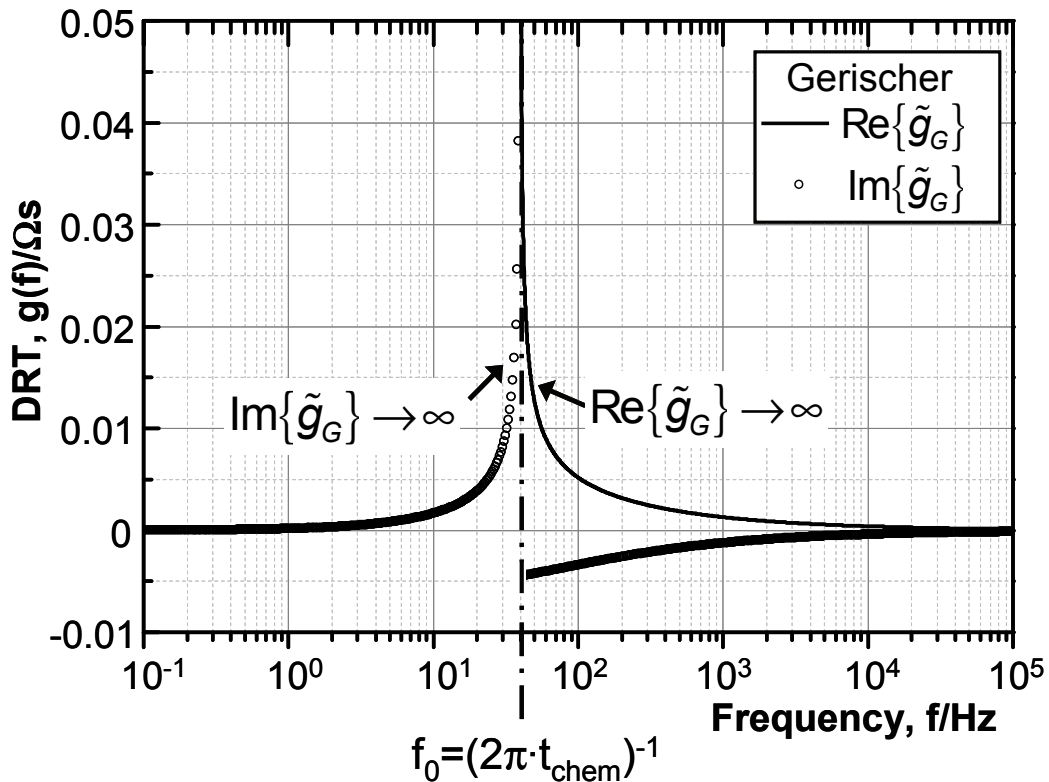
Fig. 14: When calculating the theoretical DRT of a Gerischer-element with Eq. 2.40 a complex valued function ($\tilde{g}_G(x)$) is obtained. The real and imaginary part of $\tilde{g}_G(x)$ show a singularity at $f_0=1/(2\pi t_{chem})$ (R_{chem} = 20 mΩ, t_{chem} = 0.004 s, $f_0 \approx$ 40 Hz) (cf. Eq. 2.45). The corresponding Nyquist curve was shown in Fig. 7 before.

At this point it is worth mentioning, that a more detailed mathematical treatment of Eq. 2.45 would probably deliver a more definitive conclusion about the correct analytical DRT-expression of a Gerischer-impedance. However, this is beyond the scope of this thesis and should be addressed in a future, separate work.

By examining Eq. 2.48 and reminding that $x=\ln(\omega)$ (with $\omega = 2\pi f$) one can recognize that $g_G(x)$ increases exponentially approaching an asymptote going to infinity located at the characteristic frequency $f_0 = 1/(2\pi t_{chem}) \approx 40$ Hz. For frequency values $f<f_0$ the distribution function is zero. In Fig. 15 $g_G(x)$ and the numerical DRT of a Gerischer impedance (with R_{chem} = 20 mΩ and t_{chem}= 0.004 s) are compared. The numerical DRT is characterised by two distinctive peaks (1. maximum at ca. 60 Hz; 2. maximum at about 450 Hz). For higher frequencies the numerical distribution seems to follow the exponential decay of the analytical function towards zero.
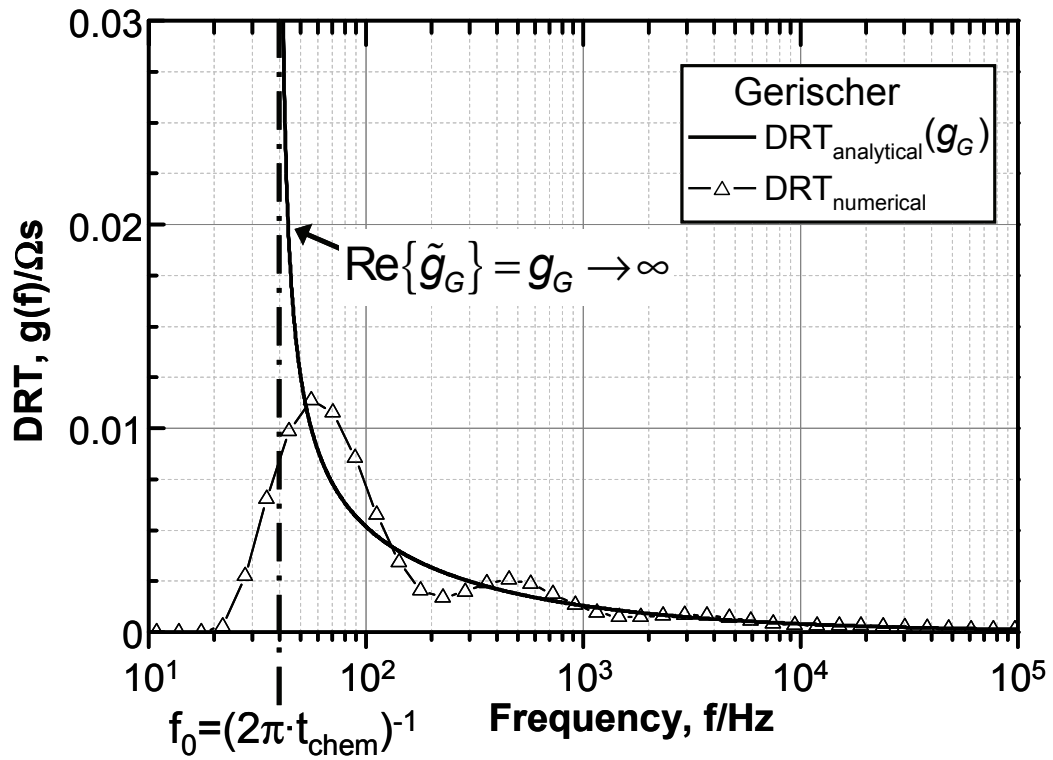
Fig. 15: Numerically calculated DRT of a Gerischer-element compared with the real part of Eq. 2.45 (i.e. $g_G(x)$). The corresponding Nyquist curve was shown in Fig. 7 before. (R_{chem} = 20 mΩ, t_{chem} = 0.004 s).

3 Experimental

This chapter describes: (i) the cell-design and material composition of the analysed ASC single cells, (ii) the measurement setup used for the electrochemical characterization, (iii) the operating parameter range over which the measurements were carried out, and (iv) the assessment of impedance measurement data by means of Kramers-Kronig analysis.

3.1 Single Cell Geometry

For the anode-supported SOFC single cells (Fig. 16) analysed in this work, an anode functional layer (Ni/8YSZ, thickness approximately 7 µm) and the electrolyte (8YSZ, thickness approximately 10 µm) were applied onto an anode substrate (Ni/8YSZ, thickness 1.0 and 1.5 mm). Onto the electrolyte, a $Ce_{0.8}Gd_{0.2}O_{2-\delta}$ (GDC) interlayer with a thickness of approximately 7 µm was screen-printed and fired. This GDC interlayer serves as a buffer layer to prevent chemical reaction between the electrolyte material 8YSZ and the cathode material L58SCF ($La_{0.58}Sr_{0.4}Co_{0.2}Fe_{0.8}O_{3-\delta}$, thickness approximately 45 µm), which is subsequently screen-printed on top of the fired buffer layer. Please note that, additionally, in chapter 4.2.2 the performance of two alternative cathode compositions ($La_{0.68}Sr_{0.3}Co_{0.2}Fe_{0.8}O_{3-\delta}$ and $La_{0.68}Sr_{0.3}FeO_{3-\delta}$) will be evaluated and compared to the state-of-the-art L58SCF cathode.

The active surface area of the cathodes (working cathode), and therefore the active cross-sectional area of the cells, is $1\ cm^2$ (10 mm x 10 mm). In addition, a reference cathode (reference electrode) is screen-printed both before the working cathode and behind it (in direction of the gas flow), in order to monitor the open-circuit voltage U_{OCV} The anode substrate has a cross-sectional area of 50 mm x 50 mm and is entirely covered by the thin-film electrolyte. A scanning electron micrograph of the polished cross section of a fractured cell showing part of the porous anode, the dense electrolyte, the GDC buffer layer, and the porous cathode, is depicted in Fig. 17. Preparation and performance of this cell type that has been developed at Forschungszentrum Jülich (FZJ) are described in detail in [35] and [36].

(a)

8YSZ-electrolyte
(transparent)

1cm

GDC interlayer

gas flow direction

reference electrode

working cathode
(1x1cm²)

(b)

LSCF or LSF cathode (~ 45µm)

Ni/8YSZ anode
functional layer (~7µm)

GDC interlayer(~ 7µm)
electrolyte (~ 10µm)

Ni/8YSZ anode substrate
(1.0 or 1.5 mm)
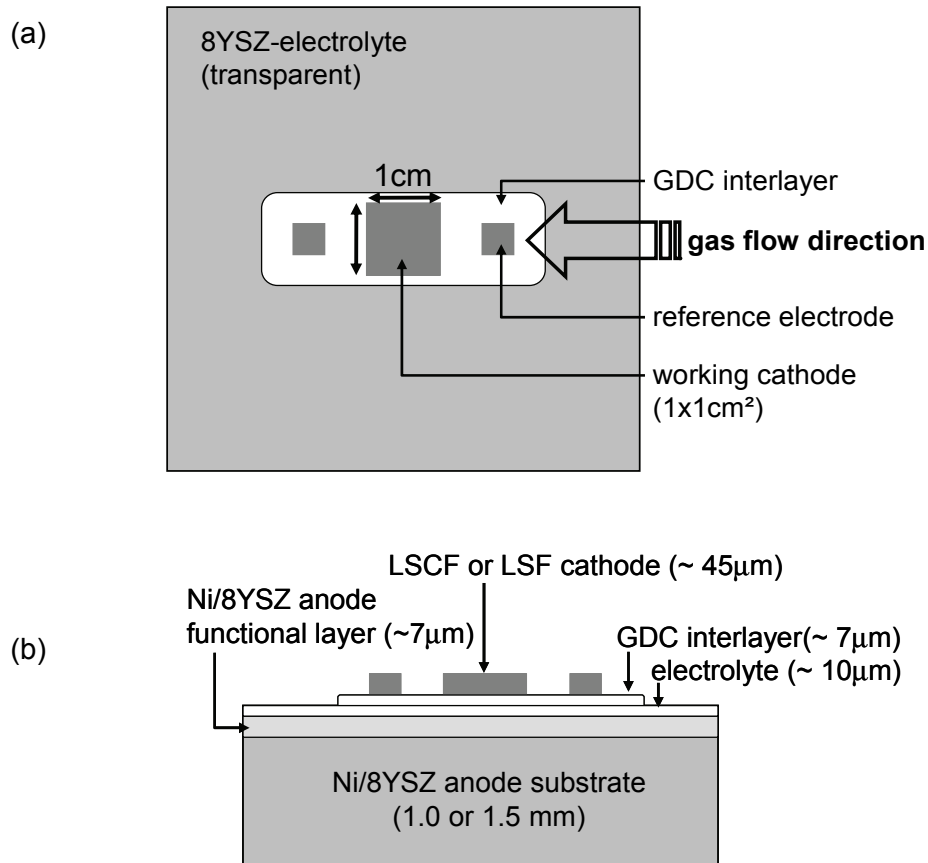
Fig. 16: (a) Design of the working and auxiliary (reference probe) electrodes at the cathode side of an anode supported SOFC single cell (top view). (b) Side view of the cell with the porous anode, the anode functional layer, the dense electrolyte, the GDC interlayer and the porous cathode.

LSCF-cathode

GDC-interlayer
8YSZ-electrolyte
Ni/8YSZ functional layer

Ni/8YSZ-substrate

10µm
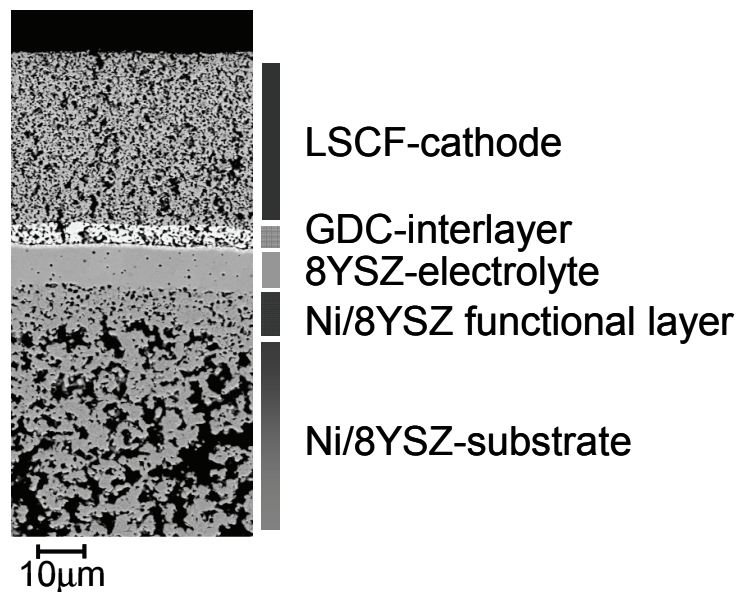
Fig. 17: Scanning electron micrograph of the polished cross section of a FZJ ASC cell showing part of the porous anode, the dense electrolyte, the GDC buffer layer, and the porous cathode.

3.2 Measurement Setup

The single cell shown in Fig. 16 is mounted in a ceramic Al_2O_3 housing (Fig. 18). Anode and cathode are contacted with Ni (1 cm^2, 3487 meshes/cm², 0.065 mm wire thickness) and Au (1 cm^2, 1024 meshes/cm²) meshes, respectively. Both gas chambers are separated by a gold seal.

The single cells were investigated under ambient air pressure at various gas compositions of H_2, H_2O and N_2 at the anode side and of O_2 and N_2 (more precisely: a mixture of Air and N_2) at the cathode side. The overall gas flow rate was constantly kept at 250 ml/min for the anode as well as the cathode. Gas compositions and gas flow were controlled by a mass flow (MFC) controller battery. High contents of water vapour could be realised by feeding oxygen into an upstream combustion chamber. The resulting gas mixture is then transported across the anode. The employed measurement setup was developed at the Institute of Materials for Electrical and Electronic Engineering (IWE) (Fig. 19) [37].
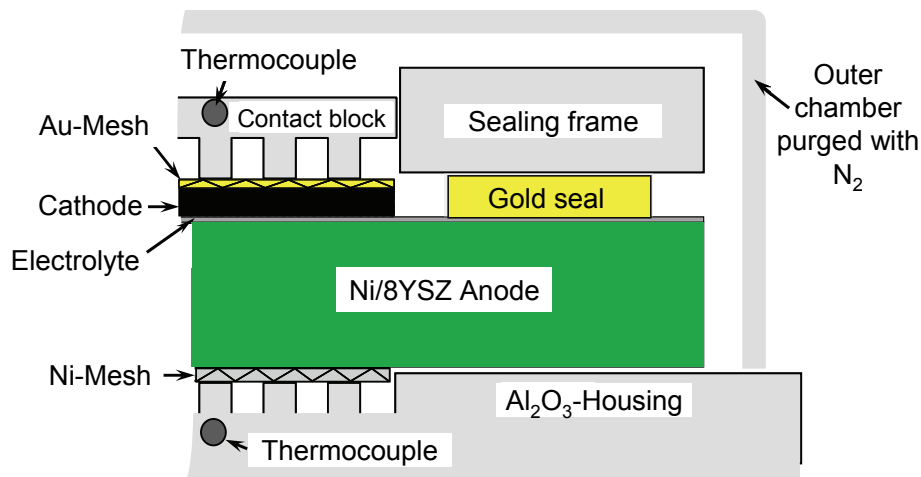
Fig. 18: The anode-supported SOFC single cell is mounted in a ceramic Al_2O_3 housing. Cathode and anode are contacted with an Au-Mesh and Ni-Mesh, respectively. Both gas chambers are separated by a gold seal. The housing is covered by an Al_2O_3 hood which is purged with nitrogen (N_2).

$$2H_2 + O_2 \rightarrow 2H_2O$$
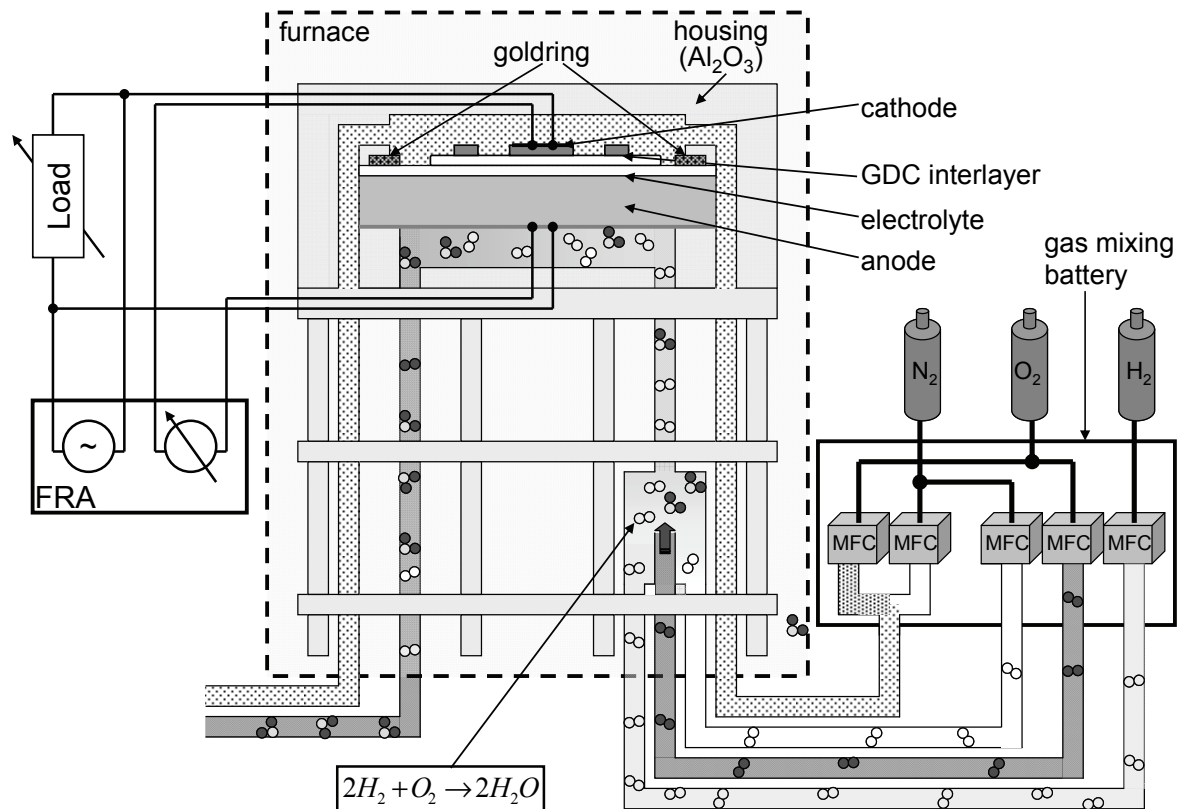
Fig. 19: Sketch of the setup used for a precise adjustment of gas composition, showing the electrical contacting in the furnace and the measuring equipment (FRA). The gas composition in the combustion chamber can precisely be adjusted by means of the „gas mixing battery" which consists of MFC's (mass flow controllers), and the pre-chamber in the furnace in which, owing to the high temperature (500...850 °C), inflowing oxygen instantaneously reacts with the hydrogen to form water.

3.3 Cell Measurements

Impedance spectroscopy was carried out using a Solartron 1260 FRA (frequency response analyser) at frequencies between 30 mHz and 1 MHz. The current amplitude was chosen in such a way that the voltage response never exceeded a value of 12 mV rms. For the cell type investigated, the internal resistance ranged from about 2 Ω at 650 °C down to 0.1 Ω at 850 °C. Correspondingly, the amplitude of the excitation current ranged from 6 to 60 mA rms (technical upper limit of the FRA output current). All impedance measurements performed within this work were carried out under open-circuit conditions [except for the measurements yielding the charge transfer coefficients α_{an} and α_{cat} (cp. Fig. 47 in chapter 4.3.1)].

I-U measurements were carried out with current densities up to 2 A/cm^2 and cell voltages not below a limit of 0.6 V. This operation range guaranties a stable cell performance during all experiments.

Several impedance curves were measured under specifically varied conditions, thereby only varying one operating condition (i.e. temperature, ($T \in \{871\text{-}571\}$ °C) oxygen partial pressure at the cathode ($pO_{2,cat} \in \{0.21, 0.13, 0.04, 0.02, 0.01\}$ atm), fuel utilization ($\beta \in \{4.0\text{-}65.0\}$ %), hydrogen partial pressure ($pH_{2,an} \in \{0.05, 0.20, 0.40, 0.80\}$ atm) or water partial pressure ($pH_2O_{an} \in \{0.04, 0.12, 0.20, 0.40\}$ atm) at the anode) at a time.

3.4 Measurement Data Quality

For a successful interpretation of impedance curves the measurement data quality is of crucial importance. The quality and amount of information that can be extracted from impedance data is implicitly connected to the noise-level and the compliance of the measured curve with the principles of causality, linearity and stability.

A well established method used to asses the consistency and quality of measured impedance spectra is the Kramers-Kronig validation [12]. The Kramers-Kronig relations are integral equations, which constrain the real and imaginary components of the impedance for systems that satisfy the conditions of causality, linearity, and stability [12].

In this work the necessary compliance of the measured data with the Kramers-Kronig transformation rules is verified by using the "KK test for Windows" software [38, 39]. Fig. 20 shows a Kramers-Kronig validation for a typical impedance spectrum. For most part of the spectrum the relative errors of both real and imaginary data lie below a very low value of 0.4 %.
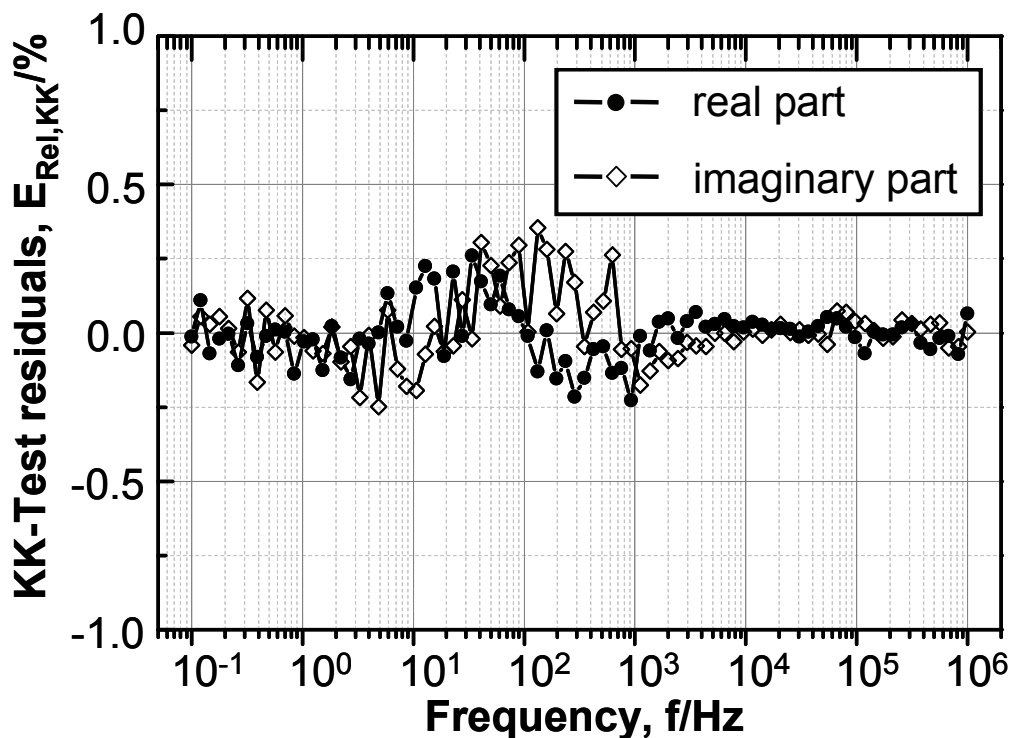
Fig. 20: Kramers–Kronig test residuals of a typical impedance spectrum, calculated with the "KK test for Windows" software [38, 39].

4 Results and Discussion

In the first part of this chapter the equivalent circuit model (ECM) of the ASC cells, analysed within this work, is developed. With the help of this ECM the measured impedance spectra are separated into the single loss contributions, thus permitting a precise determination of the area-specific resistance values for the single loss contributions of the SOFC single cells.

In the second part of the chapter the developed ECM is applied to determine the surface exchange kinetics and oxygen ion bulk diffusion properties (k^δ and D^δ) of mixed ionic-electronic conducting (MIEC) cathodes, directly from electrochemical impedance spectroscopy (EIS) measurements on ASCs.

Finally a zero-dimensional stationary model for the current-voltage (I-U) characteristics of the ASC is presented.

4.1 Equivalent Circuit Development

In order to develop a physico-chemical equivalent circuit model of the analysed ASC single cells the performance-related polarisation processes have to be identified and proven.

Commonly the obtained impedance spectra are analysed by a Complex Nonlinear Least Squares (CNLS) approximation to a model function represented by an equivalent circuit [7]. In this case the equivalent circuit model needs to be defined a priori without any knowledge about the real number of polarisation processes contributing to the overall polarisation loss of the cell. This leads very often to a severe ambiguity of the adopted model [6].

To overcome that disadvantage an alternative approach for analysing impedance spectra is used in this work. The equivalent circuit model and the optimal starting parameters for the CNLS algorithm are obtained by a preidentification of the impedance response by calculating and analysing the corresponding distribution function of relaxation times (DRT) as reported in details in [28]. The DRT approach is particularly advantageous for the analysis of (anode supported) SOFC single cells coupled to thin electrolytes (thickness less than 20 μm), where reference electrodes are not applicable for the separation of anode and cathode losses [27].

4.1.1 Process Identification

DRT Analysis

The higher resolution of the DRT allows the identification of losses with characteristic frequencies separated by only half a decade as demonstrated by the comparison of a typical impedance spectrum of an ASC (Fig. 21a) and the corresponding DRT (Fig. 21b). Unlike the impedance curve where the individual polarisation processes overlap, at least five processes (P_{1C}, P_{1A}, P_{2C}, P_{2A}, and P_{3A}) can be clearly distinguished in the calculated DRT.

To identify all polarisation processes contributing to the overall polarisation loss of the cell and investigate their parameter dependency, a series of impedance measurements was carried out in which only one cell parameter at a time was varied (cathodic oxygen partial pressure, fuel utilization and temperature). In the following sections the calculated DRTs are analysed with respect to their operating parameter dependency.
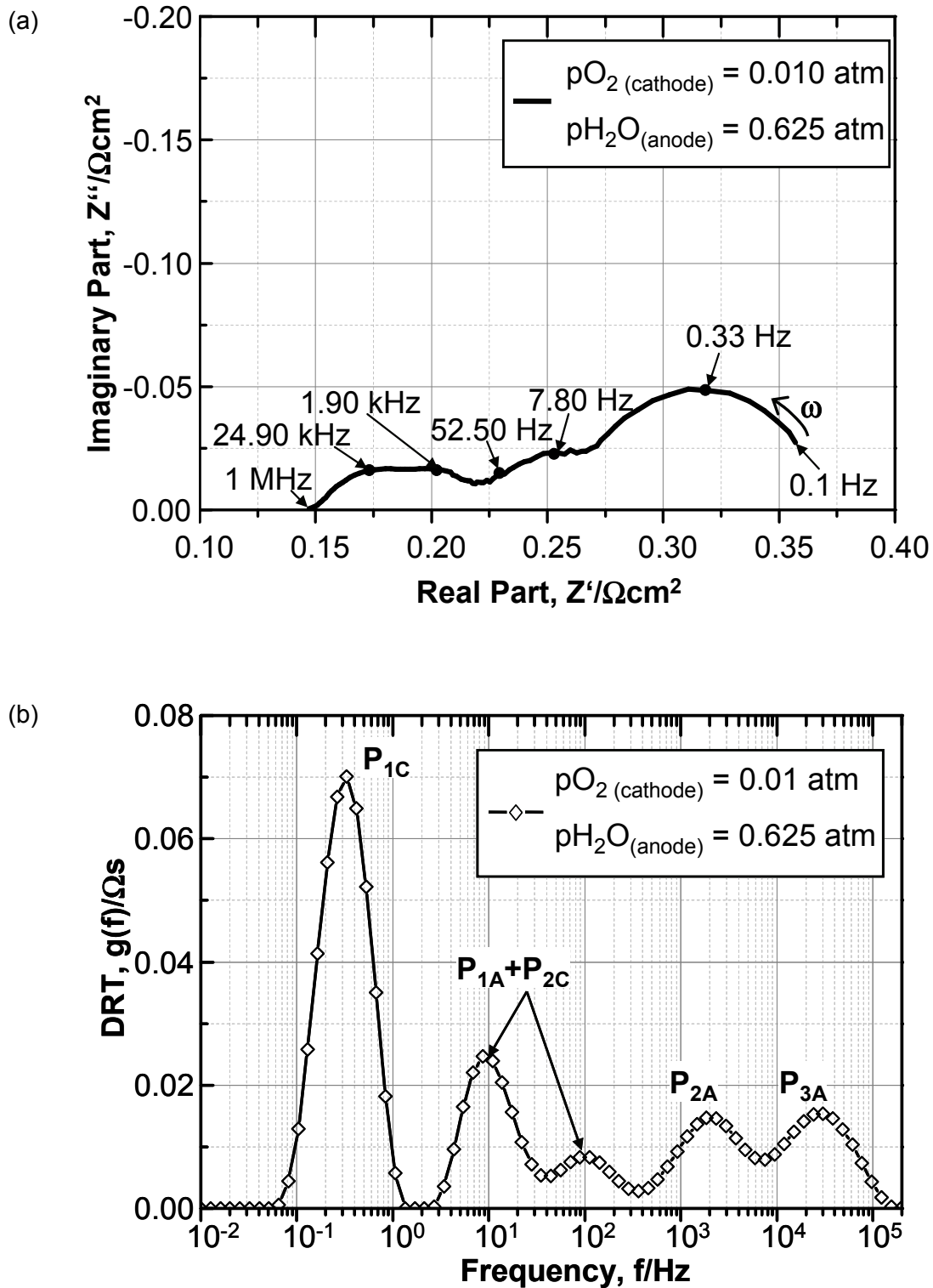
Fig. 21: (a) typical impedance spectra of an anode supported cell with L58SCF cathode recorded at T = 800 ºC, $pO_{2,cat}$ = 0.01 atm, pH_2O_{an} = 0.625 atm and (b) corresponding distribution function of relaxation times (DRT). Unlike the Nyquist plot, at least 5 processes are visible in the distribution curve [cell# Z1_153].

<u>Variation of Temperature</u>

Typical impedance spectra and corresponding DRTs of an ASC cell at four different temperatures (730, 750, 800, and 860 °C) are shown in Fig. 22. The impedance spectra were measured at a fuel gas composition of 62.5 % H_2O and 37.5 % H_2. Air was used as cathode gas.

It is evident that the processes P_{2C}, P_{2A} and P_{3A} are all characterised by a pronounced thermal activation. Process P_{1A} shows, by contrast, a negligible dependency on the operating temperature.
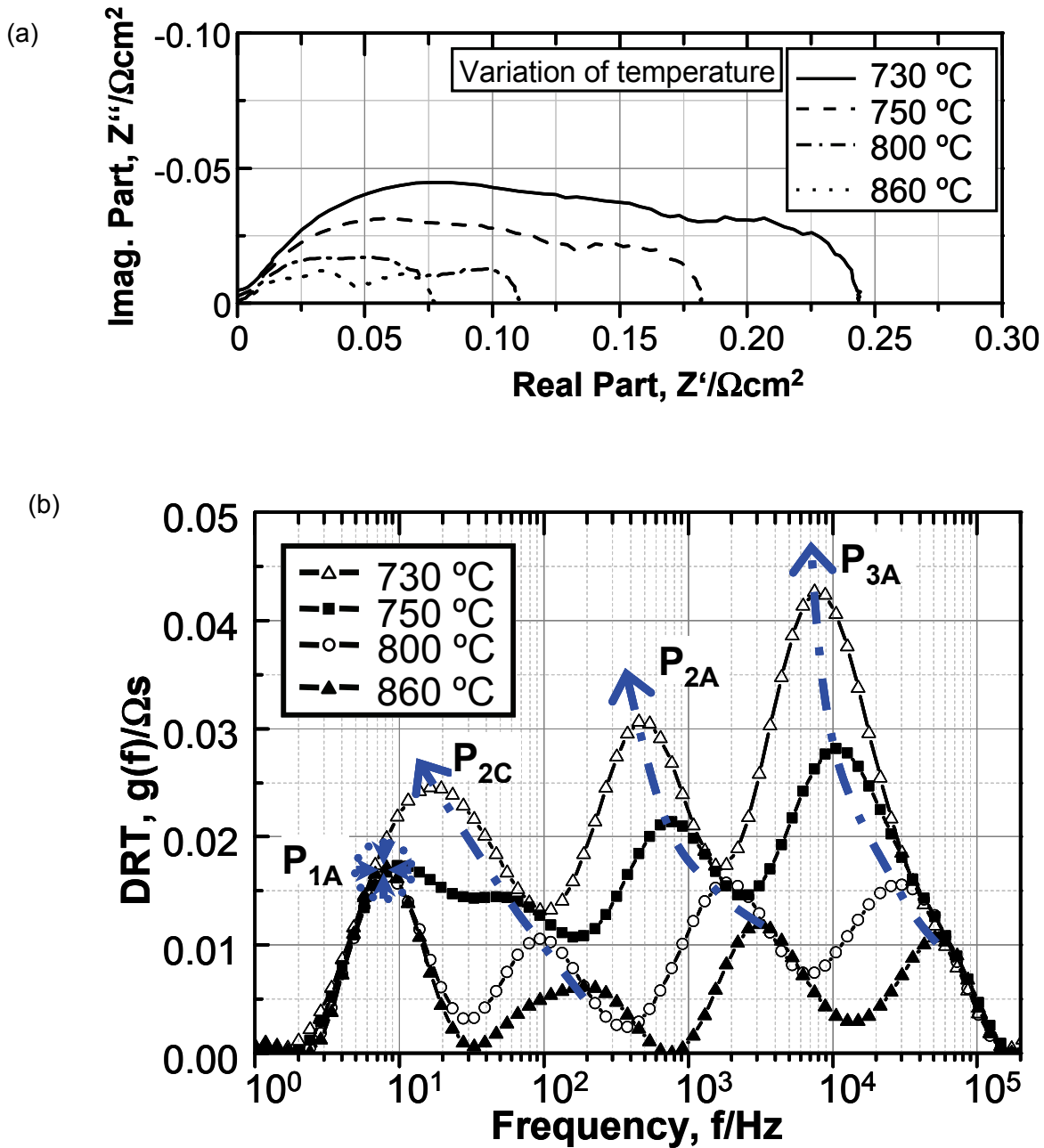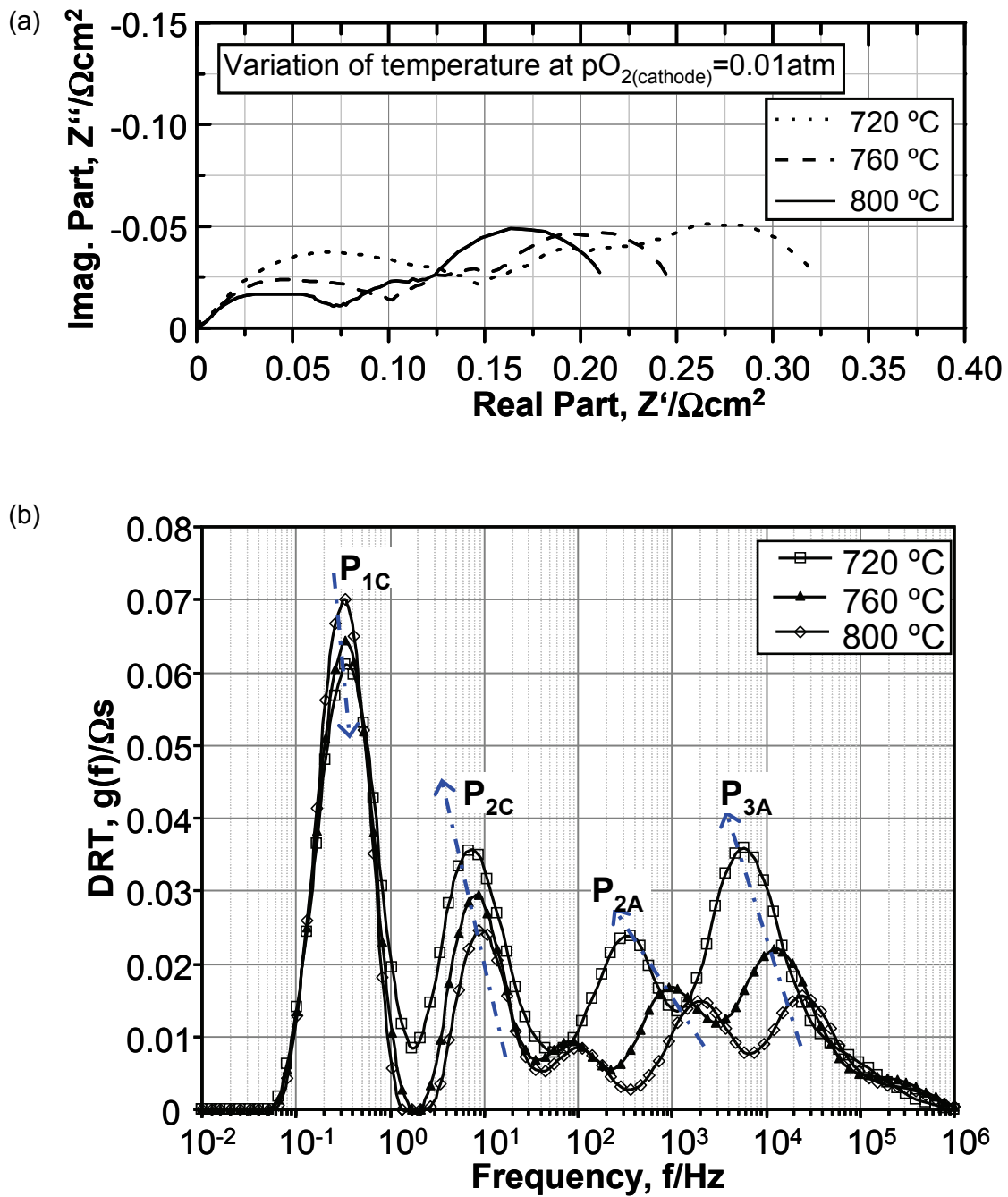

Fig. 22: (a) Series of impedance spectra (ohmic part subtracted) and (b) corresponding distribution curves at four temperatures. [pH_2O_{an} = 0.625 atm (balance H_2), $pO_{2,cat}$ = 0.21 atm (air) [cell# Z1_153].

Variation of Anodic Water Partial Pressure

In order to identify the anodic processes and their dependency on the partial pressure of water (pH_2O_{an}) in the fuel gas the H_2O content was varied stepwise between 4.88 % and 62.5 % (balance H_2). Air was used as cathode gas.

Fig. 23b shows the DRTs computed from impedance spectra (Fig. 23a) recorded at four different pH_2O_{an}. The processes P_{1A} and P_{2A} show both a significant dependency on the water content in the fuel gas, whereas process P_{3A} is characterised by a minor dependency.

Particular attention should be paid to process P_{1A}. As will be shown later, in the equivalent circuit this process is modelled by a generalised finite length Warburg element (G-FLW) accounting for the diffusion loss within the anode substrate. As discussed in chapter 2.6.2 the DRT of a G-FLW-element exhibits a large peak located at the characteristic frequency followed by smaller peaks at higher frequencies. Depending on the operating conditions this fact makes it difficult to identify the process P_{2C} as this has a maximum in a frequency range similar to that of the two major P_{1A} peaks, i.e., between 10 and 100 Hz, thus leading to a possible overlap of the peaks characteristic of both P_{1A} and P_{2C} (cp. Fig. 22b).

Variation of Cathodic Oxygen Partial Pressure

The oxygen content of the gas mixture supplied to the cathode was varied between 21 % (air) and 1 % (balance nitrogen), whereas the composition of the fuel gas was kept constant at a ratio 62.5 % H_2O to 37.5 % H_2. The high water content was used to reduce the anodic polarisation losses to a minimum (cp. Fig. 23b) thereby making the deconvolution of the cathodic contributions simpler.

Fig. 24b shows the influence of the oxygen partial pressure ($pO_{2,cat}$) on the distribution of relaxation times (the corresponding impedance spectra are shown in Fig. 24a). It is clearly visible how a new process (denoted as P_{1C}) evolves in the frequency range below 10 Hz at oxygen contents ≤ 0.05 atm. At the same time the process P_{2C}, already identified in Fig. 22, is shifted towards lower frequencies, thus strongly overlapping with the two major peaks between 7 and 100 Hz related to the process P_{1A} (see arrows on P_{1A} in Fig. 24b).

In order to analyse the temperature dependence of the newly identified process P_{1C}, additional impedance measurements were conducted at three different temperatures (Fig. 25a) and at the lowest oxygen partial pressure ($pO_{2,cat}$ = 0.01 atm). Fig. 25b shows the DRTs computed from the impedance spectra. P_{1C} is characterised by a minor dependency on the operating temperature showing a slight decrease by decreasing temperature.

(a)

(b)
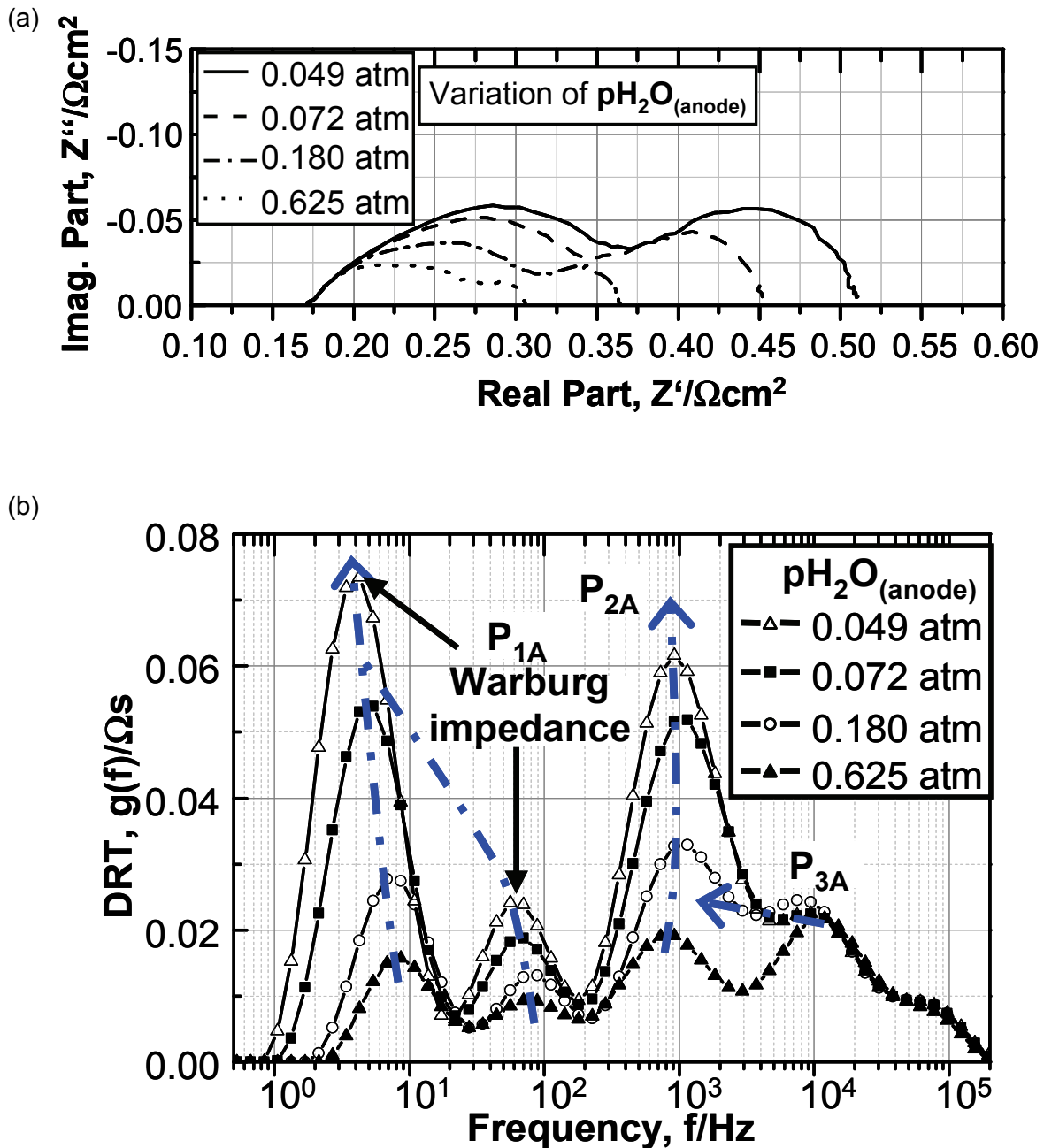
Fig. 23: (a) Series of impedance spectra and (b) corresponding distribution curves at four different pH_2O_{an}. [$pO_{2,cat}$ = 0.21 atm (air), T = 757 ºC] [cell# Z1_153].
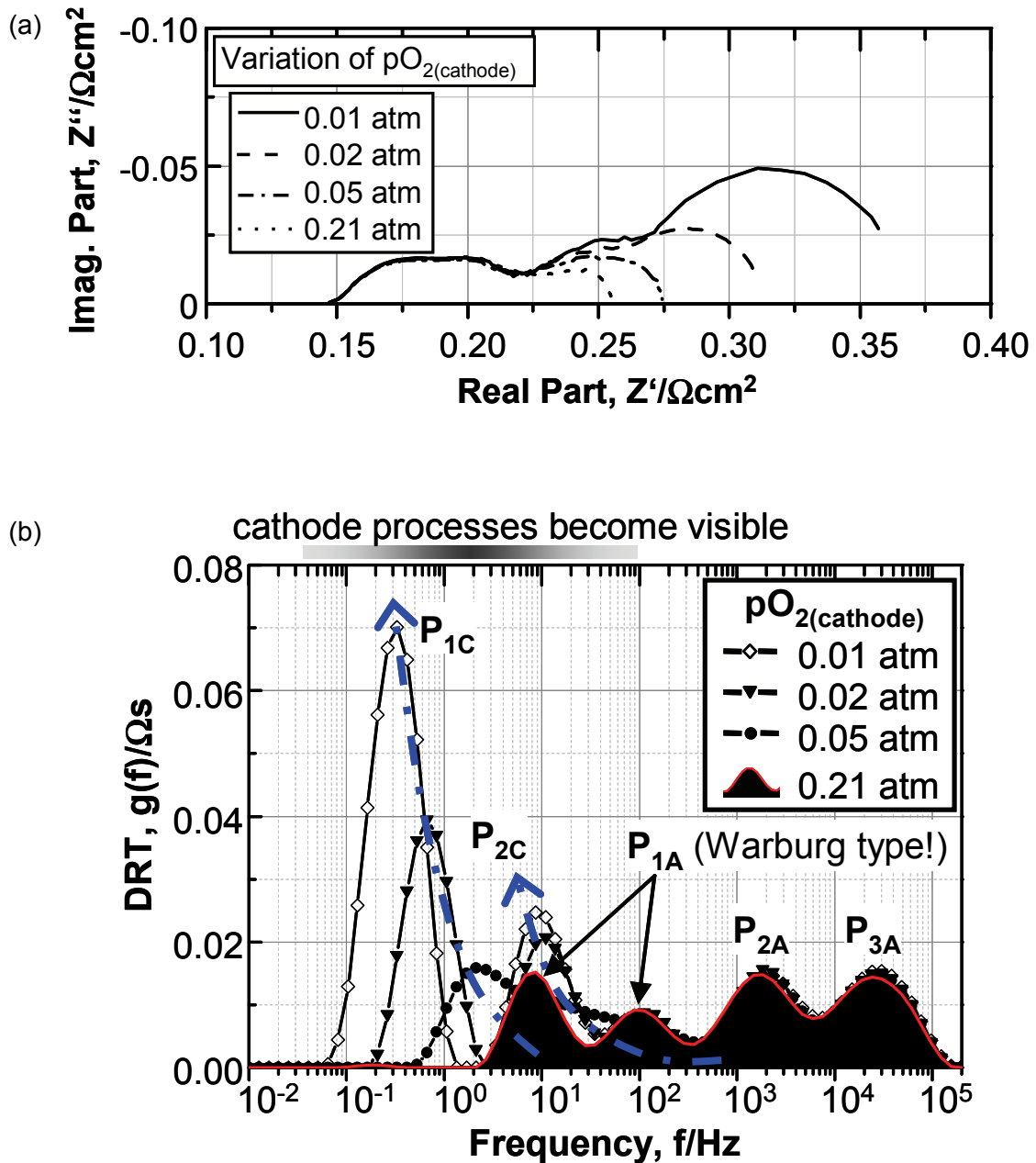
Fig. 24: (a) Series of impedance spectra and (b) corresponding distribution curves at four different $pO_{2,cat}$. [pH_2O_{an} = 0.625 atm (balance H_2), T = 800 °C] [cell# Z1_153].

(a)

(b)

Fig. 25: (a) Series of impedance spectra (ohmic part subtracted) and (b) corresponding distribution curves for three different temperatures at very low cathodic oxygen partial pressure. [pH_2O_{an} = 0.625 atm (balance H$_2$), $pO_{2,cat}$ = 0.01 atm] [cell# Z1_153].

Conclusions

The observations made above suggest that the overall polarisation loss caused by the cathode is strongly related to the two processes P_{1C} and P_{2C}. On the other side P_{1A}, P_{2A} and P_{3A} show a more or less pronounced dependence on pH_2O_{an} but no dependency on the $pO_{2,cat}$ demonstrating that this three processes are ascribable to the anode.

Based on the analysed characteristic dependencies of the identified processes a first hypothesis about their physical origin can be made:

-the processes P_{1A} and P_{1C} exhibit a very low thermal activation behaviour (a negligibly small (even negative) activation energy). Moreover, both processes are strongly affected by gas composition changes. All of these are telltale signs, that P_{1C} and P_{1A} are related to gas-phase diffusion [14, 41].

-the processes P_{2C} P_{2A} and P_{3A} are characterised by a pronounced thermal activation, therefore these losses are most likely related to the activation polarisation in the anode and cathode, respectively.

Table 1 gives an overview of the processes identified by the DRT analysis together with their characteristic frequency range, gas partial pressure and temperature dependency.

Table 1: List of processes identified from DRT analysis, together with their characteristic frequency range, gas partial pressure and temperature dependency.

Process	f_{max},	Dependencies	Assigned Electrode
P_{1C}	0.3...10 Hz,	$pO_{2,cat}$, Temperature (low)	cathode
P_{2C}	2...500 Hz,	$pO_{2,cat}$, Temperature	cathode
P_{1A}	4...10 Hz,	$pH_{2,an}$, pH_2O_{an}, Temperature (low)	anode
P_{2A}	200 Hz...3 kHz,	$pH_{2,an}$, pH_2O_{an},Temperature	anode
P_{3A}	3...50 kHz,	$pH_{2,an}$, pH_2O_{an}, Temperature	anode

4.1.2 Equivalent Circuit Model Definition and Validation

Based on the extensive DRT analysis shown above the equivalent circuit model depicted in Fig. 26 is proposed. The equivalent circuit consists of six serial impedance elements: the processes P_{1C}, P_{2A} and P_{3A} are modelled by an RQ-element, whereas P_{1A} and P_{2C} are modelled by a G-FLW-element and a Gerischer-element, respectively. The ohmic losses are accounted by an ohmic resistor R_0. The impedance expressions of the aforementioned impedance elements have been discussed in chapter 2.5 and are shortly summarised in the right part of Fig. 26.

$$\underline{Q}(\omega) = \frac{1}{(j\omega)^{n_Q}\, Y_Q}$$

$$\underline{Z}_W(\omega) = R_W \cdot \frac{\tanh\left[(j\omega T_W)^{n_W}\right]}{(j\omega T_W)^{n_W}}$$

$$\underline{Z}_G(\omega) = \frac{R_{chem}}{\sqrt{1 + j\omega t_{chem}}} \quad \begin{array}{l} R_{chem} \equiv R_{2C} \\ t_{chem} \equiv t_{2C} \end{array}$$

cathode gas diffusion only at $pO_2 \ll 0.21$
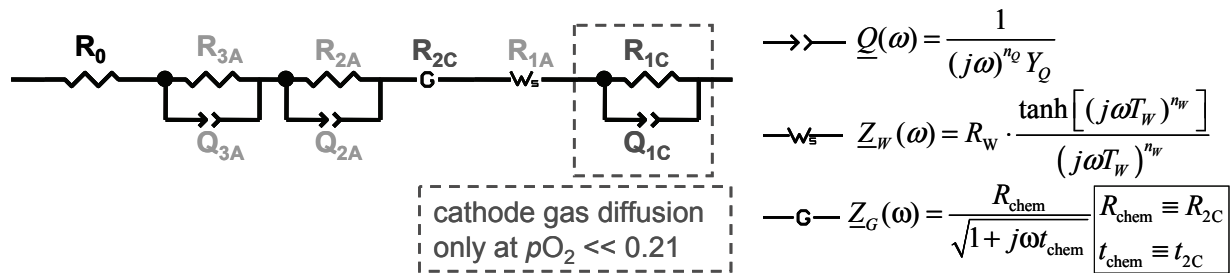
Fig. 26: Proposed equivalent circuit model for the CNLS-fit analysis of impedance spectra.

Fig. 27a shows a typical CNLS fit result applied to the imaginary part of the impedance curve depicted in Fig. 21a before. The residuals (relative errors) are distributed uniformly around the frequency axis showing no systematic deviation (Fig. 27b). For most part of the spectrum the relative errors lie below an absolute value of 0.25 %. Only from approx. 300 kHz upwards inductive artefacts caused by the electrical wiring becomes noticeable. The high quality of this CNLS fit confirms the plausibility of the proposed equivalent circuit. However, as already stated in chapter 2.6.1, the residuals are "only" a mathematical quantity that describes the level of equivalency between the measured curve and the theoretical impedance spectrum of the proposed model. Therefore, no ultimate conclusion about the physical correctness of the ECM is allowed from just evaluating the residuals. Hence, to prove the physical validity of a proposed ECM, impedance spectra recorded over a wide range of operating conditions (various gas compositions and temperatures) were analysed by CNLS approximation. In this way the equivalent circuit parameters could be evaluated with regard to physical considerations.

(a)

(b)
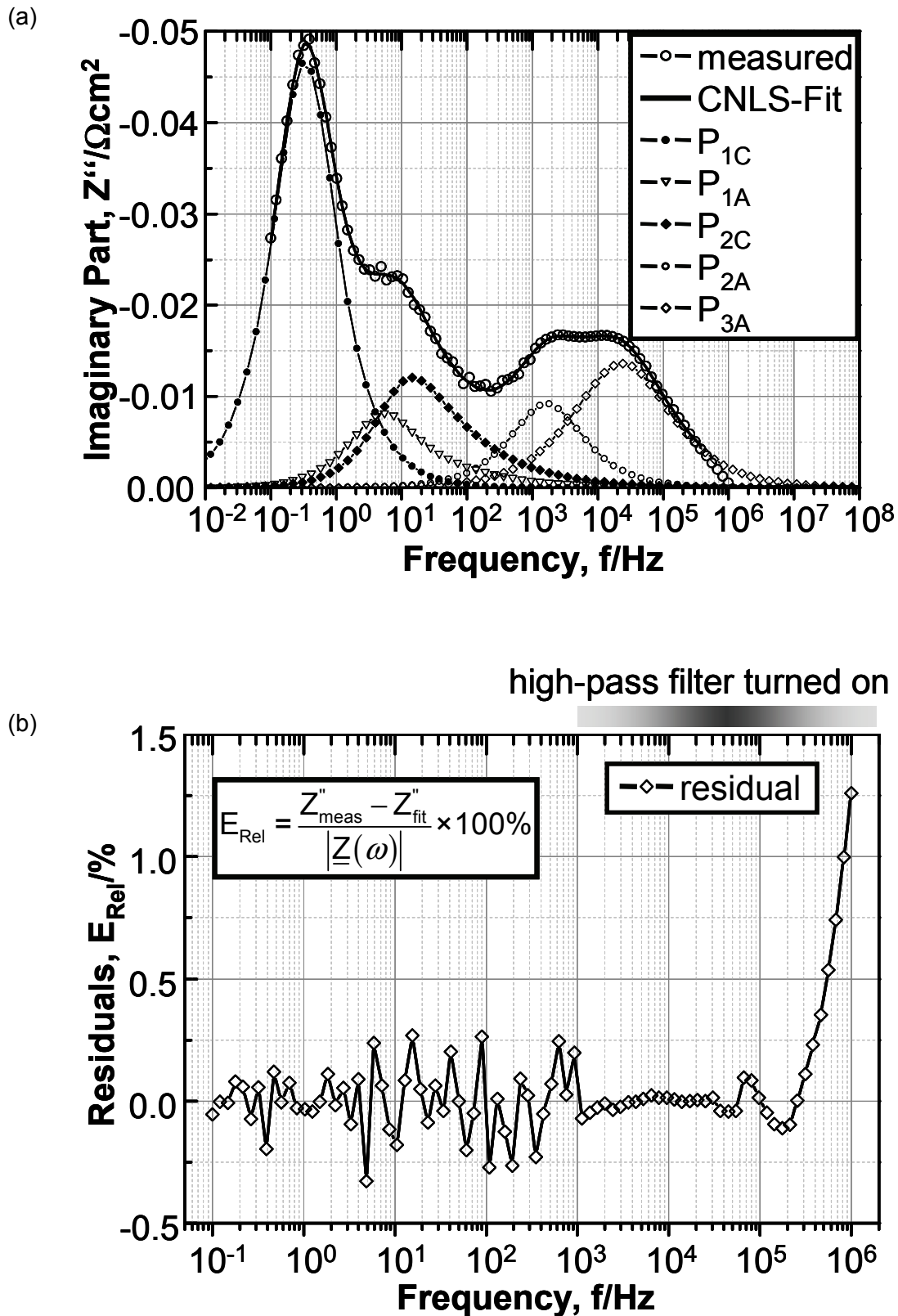
Fig. 27: (a) CNLS fit of the imaginary part of the impedance spectrum shown in Fig. 21a. (b) Residual pattern of the fit [cell# Z1_153].

Cathodic Oxygen Partial Pressure Dependency

In Fig. 28 the polarisation resistances obtained by the CNLS fit (using the equivalent circuit depicted in Fig. 26) are plotted over the partial pressure of oxygen. It should be mentioned that in this case the resistance R_{1A} was kept fixed during the entire fit procedures. This approach was essential because otherwise the similar summit frequencies of P_{1A} and P_{2C} (especially at lower $pO_{2,cat}$) would have destabilised the fit algorithm.

In accordance with the DRT analysis (Fig. 24 before) R_{2A} and R_{3A} are independent on the change in O_2, whereas the two resistances R_{1C} and R_{2C} show both an almost linear trend in the double logarithmic plane with a slope of -1.08 and -0.26 respectively. The slope of R_{2C} is in accordance with literature values obtained on symmetrical LSCF cells. For instance, Esquirol et al. [42] report a slope of -0.21 for the resistance associated with the activation polarisation of a $La_{0.6}Sr_{0.4}Co_{0.2}Fe_{0.8}O_{3-\delta}$ cathode.
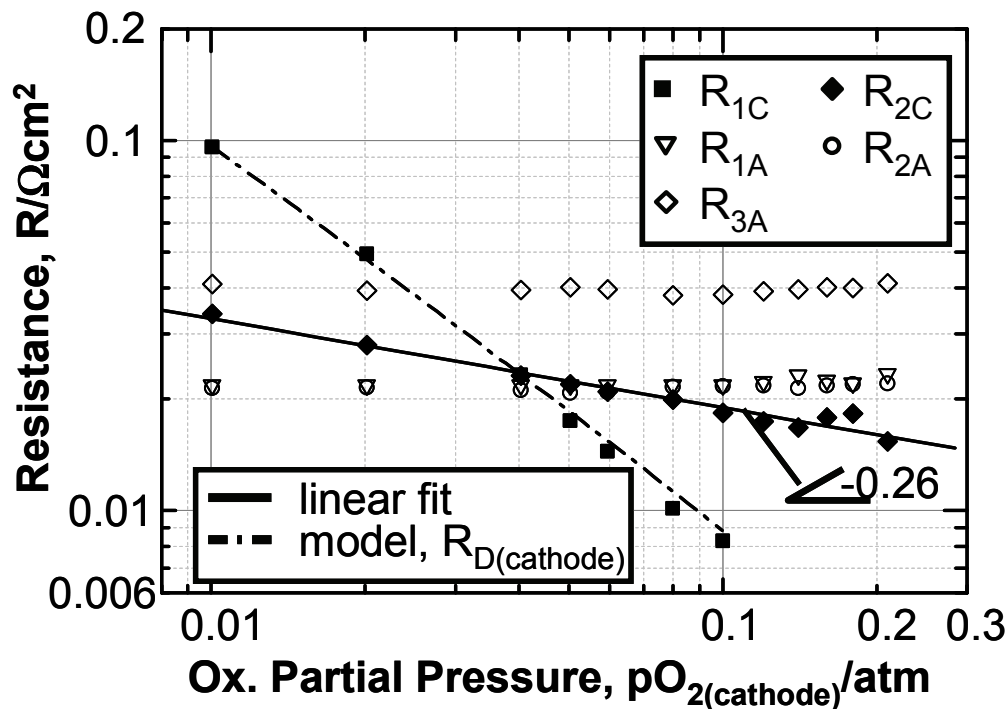
Fig. 28: Characteristic dependence of fitted equivalent circuit elements on the cathodic oxygen partial pressure. The dashed line indicates the model prediction according to Eq. 4.1 [pH_2O_{an} = 0.625 atm (balance H_2), T = 800 ºC] [cell# Z1_153].

In the following we will focus our attention on process P_{1C}. It can easily be shown that the cathodic gas diffusion resistance can be described by the following equation [15, 40],

$$R_{D(cathode)} = \left(\frac{RT}{4F}\right)^2 L_{cat} \frac{1}{D_{O_2,N_2}^{eff}} \left(\frac{1}{pO_{2,cat}} - 1\right)\left(1.0133 \cdot 10^5 \frac{Pa}{atm}\right)^{-1} \qquad \text{Eq. 4.1}$$

Where L_{cat} is the cathode thickness and $D^{eff}_{O_2,N_2}$ is the effective diffusion coefficient for a mixture of oxygen and nitrogen. R, T and F have their usual meaning.

The model equation 4.1 was fitted to the experimental data with the effective diffusion coefficient $D^{eff}_{O_2,N_2}$ representing the unknown variable (L_{cat} was set to 45 μm). The fit result is shown in Fig. 28 (dashed line). As can be seen, the agreement between the model and the experimentally obtained resistance R_{1C} is quite good. From the fit $D^{eff}_{O_2,N_2} = 2.5 \cdot 10^{-6}$ m^{2}s^{-1} is estimated. This value is in accordance with values reported in the literature for this type of cathode structure [43]. This result strongly supports the hypothesis that the low frequency process P_{1C} reflects the mass transfer resistance caused by the gas phase diffusion in the pores of the L58SCF electrode. (N.B.: in chapter 4.3.1 a more detailed analysis will be given; taking in to account the porosity, tortuosity and Knudsen-Diffusion effects).

Anodic Water Partial Pressure Dependency

In Fig. 29 the polarisation resistances obtained from the CNLS fit are plotted over the water partial pressure (balance H$_2$). During this fit procedure the resistance R_{2C} was kept fixed in order to ensure a stable fit. The polarisation contribution caused by the gas phase diffusion in the pores of the LSCF electrode can be neglected when air is used as cathode gas, thus the resistance R_{1C} was set fixed to zero. The two resistances R_{2A} and R_{3A} show both an almost linear trend in the double logarithmic plane with a slope of -0.44 and -0.20 respectively. R_{1A} shows the highest dependence on changes in the water content.
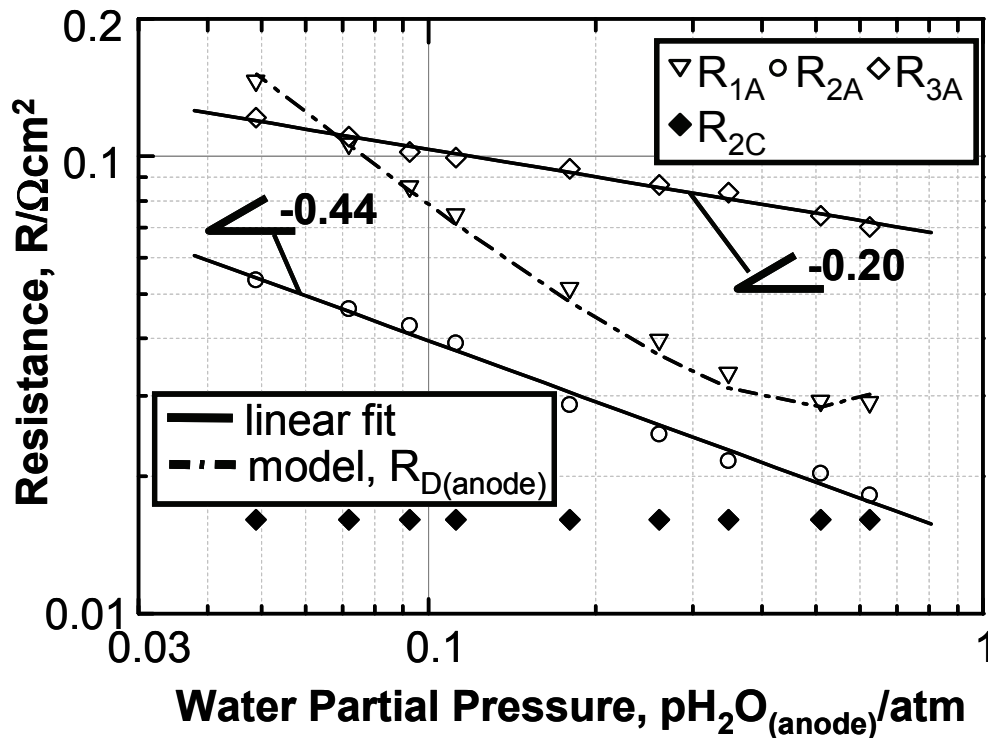
Fig. 29: Characteristic dependence of fitted equivalent circuit elements on the anodic partial pressure of water (balance H₂). [$pO_{2,cat}$ = 0.21 atm (air), T = 757 ºC] [cell# Z1_153].

In the following we will focus our attention on process P_{1A}. As discussed in chapter before, P_{1A} is characterised by a negligible thermal activation and shows attributes that are expected to be seen by gas diffusion processes [14]. To support this hypothesis the following widely used Eq. 4.2, describing the resistance caused by diffusion limitations in a porous anode structure, has been employed [14, 40],

$$R_{D(anode)} = \left(\frac{RT}{2F}\right)^2 L_{an} \frac{1}{D^{eff}_{H_2O,H_2}} \left(\frac{1}{pH_{2,an}} + \frac{1}{pH_2O_{an}}\right) \left(1.0133 \cdot 10^5 \frac{Pa}{atm}\right)^{-1} \qquad \text{Eq. 4.2}$$

where L_{an} is the anode thickness (in this case 1.5 mm). $D^{eff}_{H_2O,H_2}$ represents the effective diffusion coefficient which may depend on porosity and tortuosity of the electrode as well as the effects of Knudsen diffusion.

Eq. 4.2 was fitted to the experimental data with $D^{eff}_{H_2O,H_2}$ representing the unknown variable. The fit result is shown in Fig. 29 (dashed line). As can be seen, the model approximates very well the trend of the experimentally obtained resistance R_{1A}. From the fit a quite reasonable effective diffusion coefficient $D^{eff}_{H_2O,H_2} = 4.12 \cdot 10^{-5} m^2 s^{-1}$ is estimated. This result strongly supports the hypothesis that the low frequency process P_{1A} reflects the mass transfer resistance caused by the gas phase diffusion in the pores of the Ni/YSZ-anode substrate.

(N.B.: in chapter 4.3.1 a more detailed analysis will be given; taking in to account the porosity, tortuosity and Knudsen-Diffusion effects).

Thermal Activation

Here it should be briefly noted that in a first work of Leonide et al. [40] (cf. Fig. 28 and Fig. 29) the temperature dependent resistances R_{2A} and R_{3A} were treated separately. However later extensive work [44, 45] has demonstrated that the two identified processes P_{2A} and P_{3A} are related to three coupled processes, all of them taking place in the anode functional layer:

1. The oxygen ion transport within the YSZ matrix of the anode.

2. The charge transfer resistance at the TPB Ni/YSZ/gas phase.

3. The gas diffusion loss inside the anode functional layer.

For this reason the resistances R_{2A} and R_{3A} should not be considered separately but only as a sum, describing the overall polarisation resistance caused by the interaction of the three processes listed above. However, the gas diffusion loss inside the 7 µm thick anode functional layer (AFL) can be neglected after appositely activating the cell: the AFL is a dense layer after initial reduction. It lasts several hours (approx. 150 h) of cell operation until a certain open porosity in the AFL structure is reached. From there on gas diffusion in the AFL can be neglected for cells with an AFL thickness (t_{AFL}) smaller than 8 µm, i.e. for the cell type analysed within this study (cf. Appendix-Chapter 6.1) [45].

The resistances R_{2C}, and ($R_{2A}+R_{3A}$) obtained by the CNLS fit of the impedance curves recorded on a FZJ ASC cell are plotted over the temperature in Fig. 30. In order to facilitate the fit procedure the resistance R_{1A}=38 mΩ·cm^2 was kept fixed (constant).

As can be seen, the resistances R_{2C} and ($R_{2A}+R_{3A}$) can be approximated very well with a linear fit, demonstrating an almost perfect Arrhenius behaviour. From the slope of the fitted lines the activation energies $E_{a,2C}$ = 1.45 eV and $E_{a,3A}$ = 1.09 eV are obtained. A detailed discussion on the obtained activation energies along with a comparison to literature data is given in the subsequent chapters 4.2 and 4.3. Nevertheless, this result strongly supports the hypothesis that the processes ($P_{2A}+P_{3A}$) and P_{2C} are related to the activation polarisation in the anode and cathode, respectively.
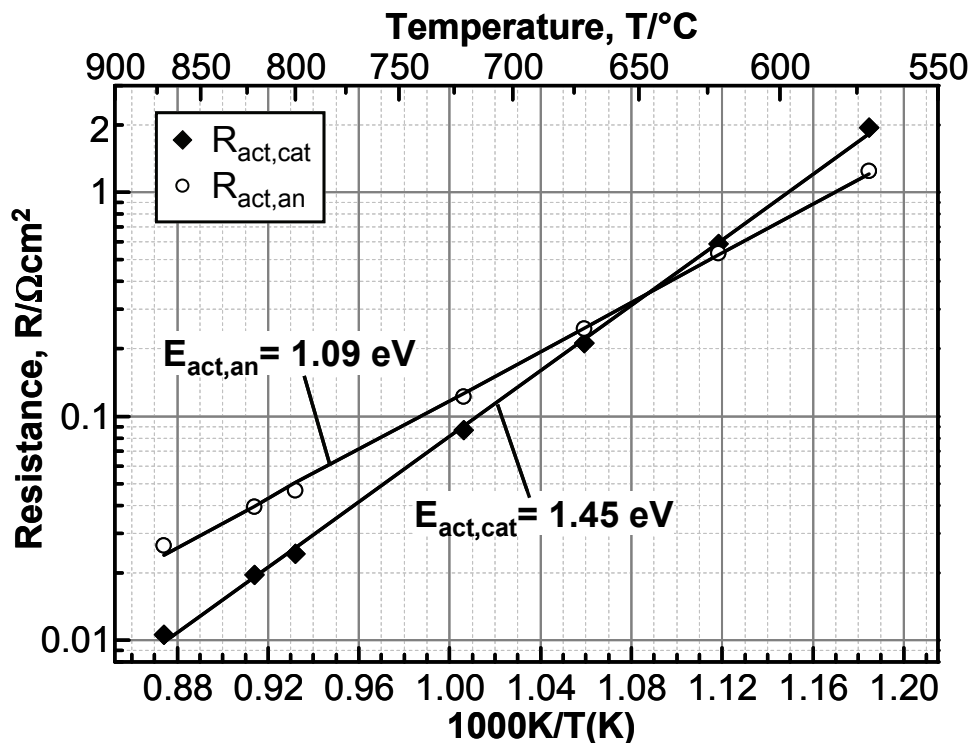
Fig. 30: Characteristic dependence of fitted equivalent circuit elements on the operating temperature. [pH_2O_{an} = 0.20 atm (balance H$_2$), $pO_{2,cat}$ = 0.21 atm (air)] [cell# Z1_188].

Conclusions

In summary the presented CNLS analysis confirms all hypotheses made in the chapter before. P_{1A} occurs owing to inhibited gas diffusion within the Ni/YSZ anode substrate. The high-frequency processes P_{2A} und P_{3A} are related to gas diffusion coupled with charge transfer reaction and ionic transport in the Ni/YSZ anode functional layer structure. The two processes P_{1C} and P_{2C} are cathodic processes: P_{1C} characterizes the gas diffusion losses within the pores of the cathode (and is, thus, negligible in air), whereas the faster process P_{2C} is inherently electrochemical, accounting for the losses resulting from oxygen incorporation and oxygen ion transport within the cathode (LSCF).

In Fig. 31 a schematic fit result of a typical measured impedance curve along with the simulated Nyquist plots of each single impedance element is shown.

Table 2 gives a final overview of the processes identified by the DRT analysis together with their characteristic frequency (f_{max}) range, gas partial pressure, temperature dependency and physical origin.
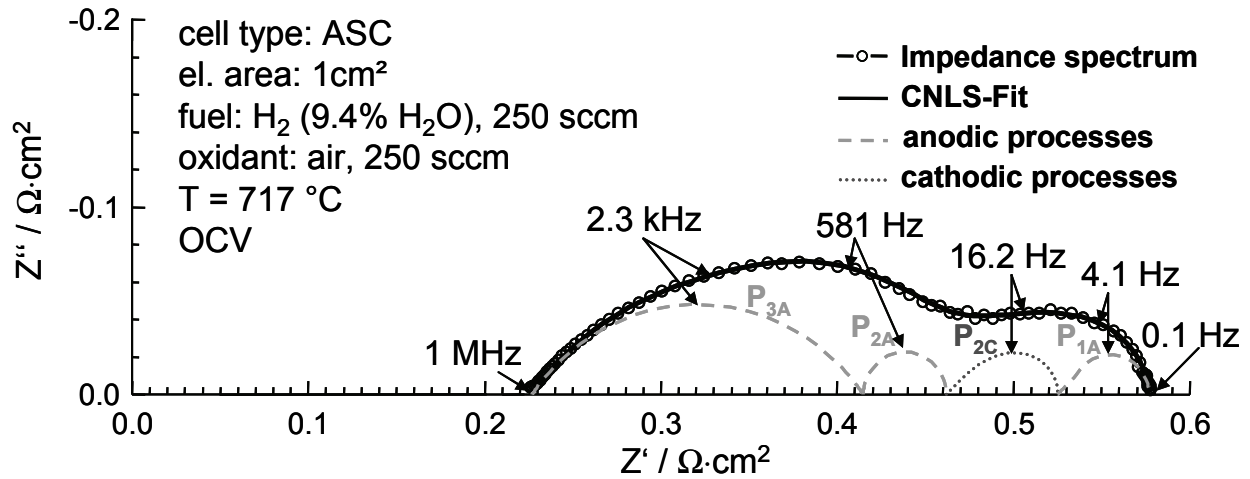
Fig. 31: Schematic fit result of a typical measured impedance curve along with the simulated Nyquist plots of each single impedance element (cf. Fig. 26) [cell# Z1_153].

Table 2: List of the processes known to take place in a ASC cell, together with their temperature, gas partial pressure and frequency dependencies as well as the magnitude of the real part of the according resistance [(T = 570 - 870 °C, H_2O ≈ 5.5 – 65 % (balance H_2) at the anode and O_2 ≈ 1.0 – 21 % (balance N_2) at the cathode].

Process	Element	f_{max}, ASR	Dependencies	Physical Origin
P_{1C}	RQ $n_{Q,1C}$≈0.97	0.3...10 Hz, 2...100 mΩcm²	$pO_{2,cat}$, T (very low)	gas diffusion in the cathode structure
P_{2C}	Gerischer	2...500 Hz, 10 mΩcm²...2 Ωcm²	$pO_{2,cat}$, T	oxygen surface exchange kinetics and O^{2-} diffusivity in the bulk of the cathode
P_{1A}	G-FLW $n_{W,1A}$=0.45...0.49	4...10 Hz, 20...150 mΩcm²	pH_2, pH_2O, T (very low)	gas diffusion in the anode substrate
P_{2A} + P_{3A}	RQ $n_{Q,2A}$=0.89...0.95 RQ $n_{Q,3A}$=0.65...0.75	200 Hz...3 kHz, 3...50 kHz, R_{2A}+R_{3A} 10 mΩcm²...2 Ωcm²	$pH_{2,an}$, pH_2O_{an}, T $pH_{2,an}$, pH_2O_{an}, T	(P_{2A}+P_{3A}) gas diffusion coupled with charge transfer reaction and ionic transport (AFL: anode functional layer)

4.2 Evaluation of Oxygen Exchange and Diffusion Coefficients

Improving mixed ionic-electronic conducting (MIEC) materials is a major goal of research in solid oxide fuel cells, particularly for operation at intermediate temperatures (IT-SOFC). Promising (MIEC) cathode materials are identified by their area specific resistance (ASR), attributed to (i) a custom-tailored microstructure and (ii) chemical composition. The latter is inevitably linked to the surface chemical exchange ($k^{\delta} \equiv k_{chem}$) of O_2 and to solid-state oxygen ion diffusion ($D^{\delta} \equiv D_{chem}$). In general, k and D are assessed by measurements performed on dense bulk samples (i.e. conductivity relaxation experiments (k^{Q}, D^{Q}), tracer experiments (k^*, D^*) or on symmetrical electrode configurations (k_{chem}, D_{chem}) [46, 47].

However, a characterisation method capable to analyse k^{δ} and D^{δ} of the "real" cathode (as deposited on the ASC) would be highly valuable. This approach would disclose degradation phenomena correlated to microstructural changes (i.e. variations of grain sizes and effective surface area) and/or compositional changes (i.e. cation demixing, reactions with neighbour materials). These effects can not be fully quantified in dense bulk samples or symmetrical cathode configurations which have undergone, unavoidable, different preparation routes compared to the "real" MIEC cathode as deposited on the ASC.

This section will introduce an approach showing promise to determine the surface exchange kinetics and oxygen ion bulk diffusion properties (k^{δ} and D^{δ}) of mixed ionic-electronic conducting (MIEC) cathodes from electrochemical impedance spectroscopy (EIS) measurements on ASCs.

4.2.1 La$_{0.58}$Sr$_{0.4}$Co$_{0.2}$Fe$_{0.8}$O$_{3-\delta}$ Cathode

In Fig. 32 the temperature dependent ASR and characteristic time constant values ($R_{chem} \equiv R_{2C}$ and $t_{chem} \equiv t_{2C}$) of the state-of-the-art La$_{0.58}$Sr$_{0.4}$Co$_{0.2}$Fe$_{0.8}$O$_{3-\delta}$ (L58SCF) cathode obtained by the CNLS-fit (using the equivalent circuit developed in chapter 4.1 and depicted in Fig. 26) are shown. Both parameters can be approximated very well with a linear fit over the entire temperature range (571 - 871 ºC), thus demonstrating Arrhenius behaviour. Corresponding activation energies are $E_a(R_{2C})$ = 1.46 eV and $E_a(t_{2C})$ = 1.05 eV.

In the literature activation energy values of ASR_{cat} for LSCF compositions close to the MIEC cathode investigated in this study vary distinctly from 1.2 up to 1.6 eV [48, 49]. Among them the value reported by Esquirol et al. [42] with 1.39±0.09 eV for La$_{0.60}$Sr$_{0.4}$Co$_{0.2}$Fe$_{0.8}$O$_{3-\delta}$ comes closest to the data obtained in this study.
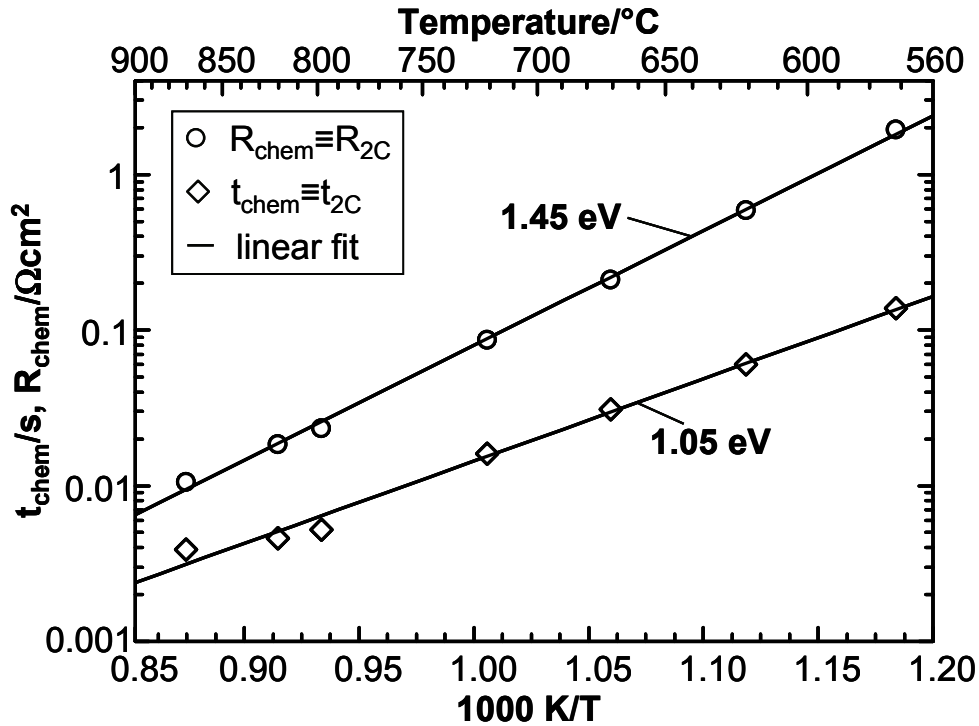
Fig. 32: Temperature dependence of R_{2C} and t_{2C} [pH_2O_{an} = 0.20 atm (balance H$_2$), $pO_{2,cat}$ = 0.21 atm (air)] and corresponding activation energies [cell# Z1_188].

Extraction of D^δ and k^δ

The chemical surface exchange coefficient (k^δ) and chemical diffusion coefficient (D^δ) values can be calculated from Eqs. 2.22 and 2.23 (from chapter 2.5.3) on condition that $R_{chem} \equiv R_{2C}$ and $t_{chem} \equiv t_{2C}$, the electrode parameters ε, a_S, τ_s, c_O, c_{mc} and the thermodynamic enhancement factor γ_{TD} are known. R_{2C} and t_{2C} are available as a function of temperature (see Fig. 32). The parameters ε, a_S and τ_s were estimated for a range of particle sizes and porosities (based on SEM analysis) taking the 3D-Microstructure FEM Model developed at IWE as a basis [23, 50]. The temperature dependent fraction of oxygen vacancies δ, the concentration of oxygen lattice sites c_{mc} and the thermodynamic enhancement factor γ_{TD} are reported in literature [51-54] for a cathode composition (La$_{0.60}$Sr$_{0.4}$Co$_{0.2}$Fe$_{0.8}$O$_{3-\delta}$) similar to L58SCF. The temperature dependency of the thermodynamic enhancement factor γ_{TD} was obtained by fitting the literature data, given for the temperature range from 600 to 900 °C [23, 54], with an exponential function. All essential parameters are summarised in Table 3.

Mean values of ε, ps, a_S, and τ_s were applied (cf. 5th row of Table 3) for the calculation of k^δ and D^δ as a function of temperature. The obtained k^δ and D^δ values are shown in Fig. 33 and listed in Table 4. For comparison between the data obtained on La$_{0.58}$Sr$_{0.4}$Co$_{0.2}$Fe$_{0.8}$O$_{3-\delta}$ within this work and literature, data of k^δ and D^δ recorded on La$_{0.60}$Sr$_{0.4}$Co$_{0.2}$Fe$_{0.8}$O$_{3-\delta}$ [53, 55, 56] are also shown and listed in Table 5. The error bars calculated for k^δ are mainly caused by the

uncertainty of the electrochemical active surface area (a_S) (approx. 87% of the error range), whereas the (rather small) error bars for D^δ are caused by the uncertainty of both porosity ε and tortuosity τ_s. The accuracy of the thermodynamic enhancement factor $\gamma_{TD}(T)$ is quite a considerable additional source of error that was, however, not taken into account as it could not be estimated from [54].

Table 3: Electrode geometry and thermodynamic parameters used to calculate k^δ and D^δ from R_{2c} and t_{2c} using Eqs. 2.22 and 2.23.

	Parameter	$La_{0.58}Sr_{0.4}Co_{0.2}Fe_{0.8}O_{3-\delta}$	Source	Mean Value
Particle size	ps (nm)	200-750	SEM pictures	400
Porosity	ε (%)	30-40	[57]	35
Solid-phase tortuosity	τ_s	1.29-1.47	[23]	1.38
Surface area density	a_S (μm^{-1})	1.63-6.98	[23]	3.32
Ox. Lattice sites	c_{mc} (mol/m^3)	83847-85536	[23]	84713
O^{2-} concentration	c_O (mol/m^3)	82315-84997	[23]	83919
Thermodynamic factor	γ_{TD}	$\gamma_{TD}(T) = 2.17\exp\left(\dfrac{37967}{RT}\right)$	[54]	$\gamma(T)$

In Fig. 33 the values of D^δ evaluated in this study lie over those given in the literature, which vary among themselves up to one order of magnitude. In contrast to these, the values of k^δ match with the literature data, which scatter as well over one order of magnitude. Both k^δ and D^δ evaluated in this study display an Arrhenius type behaviour in a broad temperature range (571°C-871°C) with activation energies E_a = 1.05 eV for k^δ and E_a = 1.26 eV for D^δ. Slightly higher activation energies for D^δ were reported by Bouwmeester et al. [53] with 1.33 eV and by Søgaard et al. [55] with 1.37 eV. The activation energy of k^δ is difficult to compare, because the literature data do not consistently show an Arrhenius behaviour over the entire temperature range. This unsteadiness is obvious for data of Bouwmeester et al. [53] and Ried et al. [56] in Fig. 3, obtained from conductivity relaxation experiments. Here, the separation of surface exchange process and bulk transport process can be a challenge. Several studies [58-61] show, for instance, the difficulty in measuring the surface exchange rate of perovskite MIEC samples thicker than 0.1 mm at high temperature and oxygen partial pressure, where the surface exchange reaction is so fast that transport is completely dominated by the bulk [62]. Another essential precondition for conductivity relaxation experiments is that the gas change time is infinitesimally fast. Therefore, it must be expected that both D^δ and k^δ deduced from conductivity relaxation measurements are smaller than the

true values [63]. This problem is generally aggravated at high temperatures were the surface exchange mechanisms exhibit comparatively short relaxation times and the assumption of an instantaneously gas change of the reactor volume is no more applicable. Therefore, both D^δ and k^δ deduced from conductivity relaxation measurements are expected to be smaller than the true values [63].
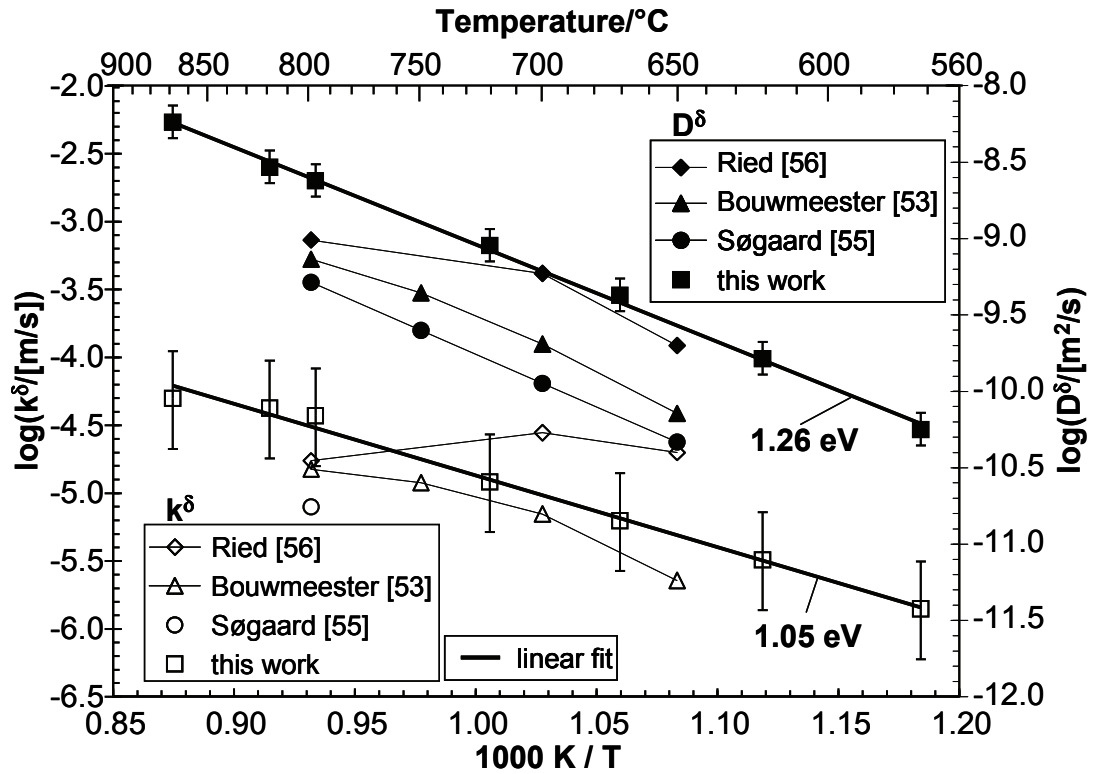
Fig. 33: Arrhenius plots of k^δ and D^δ calculated from R_{2c} and t_{2c} (in air). D^δ: full symbols. k^δ: open symbols [cell# Z1_188].

Table 4: Temperature dependent ASR values (R_{chem}) and characteristic time constant (t_{chem}) of the state-of-the-art LSCF cathode (L58SCF) obtained by the equivalent circuit fit and shown in Fig. 32 together with the calculated k^δ and D^δ (see Fig. 33) (the parameters listed in Table 3 were applied) [$pO_{2,cat}$ = 0.21 atm (air)].

T / °C	R_{chem} / (Ωcm^2)	t_{chem} / (s)	D^δ / (m^2/s)	k^δ / (m/s)
870	0.011	0.0039	$5.77 \cdot 10^{-9}$	$4.97 \cdot 10^{-5}$
820	0.019	0.0046	$2.93 \cdot 10^{-9}$	$4.23 \cdot 10^{-5}$
798	0.023	0.0052	$2.40 \cdot 10^{-9}$	$3.71 \cdot 10^{-5}$
721	0.086	0.0160	$9.00 \cdot 10^{-10}$	$1.21 \cdot 10^{-5}$
671	0.21	0.0310	$4.25 \cdot 10^{-10}$	$6.27 \cdot 10^{-6}$
621	0.599	0.0602	$1.63 \cdot 10^{-10}$	$3.23 \cdot 10^{-6}$
571	1.940	0.1385	$5.62 \cdot 10^{-11}$	$1.40 \cdot 10^{-6}$

Table 5: Temperature dependent k^δ and D^δ values reported in [53], [56] and [55] and shown in Fig. 33. The data were obtained on $La_{0.60}Sr_{0.4}Co_{0.2}Fe_{0.8}O_{3-\delta}$ bulk-samples at $pO_{2,cat}$ = 0.21 atm (air) by conductivity relaxation experiments.

T / °C	Bouwmeester et al. [53]		Ried et al. [56]		Søgaard et al. [55]	
	D^δ / (m^2/s)	k^δ / (m/s)	D^δ / (m^2/s)	k^δ / (m/s)	D^δ / (m^2/s)	k^δ / (m/s)
800	$7.32 \cdot 10^{-10}$	$1.50 \cdot 10^{-5}$	$9.80 \cdot 10^{-10}$	$1.73 \cdot 10^{-5}$	$5.17 \cdot 10^{-10}$	$7.91 \cdot 10^{-6}$
750	$4.40 \cdot 10^{-10}$	$1.20 \cdot 10^{-5}$	____	____	$2.51 \cdot 10^{-10}$	____
700	$2.04 \cdot 10^{-10}$	$7.04 \cdot 10^{-6}$	$5.92 \cdot 10^{-10}$	$2.79 \cdot 10^{-5}$	$1.13 \cdot 10^{-10}$	____
650	$7.18 \cdot 10^{-11}$	$2.28 \cdot 10^{-6}$	$2.00 \cdot 10^{-10}$	$2.00 \cdot 10^{-5}$	$4.65 \cdot 10^{-11}$	____

As shown in this study, the evaluation of D^δ and k^δ for MIEC materials can be expanded to higher (and lower) temperatures by adopting EIS combined with a high resolved DRT and CNLS-fit data analysis. However, several additional parameters related to electrode microstructure and electrochemistry are required to this end.

Uncertainties in k^δ are mainly caused by the variation range of the electrochemical active surface area (a_S). However, recent work on SOFC electrode microstructure modelling, based on high-resolution FIB/SEM data, e.g. by [64-66], strongly suggests that in the near future structural parameters of "real" electrodes will become more readily accessible.

According to Fig. 33, at first sight the uncertainties in D^δ seem to be rather small. Here, the accuracy of the thermodynamic enhancement factor γ_{TD} is an additional source of error. This aspect could not be taken into account in this work, but will increase considerably the uncertainties in D^δ. As can be seen from Eq. 2.22 $D^\delta \propto \gamma_{TD}^2$, even a small error in γ_{TD} will have a significant impact on the accuracy of D^δ.

4.2.2 Alternative Cathode Compositions

Recently a long term study on the state-of-the-art ASC from Forschungszentrum Jülich (FZJ) with a high-performance $La_{0.58}Sr_{0.4}Co_{0.2}Fe_{0.8}O_{3-\delta}$ cathode (L58SCF) showed an increase of the polarisation resistance at 750 °C by 310 % (from 0.015 Ωcm^2 to 0.063 Ωcm^2) within 700 hrs [67]. This result gives evidence for the need of alternative candidate compositions.

Therefore, in this subchapter two cathodes, $La_{0.68}Sr_{0.3}FeO_{3-\delta}$ (LSF) and $La_{0.68}Sr_{0.3}Co_{0.2}Fe_{0.8}O_{3-\delta}$ (L68SCF: La-rich), which are characterised by electrochemical impedance spectroscopy (EIS) over a wide range of operating conditions, will be introduced. Both material systems are assessed with regard to surface exchange kinetics and oxygen ion bulk diffusion properties.

Electrode Kinetics

<u>Temperature Dependency</u>

The SOFC single cells were tested at temperatures between 630 and 870 ºC with a fuel gas composition of 62.5 % H_2O and 37.5 % H_2. Air was used as cathode gas. The DRTs of the analysed cells at three different temperatures (726, 766, 807 °C) are compared in Fig. 34. As the anode substrate properties were kept constant, the anodic processes P_{1A} (gas-phase diffusion in the pores of the Ni/YSZ-anode-substrate) and $P_{2A}+P_{3A}$ (anode electrochemistry losses) of both samples differ insignificantly (but still distinguishable). In contrast to them, process P_{2C} (loss resulting from oxygen incorporation and oxygen ion transport within the cathode) strongly depends on the cathode composition. The L68SCF cell is characterised by an extensive P_{2C} peak area when compared with the LSF cathode. This observation is in accordance with the area specific resistance (ASR) values obtained by the equivalent circuit fit and shown in Fig. 35. The corresponding values are also listed in Table 6. The ASR of the L68SCF cathode ($R_{2C,L68SCF}$) is by a factor of 2 to 3 higher over the entire temperature range.
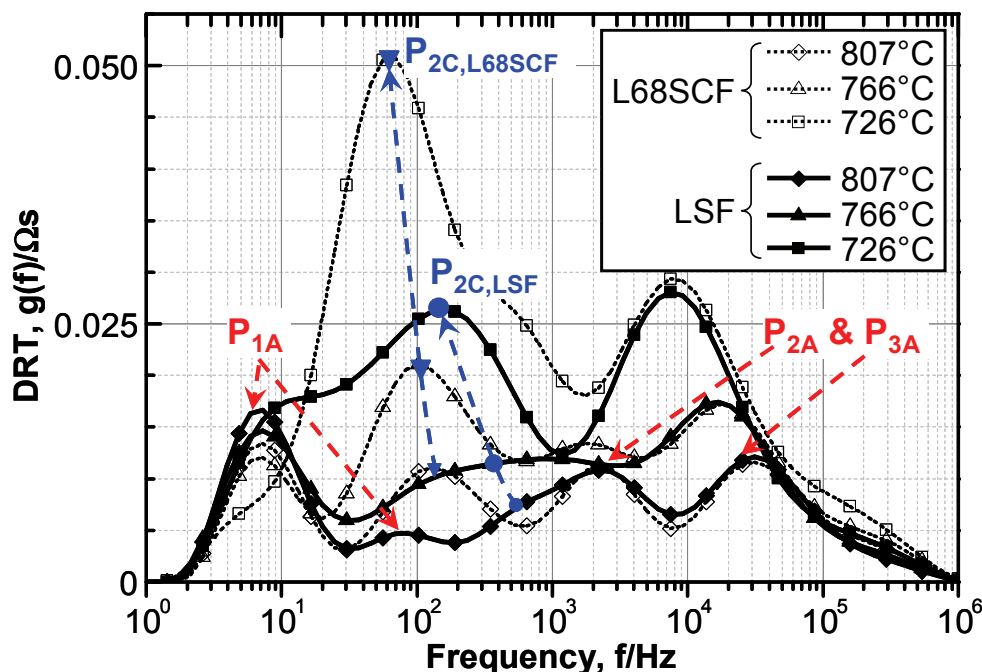
Fig. 34: Series of DRT-curves at three different temperatures. [pH_2O_{an} = 0.625 atm (balance H$_2$), $pO_{2,cat}$ = 0.21 atm (air)] (L68SCF was cell# Z1_158; LSF was cell# Z1_160).

The ASRs $R_{2C,L68SCF}$ and $R_{2C,LSF}$ can be approximated very well with a linear fit, demonstrating a good Arrhenius behaviour. From the slope of the fitted lines the activation energies $E_{a,2C,L68SCF}$ = 1.69 eV and $E_{a,2C,LSF}$ = 1.80 eV are obtained. As already mentioned, in the literature activation energy values reported for LSCF cathodes vary very strongly from 1.2 up to 1.6 eV [48, 49]. Among them the nearest value to $E_{a,2C,L68SCF}$ is reported by Lane et al [49]. with 1.6 eV for La$_{0.60}$Sr$_{0.4}$Co$_{0.2}$Fe$_{0.8}$O$_{3-\delta}$. Unfortunately, less activation energy data are available for LSF in literature; however, Baumann [68] reports a value of 1.8 eV for La$_{0.6}$Sr$_{0.4}$FeO$_{3-\delta}$, measured on microelectrodes, which is identical to the value obtained in this study.

By comparing these ASR values with the ASR of the L58SCF cathode ($R_{2C,L58SFC}$) at 750 °C, before and after degradation (cf. Fig. 35), one can notice that the LSF cathode could represent a potential alternative to the state-of-the-art cathode composition (La$_{0.58}$Sr$_{0.4}$Co$_{0.2}$Fe$_{0.8}$O$_{3-\delta}$). However a justification needs long term experiments. Nevertheless, during measurements conducted so far no extraordinary degradation effects of LSF could be identified, but only after appropriately designed long term experiments a conclusive statement can be given.
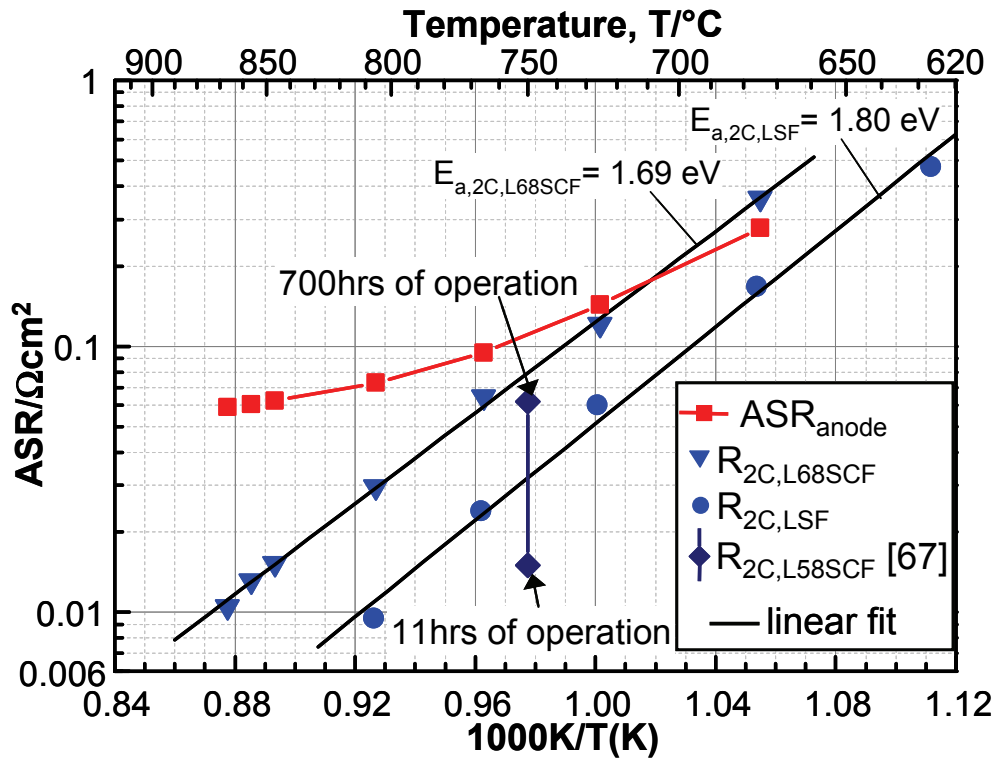
Fig. 35: Characteristic dependence of ASRs on operating temperature. [pH_2O_{an} = 0.625 atm (balance H_2), $pO_{2,cat}$ = 0.21 atm (air)] (L68SCF was cell# Z1_158; LSF was cell# Z1_160).

Table 6: ASR values of the LSF ($R_{2C,LSF}$) and L68SCF ($R_{2C,L68SCF}$) cathode together with the overall anode ASR ($ASR_{anode}=R_{1A}+R_{2A}+R_{3A}$) vs. temperature obtained by the equivalent circuit fit and shown in Fig. 35 [pH_2O_{an} = 0.625 atm (balance H_2), $pO_{2,cat}$ = 0.21 atm (air)].

T / °C	$R_{2C,LSF}$ / (Ωcm^2)	$R_{2C,L68SCF}$ / (Ωcm^2)	ASR_{anode} / (Ωcm^2)
866	____	0.011	0.059
807	0.0095	0.030	0.073
766	0.024	0.065	0.094
726	0.060	0.121	0.144
676	0.168	0.360	0.279
626	0.474	____	____

In Fig. 35 also the temperature dependent overall anode polarisation resistance (ASR_{anode} = $R_{1A}+R_{2A}+R_{3A}$) is plotted. As can be seen the temperature dependency of ASR_{anode} is characterised by an Arrhenius behaviour at lower temperatures (<775 °C), whereas at higher temperatures an apparent decrease of the activation energy is observed (decreasing slope of the curve). This is explained by the fact that with increasing temperature

the overall anode polarisation loss becomes more and more dominated by the almost temperature independent gas diffusion polarisation loss (R_{1A}) within the anode substrate.

In summary, it can be noted that ASR_{anode} represents a major part of the overall polarisation resistance of state-of-the-art ASCs, at least for operating temperatures above 725 °C. This result underlines once again that, besides cathode research, more emphasis should be placed on anode development in ongoing SOFC research activities.

In Fig. 36 the characteristic time constant t_{chem} = t_{2C} obtained from the equivalent circuit fit is shown as a function of temperature. Both, $t_{2C,LSF}$ and $t_{2C,L68SCF}$ show an Arrhenius type behaviour with activation energies of 1.30 and 0.59 eV respectively.
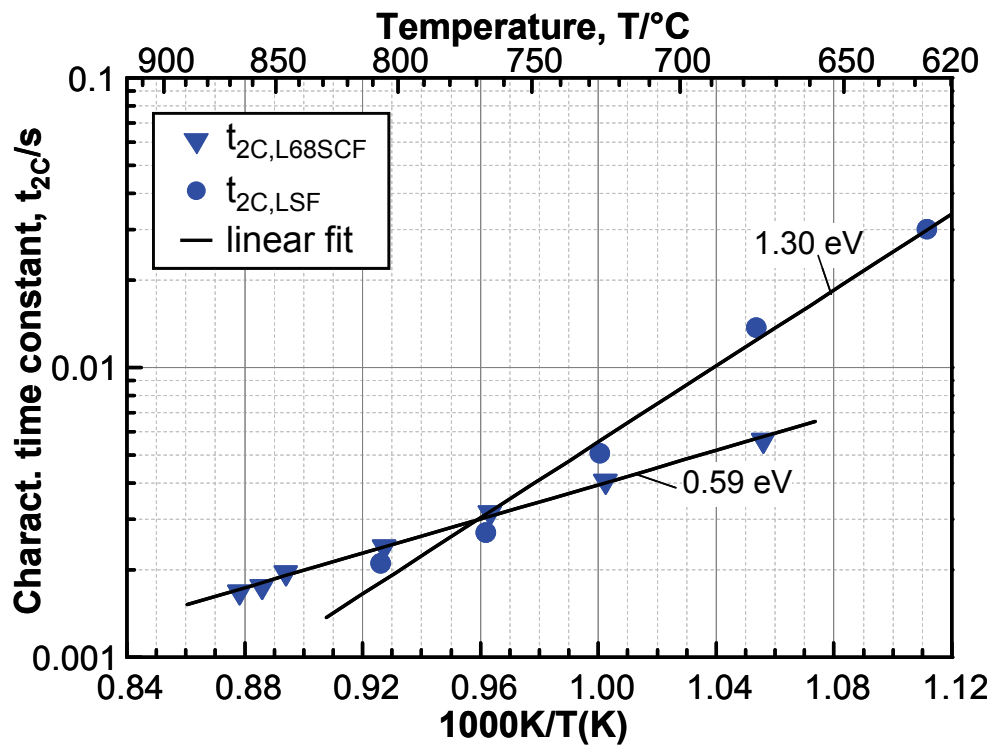
Fig. 36: Characteristic dependence of t_{2C} on operating temperature. [pH_2O_{an} = 0.625 atm (balance H$_2$), $pO_{2,cat}$ = 0.21 atm (air)] (L68SCF was cell# Z1_158; LSF was cell# Z1_160).

Cathodic Oxygen Partial Pressure Dependency

The oxygen content of the gas mixture supplied to the cathode was varied between 21 % (air) and 1 % (balance nitrogen), whereas the composition of the fuel gas was kept constant at a ratio 62.5 % H$_2$O to 37.5 % H$_2$. The high water content was used to reduce the anodic polarisation losses to a minimum thereby making the deconvolution of the cathodic contributions simpler.

The polarisation resistances R_{1C}, R_{2C} and the characteristic time constants t_{2C} obtained by the CNLS fit (using the equivalent circuit presented in chapter 4.1 and depicted in Fig. 26)

are plotted over the partial pressure of oxygen in Fig. 37a and Fig. 37b, respectively. Both parameters show an almost linear trend in the double logarithmic plane and can be described using the expressions $R_{2C} = b \cdot pO_2^n$ and $t_{2C} = c \cdot pO_2^m$. Table 7 shows values of the best fit to the expressions described before.

The area specific resistance R_{1C} related to the gas diffusion loss inside the pores of the cathode structure shows, as expected, a strong dependency on pO_2, whereas no mentionable difference is observed when comparing the values of both analysed cathode compositions. The latter proves the similar microstructural properties of the LSF and L68SCF cathodes, with respect to their porosity, tortuosity and mean pore radius.
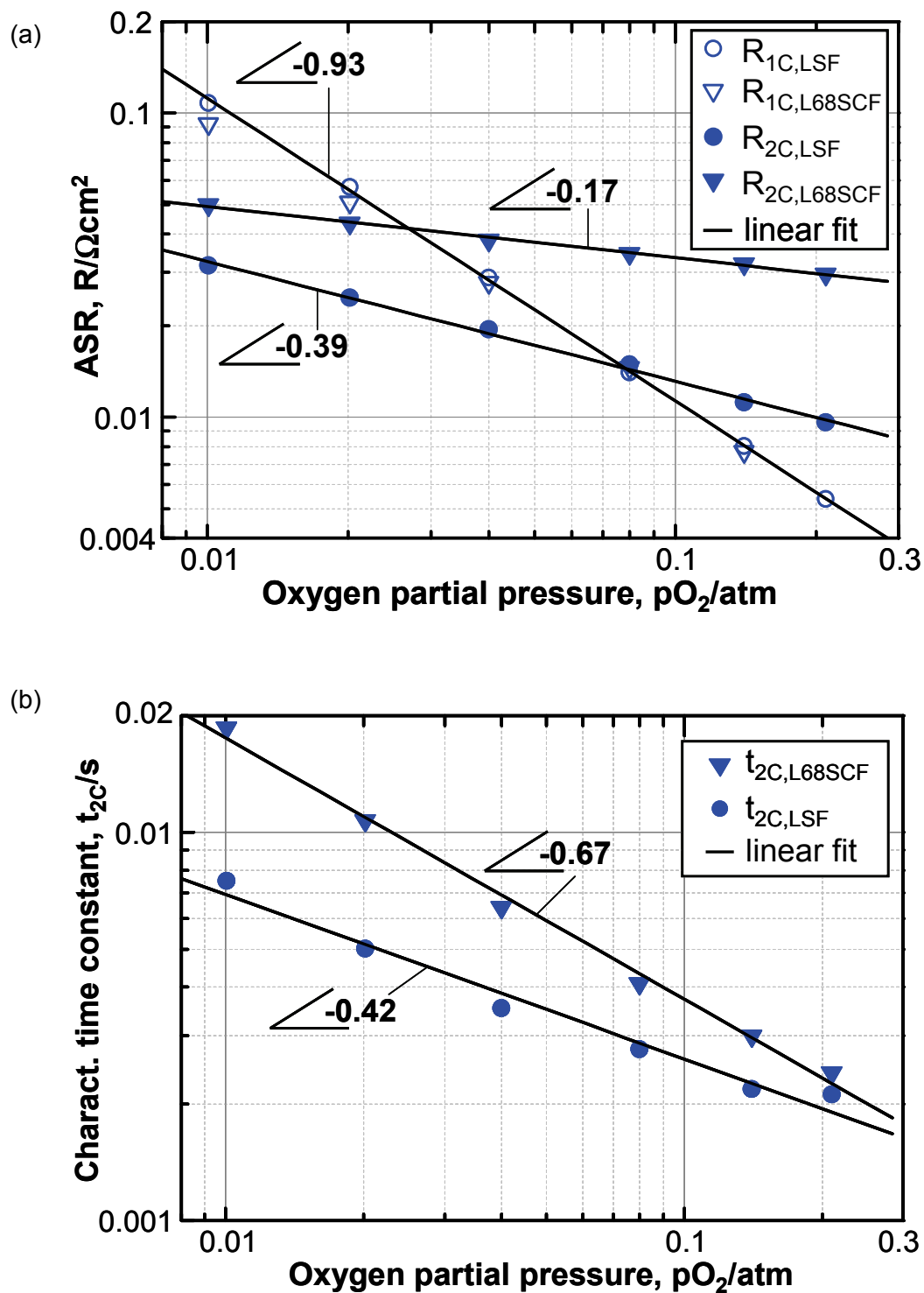
Fig. 37: (a) R_{2C} and (b) t_{2C} as a function of oxygen partial pressure at 805 °C (L68SCF was cell# Z1_158; LSF was cell# Z1_160).

Table 7: Best Fit values of R_{2C} and t_{2c} to the expressions $R_{2C} = b \times pO_2^n$ and $t_{2c} = c \times pO_2^m$.

Cathode	b / ($\Omega cm^2/atm^n$)	n	c / (s/atm^m)	m
L68SCF	2.26×10^{-2}	-0.17	7.90×10^{-4}	-0.67
LSF	5.29×10^{-3}	-0.39	9.84×10^{-4}	-0.42

Extraction of D^δ and k^δ

Using Eqs. 2.22 and 2.23 (from chapter 2.5.3), the chemical surface exchange coefficient (k^δ) and chemical diffusion coefficient (D^δ) values were calculated as a function of temperature and pO_2 based on the values R_{2C} and t_{2C} reported in Fig. 35-37, before. The electrode geometry parameters ε, a_S and τ_s were estimated for a reasonable range of particle sizes (ps) and porosities (based on SEM analysis) by the 3D-Microstructure FEM Model developed at IWE [23, 50].

Due to the fact, that for the analysed cathode materials no experimental values for the fraction of oxygen vacancies (δ), the concentration of oxygen lattice sites (c_{mc}) and the thermodynamic enhancement factor (γ_{TD}) were available, the probable value (range) of these parameters was estimated from literature data, obtained on similar cathode compositions. The obtained values are listed in Table 8. Based on this value range a set of mean values was defined (cf. 4th row of Table 8), which was used to calculate the D^δ and k^δ values from R_{2C} and t_{2C}, thereby making the simplifying assumption of temperature and oxygen partial pressure independent γ_{TD}, δ and c_{mc} values.

Table 8: Electrode geometry and thermodynamic parameters used to calculate D^δ and k^δ from R_{2C} and t_{2C}.

Parameter	LSF	L68SCF	Mean Value
ps (nm)	200-750 (SEM analysis)	200-750 (SEM analysis)	400
ε (%)	30-40	30-40	35
τ_s	1.29-1.47	1.29-1.47	1.38
a_S (μm^{-1})	1.63-6.98	1.63-6.98	3.32
c_{mc}	83288 [69]	84262 [51]	83288 and 84262
$3-\delta$	2.8-2.98 [70]	2.8-2.98 [53]	2.9
$\log(\gamma_{TD})$	1.5-2.5 [71]	1.5-2.5 [53]	2

Temperature Dependency

Fig. 38a and Fig. 38b show the calculated values of the chemical surface exchange coefficient k^δ and chemical diffusion coefficient D^δ as a function of temperature. The obtained values are also listed in the following Table 9. The error bars refer to the upper and lower values of D^δ and k^δ with respect to the parameter value limits listed in Table 8. For comparison, literature data of k^δ and D^δ recorded on $La_{0.60}Sr_{0.4}Co_{0.2}Fe_{0.8}O_{3-\delta}$ (L60SCF) [53, 55, 56] (see Table 5 before)] and $La_{1-x}Sr_xFeO_{3-\delta}$ [71], (see Table 10)] are also shown. In Fig. 38a and 38b the data of Endler et al. [67] obtained on L58SCF at 750°C before and after long term measurements are included.

Both coefficients (k^δ and D^δ) of the two alternative cathodes analysed within this study show an Arrhenius behaviour and thus can be approximated very well with a straight line. The exchange coefficients of both cathodes show noticeable difference in activation energies whereas a less pronounced difference of the slope is observed for the diffusion coefficients. The activation energies of k^δ and D^δ obtained from the fit are 1.30 eV and 2.46 eV for LSF, and 0.59 eV and 2.97 eV for L68SCF, respectively. When comparing these values with literature data recorded on similar cathode compositions one can notice that the activation energies of D^δ obtained in this study are extremely higher. For L60SCF activation energies of D^δ between 1.3 and 1.5 eV are reported. Whereas ten Elshof et al [71] measured values of 0.64 eV and 1.09 eV on $La_{0.9}Sr_{0.2}FeO_{3-\delta}$ and $La_{0.6}Sr_{0.4}FeO_{3-\delta}$ respectively. Søgaard et al. [24] obtained a value of 1.42 eV for D^δ on $La_{0.6}Sr_{0.4}FeO_{3-\delta}$.

The discussed strong discrepancy in activation energies of D^δ may be explained by the different experimental conditions. All literature data referred to above were obtained by electrical conductivity relaxation experiments on dense bulk samples (porosity < 5%). In contrast to them the data presented here are obtained directly from impedance data measured on full ASC cells; thus, the cathode material in this study was in direct contact, during sintering and operation, with the GDC buffer layer. Therefore, in this case, a chemical reaction between both layers (GDC and cathode material), causing a change of the chemical properties of the cathodes, cannot be excluded. For instance, Uhlenbruck et al. [72] recently analysed ASC cells with electron-beam physical vapour deposition (EB-PVD) GDC and LSCF cathode by transmission electron microscopy (TEM) measurements. Besides a Sr-depletion they found a slight Gd-enrichment in the sintered LSCF cathode, which they found to be detrimental to the power density of the cell.
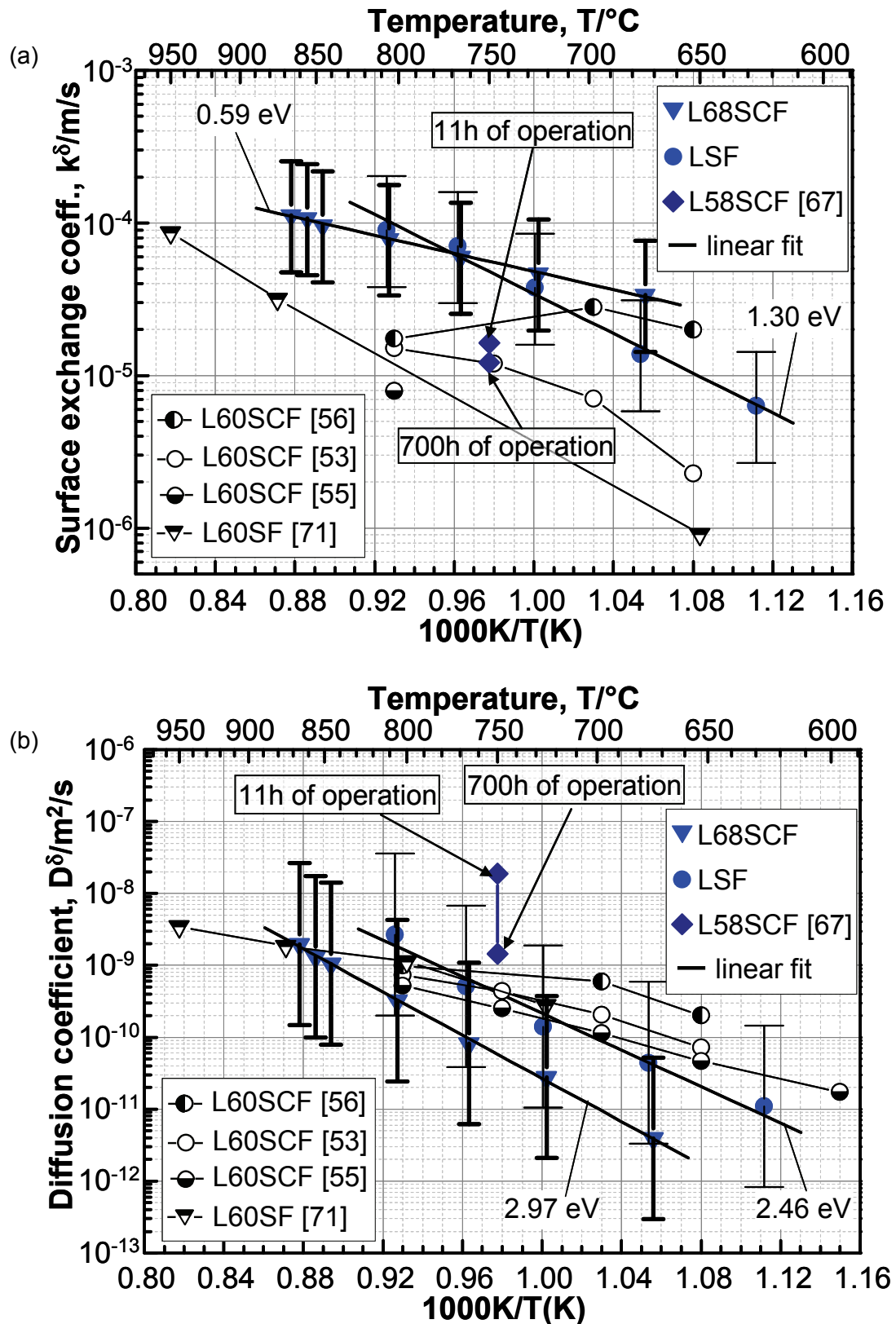
Fig. 38: (a) Arrhenius plots of chemical surface exchange coefficient k^δ and (b) chemical diffusion coefficient D^δ calculated from R_{2c} and t_{2c} (in air). Error bars (L68SCF: thick line. LSF: thin line) originate from uncertainty of parameters needed for calculation of k^δ and D^δ (see Table 8) (L68SCF was cell# Z1_158; LSF was cell# Z1_160).

Table 9: Temperature dependent k^δ and D^δ values for LSF and L68SCF obtained from R_{2C} and t_{2C}, respectively. The parameters listed in Table 8 were applied for the calculation. [$pO_{2,cat}$ = 0.21 atm (air)].

T / °C	LSF (this work)		L68SCF (this work)	
	D^δ / (m²/s)	k^δ / (m/s)	D^δ / (m²/s)	k^δ / (m/s)
866	____	____	$1.98 \cdot 10^{-9}$	$1.12 \cdot 10^{-4}$
807	$2.67 \cdot 10^{-9}$	$8.98 \cdot 10^{-5}$	$3.21 \cdot 10^{-10}$	$7.87 \cdot 10^{-5}$
766	$5.05 \cdot 10^{-10}$	$7.05 \cdot 10^{-5}$	$8.15 \cdot 10^{-11}$	$6.00 \cdot 10^{-5}$
726	$1.40 \cdot 10^{-10}$	$3.75 \cdot 10^{-5}$	$2.78 \cdot 10^{-11}$	$4.68 \cdot 10^{-5}$
676	$4.41 \cdot 10^{-11}$	$1.38 \cdot 10^{-5}$	$3.90 \cdot 10^{-12}$	$3.37 \cdot 10^{-5}$
626	$1.09 \cdot 10^{-11}$	$6.31 \cdot 10^{-6}$	____	____

Table 10: Temperature dependent k^δ and D^δ values for $La_{0.6}Sr_{0.4}FeO_{3-\delta}$ (L60SF) reported by ten Elshof et al. [71] (see Fig. 38). The data were obtained on bulk-samples at $pO_{2,cat}$ = 0.21 atm (air) by conductivity relaxation experiments.

T / °C	L60SF (ten Elshof et al. [71])	
	D^δ / (m²/s)	k^δ / (m/s)
950	$3.47 \cdot 10^{-9}$	$8.70 \cdot 10^{-5}$
875	$1.86 \cdot 10^{-9}$	$3.18 \cdot 10^{-5}$
800	$1.12 \cdot 10^{-9}$	____
725	$2.75 \cdot 10^{-10}$	____
650	____	$9.09 \cdot 10^{-7}$

Comparing the obtained activation energies of the surface exchange coefficients k^δ with literature data, similar values for the LSF cathode are found: ten Elshof et al. [71] obtained activation energies of 1.17 and 1.36 eV for $La_{0.9}Sr_{0.4}FeO_{3-\delta}$ and $La_{0.6}Sr_{0.4}FeO_{3-\delta}$ respectively. On the other side it appears more difficult to compare the activation energy of the k^δ value obtained on L68SCF with literature data on $La_{0.60}Sr_{0.4}Co_{0.2}Fe_{0.8}O_{3-\delta}$. As already explained in chapter 4.2.1 before, this is due to the fact, that the reported literature data very often do not show an Arrhenius behaviour over the entire temperature range (cf. data of Bouwmeester [53] and Ried [56] in Fig. 38a).

Nevertheless, in summary it should be noted that the relatively high activation energies of the cathode polarisation resistance $R_{2C,}$ determined for LSF (1.8 eV) and L68SCF (1.69 eV), are not ascribable to the temperature dependency of the surface exchange kinetics but are caused by the extraordinary high activation energies of the oxygen ion bulk diffusion process (> 2.46 eV).

Cathodic Oxygen Partial Pressure Dependency

In Fig. 39 the calculated values of D^δ and k^δ are shown vs. oxygen partial pressure at 805 °C. The values of k^δ are proportional to pO_2^ξ with $\xi = 0.42$ for the LSF cathode, and $\xi = 0.67$ for the L68SCF cathode respectively.

When comparing the D^δ values an opposite trend between the two cathodes is seen. With increasing pO_2 the chemical diffusion coefficient of LSF is increasing, whereas a slight decrease is seen for L68SCF.

At this point it is important to underline again that in contrast to k^δ, which is independent on the thermodynamic enhancement factor (γ_{TD}), D^δ is proportional to the square of γ_{TD} (cf. Eqs. 2.22 and 2.23). Therefore, in order to make a conclusive statement about the correct dependency of D^δ on pO_2, the oxygen partial pressure dependent γ_{TD} values need to be known. It should be also noted that the error bars shown for the k^δ values are almost solely (87 % of the error range) caused by the uncertainty of the electrochemical active surface area (a_S). On the other side the error bars of the D^δ values are almost solely caused by the uncertainty of the thermodynamic enhancement factor (γ_{TD}) (89 % of the error range) due to the fact that D^δ is independent on the electrochemical active surface area (a_S). This can be understood very easily by replacing k^δ from Eq. 2.22 with the k^δ obtained from Eq. 2.23 and cutting out in this way the parameter a_S in the denominator of Eq. 2.22.
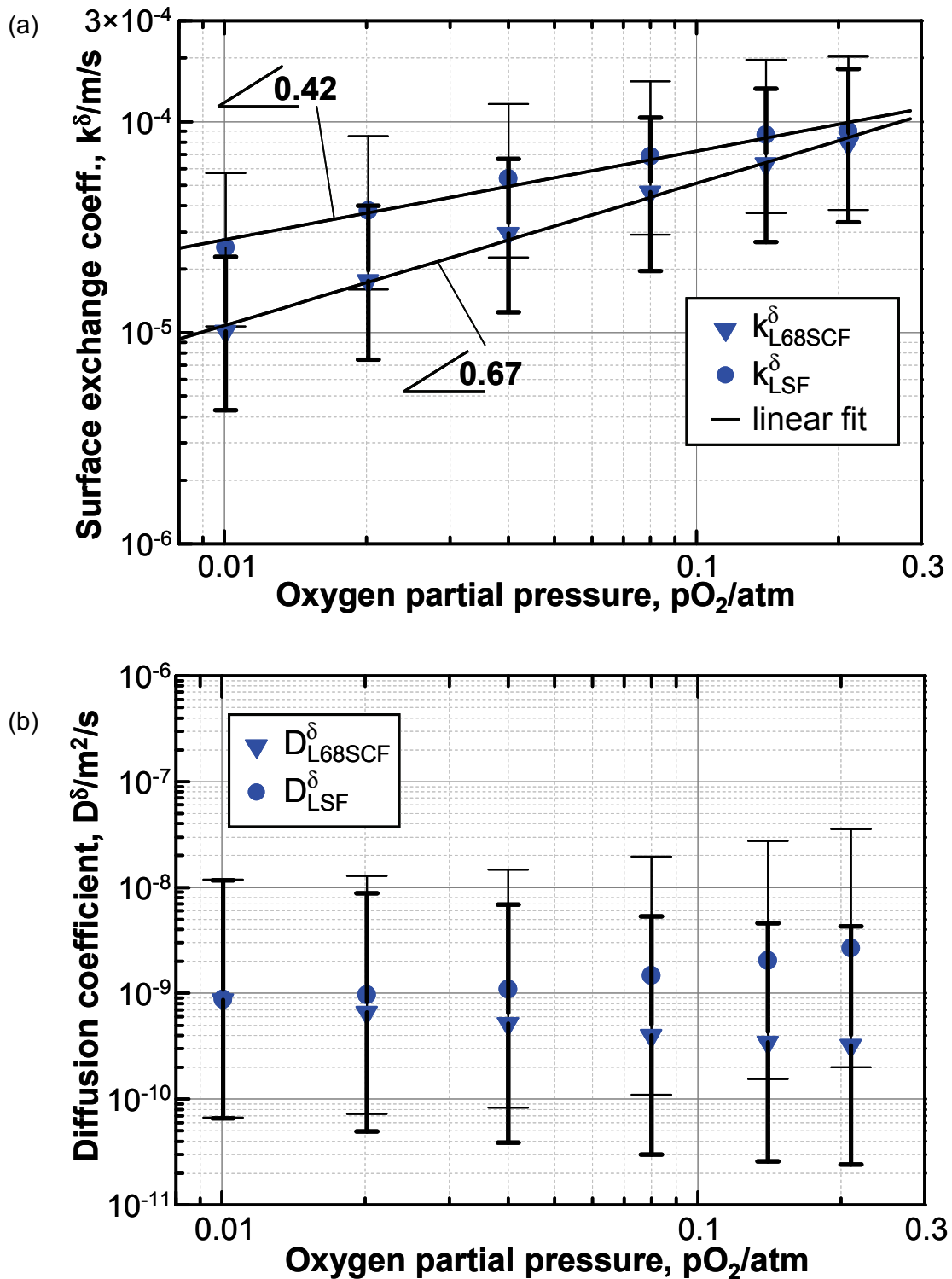
Fig. 39: (a) Surface exchange coefficient k^δ and (b) chemical diffusion coefficient D^δ vs. oxygen partial pressure at 805 °C. Error bars (L68SCF: thick line. LSF: thin line) originate from uncertainty of parameters needed for calculation of k^δ and D^δ (see Table 8) (L68SCF was cell# Z1_158; LSF was cell# Z1_160).

Brief Summary

Chemical surface and diffusion coefficients (k^δ and D^δ) of "real" MIEC cathode structures (as deposited on ASC) were obtained from impedance measurements on anode supported cells. As a prerequisite, the Gerischer-type impedance of the cathode has to be extracted, and several additional parameters related to electrode microstructure and electrochemistry are required to this end.

The evaluation of k^δ and D^δ for MIEC materials was expanded to higher (and lower) temperatures compared to well-established methods (i.e. conductivity relaxation).

Given the recent advancements in obtaining structural parameters from electrode reconstruction based on FIB/SEM data and appropriate microstructure modelling [64-66], this approach also holds potential for an assessment of degradation phenomena correlated to microstructural changes and/or compositional changes of "real" cathodes.

4.3 Modelling of the Current-Voltage Characteristic

From literature, several electrochemical models [73-80] that predict the I-U behaviour of an anode-supported SOFC single cell are known. However, these models encounter difficulties in the prediction of polarisation losses caused by activation and gas diffusion, particularly over a sufficiently broad range of operating conditions. Although these models as well as other models [75, 77] are based on physical equations such as the Butler-Volmer equation for determining the activation polarisation or Fick's model for determining diffusion polarisation, these equations often have to be simplified to a much too large extent. The Butler-Volmer equation, as described by Noren et al. [78] or Jiang et al. [79], is substituted by a linear function and the Tafel equation. The partial pressure dependencies of the exchange current densities are largely simplified [75, 76, 81] or only a constant value is used for the exchange current density [74, 79] because the parameters that determine the partial pressure dependencies cannot be determined at all, or, at least, not independently of each other. Owing to these limitations, frequently [82-84] parameters are used that are either generally estimated or taken from literature.

In the following a zero-dimensional stationary model for the current-voltage (I-U) characteristics of anode-supported solid oxide fuel cells (SOFC) is presented. Similar to the modelling approaches cited above the procedure includes modelling of the activation polarisation by the Butler-Volmer equation and the calculation of the gas diffusion polarisation from Fick's law. However, in the present work the different kinds of electrode polarisation resistances shall be separated from experimental impedance data by means of the detailed equivalent circuit model developed in this study (see Fig. 26 in chapter 4.1.2). This has the one big advantage that partial pressure and temperature dependency of electrode exchange current densities can be determined by a fit of semi-empirical power law model equations. For the first time, the exponents a and b for the H_2 and H_2O partial pressure dependency of the anodic exchange current density are obtained independently. Equally, the exponent m for the O_2 partial pressure dependency of the cathodic exchange current density is derived. In contrast to alternative modelling approaches, the anodic and cathodic gas diffusion polarisation is calculated without the estimation of parameters such as tortuosity and porosity. This approach proves to be of advantage to separate anodic and cathodic activation and diffusion polarisation and precisely predicts I-U characteristics for a wide operating range.

4.3.1 Model Description and Parameter Identification

Various models [73-77, 79, 80] still disclose weak points with respect to the prediction of activation and diffusion polarisation losses, because the ansätze used were largely simplified or the modelling parameters could not be determined independently of each other. In this

work, the current–voltage characteristics shall be modelled based on generally valid assumptions, such as the Butler-Volmer equation, Fick's law and Ohm's law, yet without any further simplifications. The model has been implemented in *Matlab®*, thereby taking into consideration the following issues:

- the use of generally valid ansätze, derived from physically well-founded equations or experimentally validated empirical equations (power law ansatz).

- all modelling parameters shall be determined from open-circuit impedance measurements (with the exception of the charge transfer coefficients α_{an} and α_{cat} that are determined from impedance measurements under load).

- all processes responsible for polarisation resistance have to be considered in the model.

In the following subsections, the modelling equations, the necessary modelling parameters as well as the means of determining them are presented.

Operating Voltage

The open-circuit voltage U_{OCV} is described by the Nernst equation (Eq. 2.7), which, for completeness, is shown again (Eq. 4.3) below:

$$U_{OCV}(T) = U_0(T) - \frac{RT}{2F} \ln\left(\frac{pH_2O_{an}}{pH_{2,an} \cdot \sqrt{pO_{2,cat}}} \right) \qquad \text{Eq. 4.3}$$

In Eq. 4.3 $pO_{2,cat}$ denotes the oxygen partial pressure at the cathode, $pH_{2,an}$ the hydrogen partial pressure at the anode, pH_2O_{an} the water partial pressure at the anode, and T the absolute temperature in Kelvin. The theoretical standard cell voltage $U_0(T)$ can be determined from the Gibbs free reaction enthalpy $\Delta G_0(T)$ [kJ/mol] of the overall reaction (see Eq. 2.7). As discussed in chapter 2.3 before, under load U_{OCV} is reduced by internal losses, such as activation, diffusion and ohmic losses. The operating voltage of the cell U_{cell} can be calculated by Eq. 4.4 on the basis of Kirchhoff's second law (mesh rule).

$$U_{cell} = U_{OCV} - \left(\eta_{ohm} + \eta_{act,an} + \eta_{act,cat} + \eta_{conc,an} + \eta_{conc,cat} \right) \qquad \text{Eq. 4.4}$$

η_{ohm} denotes the overpotential owing to ohmic losses in the cell, $\eta_{act,an}$, $\eta_{act,cat}$, $\eta_{conc,an}$, and $\eta_{conc,cat}$ denote the activation and concentration overpotentials at the anode and cathode, respectively.

Ohmic Losses

Ohmic losses occur during the electronic or ionic transport through the electrodes and the electrolyte. The overall ohmic losses are the sum of each individual ohmic contribution. According to Ohm's law, the ohmic overpotential linearly increases with the current density j.

$$\eta_{ohm} = j \cdot \sum_k R_k = j \cdot R_{ohm}$$

Eq. 4.5

R_k is the area-specific resistance of anode, cathode, GDC interlayer, electrolyte and the GDC/8YSZ interdiffusion layer, respectively. As the model should be applicable over a wide temperature range, the temperature dependence of $R_{ohm}(T)$ must be precisely predictable. For thermally activated charge transport mechanisms, such as the oxygen ion conduction in 8YSZ, in general the following relationship, derived from the Arrhenius equation, holds [4, 80].

$$R_{ohm}(T) = \frac{T}{B_{ohm}} \exp\left(\frac{E_{act,ohm}}{RT}\right)$$

Eq. 4.6

T denotes the absolute temperature in Kelvin, $E_{act,ohm}$ the activation energy in kJ/mol, and B_{ohm} is a material-specific constant in [S·K/m^2]. The unknown parameters B_{ohm} and $E_{act,ohm}$ are the first two to be determined in this subchapter. To this end, open-circuit impedance measurements carried out in the temperature range 571...871 °C were evaluated using the equivalent circuit developed in this work (see Fig. 26 in chapter 4.1.2). In Fig. 40, the ohmic resistance R_{ohm} (equivalent circuit element R_0) obtained from the CNLS fit is shown as a function of temperature, as well as the curve resulting from fitting Eq. 4.6 to the measurement data. The temperature dependence of the ohmic resistance R_{ohm} follows Eq. 4.6 very well. Thus, the values B_{ohm} = 4.1879×10^{12} S·K/m^2 and $E_{act,ohm}$ = 90.31 kJ/mol (0.94 eV) can be extracted (also see Table 12). The latter value lies within the range known from literature [44, 86, 87] for the activation energies of 8YSZ ($E_{act,8YSZ}$ = 87.0 - 99.0 kJ/mol). $E_{act,ohm}$ also contains the ohmic losses for both the GDC interlayer (with a smaller activation energy of $E_{act,GDC}$ = 77.2 kJ/mol [88]) and the interdiffusion layer between GDC and 8YSZ (which has a higher activation energy of up to 111 kJ/mol [88]).
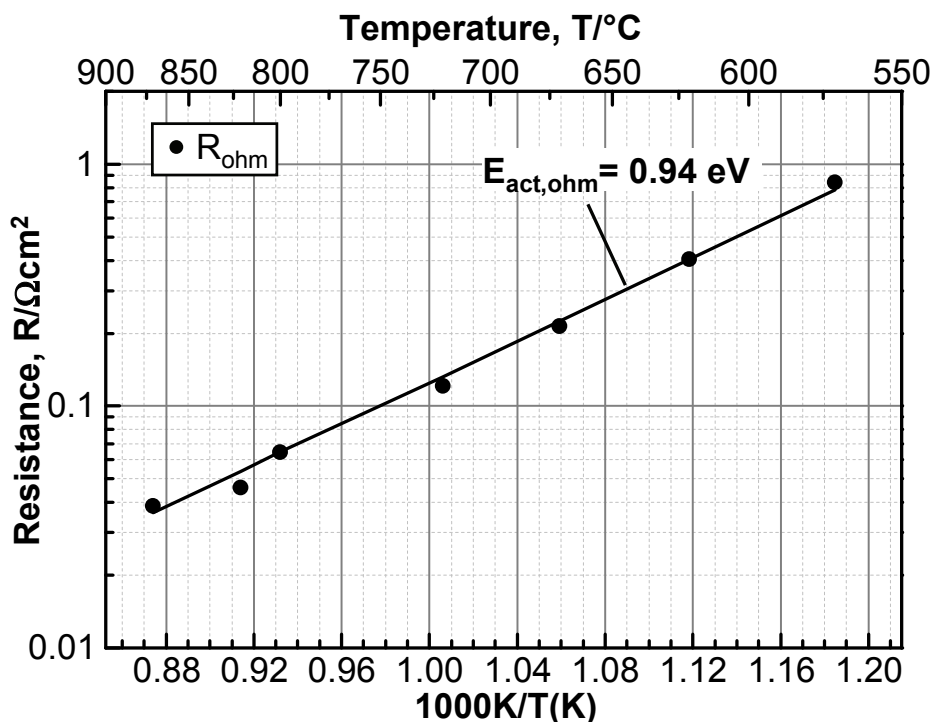
Fig. 40: Ohmic resistance R_{ohm} [Ω·cm²] as a function of temperature (T = 871, 821, 798, 721, 671, 621, 571 °C) [cell# Z1_188].

Diffusion Overpotential

High current densities are correlated with an enhanced gas transport and gas conversion in the electrode, which leads to polarisation losses. The so-called diffusion polarisation at the anode results from an undersupply of the three-phase points with fuel. Simultaneously the reaction product (water) is being transported away from the reaction zone too slowly. At the cathode, losses due to diffusion polarisation occur, too. They are caused by an undersupply with oxidizing gas. According to the results discussed in chapter 4.1, this process is only unambiguously identifiable in the DRT at very low oxygen partial pressures ($pO_{2,cat}$ < 0.05 atm)). This may be the reason why other models [89] neglect the diffusion polarisation at the cathode. However, in the present study the partial pressure and temperature dependence of this process shall be considered.

Calculation of the diffusion polarisation overpotential is based on the Nernst equation (Eq. 2.4), from which the following Eqs. 4.7 and 4.8 can easily be derived [14].

$$\eta_{conc,an} = \frac{RT}{2F} \ln\left(\frac{pH_2O_{an}^{TPB} \cdot pH_{2,an}}{pH_2O_{an} \cdot pH_{2,an}^{TPB}} \right)$$

Eq. 4.7

$$\eta_{conc,cat} = \frac{RT}{4F} \ln\left(\frac{pO_{2,cat}}{pO_{2,cat}^{TPB}}\right) \qquad \text{Eq. 4.8}$$

$\eta_{conc,el}$ (the subscript „el" refers to anode („an") and cathode („cat"), respectively) describes the overpotential resulting from a partial pressure difference between gas atmosphere and TPB. $pH_{2,an}$, pH_2O_{an}, and $pO_{2,cat}$ are the known partial pressures of hydrogen, water and oxygen, respectively, in the gas channel.

In [15] the unknown partial pressures $pH_{2,an}^{TPB}$, $pH_2O_{an}^{TPB}$, and $pO_{2,cat}^{TPB}$ are determined by applying Fick's first law and assuming a linear concentration gradient as a function of the current density j:

$$pH_{2,an}^{TPB} = pH_{2,an} - \frac{RTL_{an}}{2FD_{H_2}^{eff}} j \cdot \left(1.0133 \cdot 10^5 \frac{Pa}{atm}\right)^{-1} \qquad \text{Eq. 4.9}$$

$$pH_2O_{an}^{TPB} = pH_2O_{an} + \frac{RTL_{an}}{2FD_{H_2O}^{eff}P_0} j \qquad \text{Eq. 4.10}$$

and

$$pO_{2,cat}^{TPB} = pO_{2,cat} - \left(\frac{P - pO_{2,cat}}{P}\right)\frac{RTL_{cat}}{4FD_{O_2}^{eff}P_0} j \qquad \text{Eq. 4.11}$$

P denotes the absolute atmospheric pressure ($P = 1$ atm) and $P_0 = 101330$ Pa/atm represents a conversion factor from [atm] to [Pa]. By inserting Eqs. 4.9, 4.10 and 4.11 into Eqs. 4.7 and 4.8, [15] obtains Eqs. 4.12 and 4.13, which relate the diffusion-based voltage drop $\eta_{conc,el}$ to the current density j:

$$\eta_{conc,an} = \frac{RT}{2F} \ln\left(\frac{1 + \dfrac{RTL_{an}}{2FD_{H_2O}^{eff}pH_2O_{an}P_0} \cdot j}{1 - \dfrac{RTL_{an}}{2FD_{H_2}^{eff}pH_{2,an}P_0} \cdot j}\right) \qquad \text{Eq. 4.12}$$

$$\eta_{conc,cat} = \frac{RT}{4F} \ln\left(1 \Big/ \left(1 - \frac{RTL_{cat}(1 - pO_{2,cat}/P)}{4FD_{O_2}^{eff} pO_{2,cat}P_0} \cdot j \right) \right)$$

Eq. 4.13

L_{an} and L_{cat} denote the thickness of the anode substrate (in this case: 1 mm) and the thickness of the screen-printed cathode (in this case: 45 µm). D_i^{eff} is the only unknown parameter in these equations, it is the effective molecular diffusion coefficient, which can also be expressed as [15]:

$$D_i^{eff} = \psi_{an/cat} \cdot D_{mol,i}$$

Eq. 4.14

with

$$\psi_{an/cat} = \frac{\varepsilon_{p,\,an/cat}}{\tau_{tortuosity,\,an/cat}}$$

Eq. 4.15

ψ_{an} and ψ_{cat} are the unknown structural parameters of anode and cathode, respectively, that describe the relationship between volumetric porosity $\varepsilon_{p,\,an/cat}$ and tortuosity $\tau_{tortuosity,\,an/cat}$. These two entities can, however, not be determined accurately, e.g. from microstructural analyses, and are thus often estimated in general. In this work, the structural parameters ψ_{an} and ψ_{cat} can directly be determined from impedance measurements, as shall be shown below. For this, however, the molecular diffusion coefficients $D_{mol,i}$ of the single components must be known. These, in turn, are composed of the Knudsen diffusion coefficients $D_{Knudsen,i}$ and the bulk diffusion coefficients $D_{bulk,i}$ of the individual components (Eq. 4.16) [15, 73, 90, 91]. $D_{Knudsen,i}$ can be calculated using Eq. 4.17 [75] and must be considered for structures with pore sizes in the order of the mean free path length of the diffusing particles. The binary diffusion coefficient $D_{bulk,ij}$ which is used in general for diffusion processes in the gas atmosphere, can be estimated for binary gas mixtures according to the Chapman-Enskog theory [15, 92] (Eq. 4.18). For gas mixtures consisting of more than two gases the approach by Wilke [93] (Eq. 4.19) can be used to calculate the diffusion coefficient $D_{bulk,i}$ of each gas [75]:

$$\frac{1}{D_{mol,i}} = \frac{1}{D_{bulk,i}} + \frac{1}{D_{Knudsen,i}}$$

Eq. 4.16

$$D_{Knudsen,i} = \frac{2}{3} \cdot r_{Por,el} \sqrt{\frac{8RT}{\pi M_i}}$$

Eq. 4.17

$$D_{bulk,ij} = \frac{1.86 \cdot 10^{-3} \cdot T^{1.5} \sqrt{M_i^{-1} + M_j^{-1}}}{p \cdot \sigma_{ij}^2 \cdot \Omega_D}$$

Eq. 4.18

$$D_{bulk,i} = \frac{1 - Y_i}{\displaystyle\sum_{j \neq i} (Y_j / D_{bulk,ij})} \quad (Y_i: \text{molar fraction of component } i)$$

Eq. 4.19

The constants that appear in Eqs. 4.17 and 4.18 (M_i: molar mass, σ_{ij}: average collision diameter, and Ω_D: collision integral) were taken from [94]. The constants $r_{Por,el}$, which denote the mean pore radius of each electrode structure (index „el"), were extracted from semi-quantitative image analysis of SEM micrographs of the according electrode structures. The mean pore radius of the anode was estimated to be $r_{Por,an}$ = 600 nm, the mean pore radius of the cathode was estimated to be $r_{Por,cat}$ = 600 nm. Since for these pore radii the Knudsen diffusion coefficients are in the same order of magnitude as the bulk diffusion coefficients, Knudsen diffusion has to be considered as well. The molecular diffusion coefficient $D_{mol,i}$ has been calculated according to Eqs. 4.16 to 4.19, the mean pore radii have been determined semi-quantitatively, thus the structural parameters ψ_{an} and ψ_{cat} are the only parameters necessary for obtaining the diffusion polarisation overpotential that remain to be determined. Therefore, in the impedance analyses the hydrogen and water partial pressure at the anode was specifically varied (in order to determine ψ_{an}), and the oxygen partial pressure was varied stepwise from $pO_{2,cat}$ = 0.04 atm to 0.01 atm (in order to determine ψ_{cat}). These low partial pressures were mandatory as diffusion polarisation at the cathode can only be identified unambiguously for very low oxygen concentrations (as mentioned earlier in this work). The structural parameters ψ_{an} and ψ_{cat} were then obtained by a fit of Eqs. 4.20 and 4.21 to the according resistance data $R_{1A} = R_{conc,an}(pH_{2,an}, pH_2O_{an})$ and $R_{1C} = R_{conc,cat}(pO_{2,cat})$ (Fig. 41 and Fig. 42).

$$R_{conc,an} = \left(\frac{RT}{2F}\right)^2 L_{an} \frac{1}{\psi_{an} P_0} \left(\frac{1}{D_{mol,H_2} \cdot pH_{2,an}} + \frac{1}{D_{mol,H_2O} \cdot pH_2O_{an}}\right)$$

Eq. 4.20

$$R_{conc,cat} = \left(\frac{RT}{4F}\right)^2 L_{cat} \frac{1}{D_{mol,O_2}} \frac{1}{\psi_{cat}P_0} \left(\frac{1}{pO_{2,cat}} - 1\right)$$

<div align="right">Eq. 4.21</div>

The values determined in this way (ψ_{an} = 0.13 and ψ_{cat} = 0.022) are listed in Table 12. For comparison, Ackmann et al. [43] found values of ψ_{an} = 0.156 and ψ_{cat} = 0.021-0.037 on similar electrode structures by diffusion and permeation experiments [95, 96].
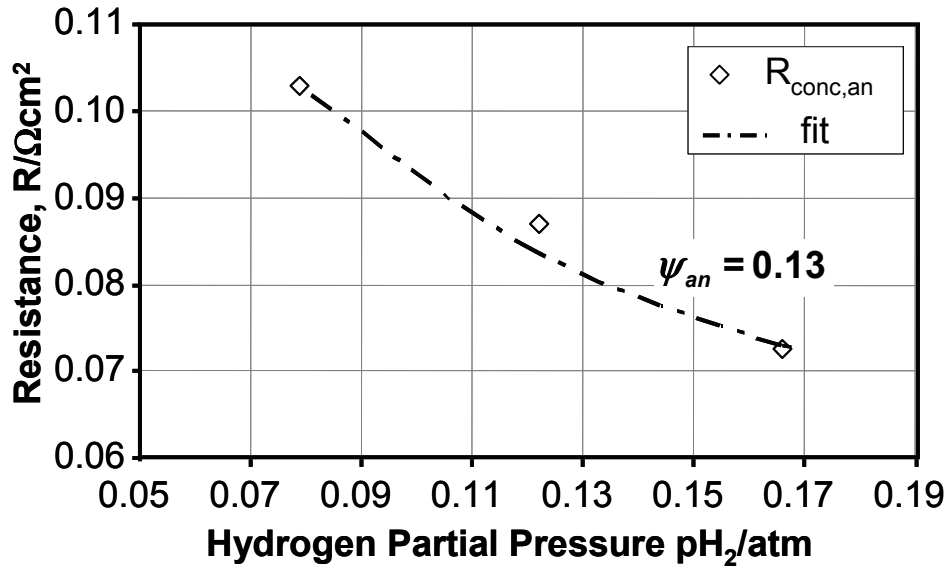
Fig. 41: Determination Ψ_{an} from Eq. 4.20. $R_{conc,an}$ [Ω·cm²] as a function of hydrogen partial pressure (pH_2O_{an} = 0.18, balance N_2) [cell# Z1_188].
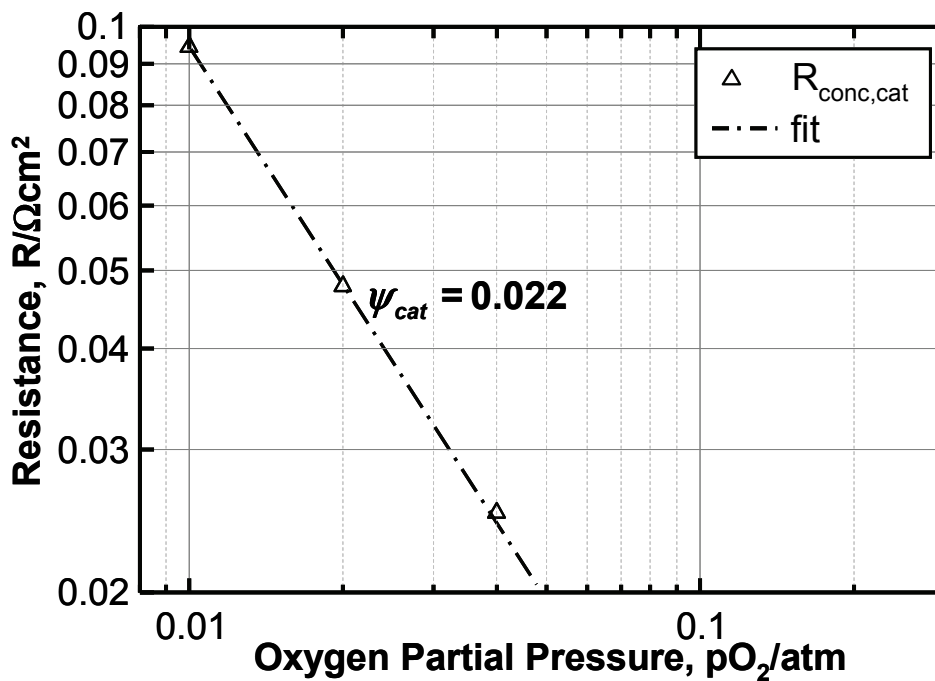
Fig. 42: Determination of parameters Ψ_{cat} from Eq. 4.21. $R_{conc,cat}$ [Ω·cm²] as a function of oxygen partial pressure on a double-logarithmic scale [cell# Z1_188].

Activation Overpotential

Activation polarisation describes the electrochemical loss mechanisms taking place mainly at the three-phase boundary where ionic-conducting, electronic-conducting and gas phase meet. An activation energy is necessary in order to overcome the energy barrier that prevents a spontaneous reaction. The higher the temperature, the higher the probability for reactants to gain the necessary activation energy, therefore the overpotentials are reduced. In most models [73-75, 77] the activation polarisation is calculated separately for anode or cathode, in both cases using the Butler-Volmer equation (Eq. 4.22).

$$ j = j_{0,el} \left[\exp\left(\alpha_{el} \frac{n_e F \eta_{act,el}}{RT} \right) - \exp\left(-\left(1-\alpha_{el}\right) \frac{n_e F \eta_{act,el}}{RT} \right) \right] \qquad \text{Eq. 4.22} $$

Here, $j_{0,el}$ is the (partial pressure and temperature dependent) exchange current density of anode/cathode, n_e the number of exchanged electrons (in our case $n_e = 2$), α_{el} the apparent charge transfer coefficient, and $\eta_{act,el}$ the activation overpotential of the according electrode (anode or cathode). The charge transfer coefficient is an indicator of the symmetry of the activation energy barrier when a positive or negative overpotential is applied [13]. In earlier models [76, 79] the Butler-Volmer equation was frequently approximated by a linear relationship (for $j/j_{0,el} < 2$) and by the Tafel equation (for $j/j_{0,el} > 4$) [73, 78]. However, this simplification leads to large deviations from the Butler-Volmer equation in the range $1 < j/j_{0,el} < 4$ which is relevant for a description of the activation overpotential [97]. Another simplification one often encounters [80, 98, 99] is the general estimate of the charge transfer coefficient as $\alpha_{el} = 0.5$, because α_{el} has so far only been determined from model geometries [100, 101] and could not accurately be determined experimentally in the case of high-performance (technologically relevant) electrode structures [102]. For instance, Holtappels et al. [103] determined $\alpha_{an} = 0.7$ in the temperature range $T = 725\text{-}845\,°C$; at higher temperatures, however, they obtained a large scatter of α_{an} values between 0.2 and 0.5. In the present work, both α_{el} values were determined (as the only parameters) from impedance measurements under load. The gas diffusion losses, particularly within the anode substrate, were hereby carefully observed during evaluation as a potential cause of error.

In the following, the so far unknown parameters required for modelling (exchange current density $j_{0,el}$ and charge transfer coefficient α_{el} of each electrode) are determined.

Partial pressure dependency of the exchange current densities $j_{0,an}$ and $j_{0,cat}$ of anode and cathode, respectively, is frequently described by the semi-empirical Eqs. 4.23 and 4.24 [102]. They contain (in contrast to the models of [74] and [79]) a power law ansatz for the partial pressure dependency as well as an Arrhenius-type temperature dependency.

$$j_{0,an} = \gamma_{an} \left(\frac{pH_{2,an}}{P} \right)^a \left(\frac{pH_2O_{an}}{P} \right)^b \exp \left(-\frac{E_{act,an}}{RT} \right) \qquad \text{Eq. 4.23}$$

$$j_{0,cat} = \gamma_{cat} \left(\frac{pO_{2,cat}}{P} \right)^m \exp \left(-\frac{E_{act,cat}}{RT} \right) \qquad \text{Eq. 4.24}$$

The prefactors γ_{an} and γ_{cat}, the exponents a, b, and m as well as the activation energies $E_{act,an}$ and $E_{act,cat}$ are not known and have to be determined. The exponents are quite difficult to determine in particular [80]. In most cases [76, 77, 80, 81, 84, 104] m was estimated as $m = 0.25$, but not precisely determined. Furthermore, an accurate and separate determination of the two exponents a and b so far was only possible for symmetrical cells. For asymmetrical cells [82] only simplified approaches are to be found in literature. Whereas Ni et al. [81] sets both a and b to unity, this approach being pursued in [75, 77, 80], Yamamura et al. [82] use values of $a = 1$ and $b = -0.5$. The latter value of b was experimentally determined by Yamamura on model anodes (Nickel pattern electrode) by varying the water partial pressure, yet values for a and b could also not be obtained separately in this case. By comparing both aforementioned approaches, Costamagna et al. [84] found that for $b = -0.5$ the gas composition at the anode could be varied over a wide range without leading to a too large deviation between simulation results and measured data.

Determination of Exponents a, b and m

In order to make a prediction of the activation overpotential more reliable, the exponents a and b are determined separately in this study. To ensure that water partial pressure and hydrogen partial pressure could be varied independently of each other, a defined amount of inert gas (in our case: nitrogen) was added to the gas mixture (cf. Table 11). This procedure, in combination with the equivalent circuit developed in chapter 4.1, made it possible to experimentally determine the resistance of the activation polarisation at the anode $R_{act,an} = R_{2A} + R_{3A}$ as a function of pH_2O_{an} or $pH_{2,an}$ from impedance measurements under open-circuit conditions. The DRTs calculated from the measured impedance curves are shown in Fig. 43a and Fig. 43b for four different $pH_{2,an}$ ($pH_{2,an} = 0.05, 0.2, 0.4, 0.8$ atm) and four different pH_2O_{an} ($pH_2O_{an} = 0.04, 0.12, 0.2, 0.4$ atm), respectively.

Table 11: Partial pressures of H_2, H_2O, and N_2, that were selected in order to determine the parameters *a* and *b*.

Purpose	$pH_{2,an}$ / atm	pH_2O_{an} / atm	$pN_{2,an}$ / atm
Determination of parameter *a*			
	0.80	0.20	0.0
	0.40	0.20	0.40
	0.20	0.20	0.60
	0.10	0.20	0.70
	0.05	0.20	0.75
Determination of parameter *b*			
	0.60	0.40	0.0
	0.60	0.20	0.20
	0.60	0.12	0.28
	0.60	0.08	0.32
	0.60	0.04	0.36
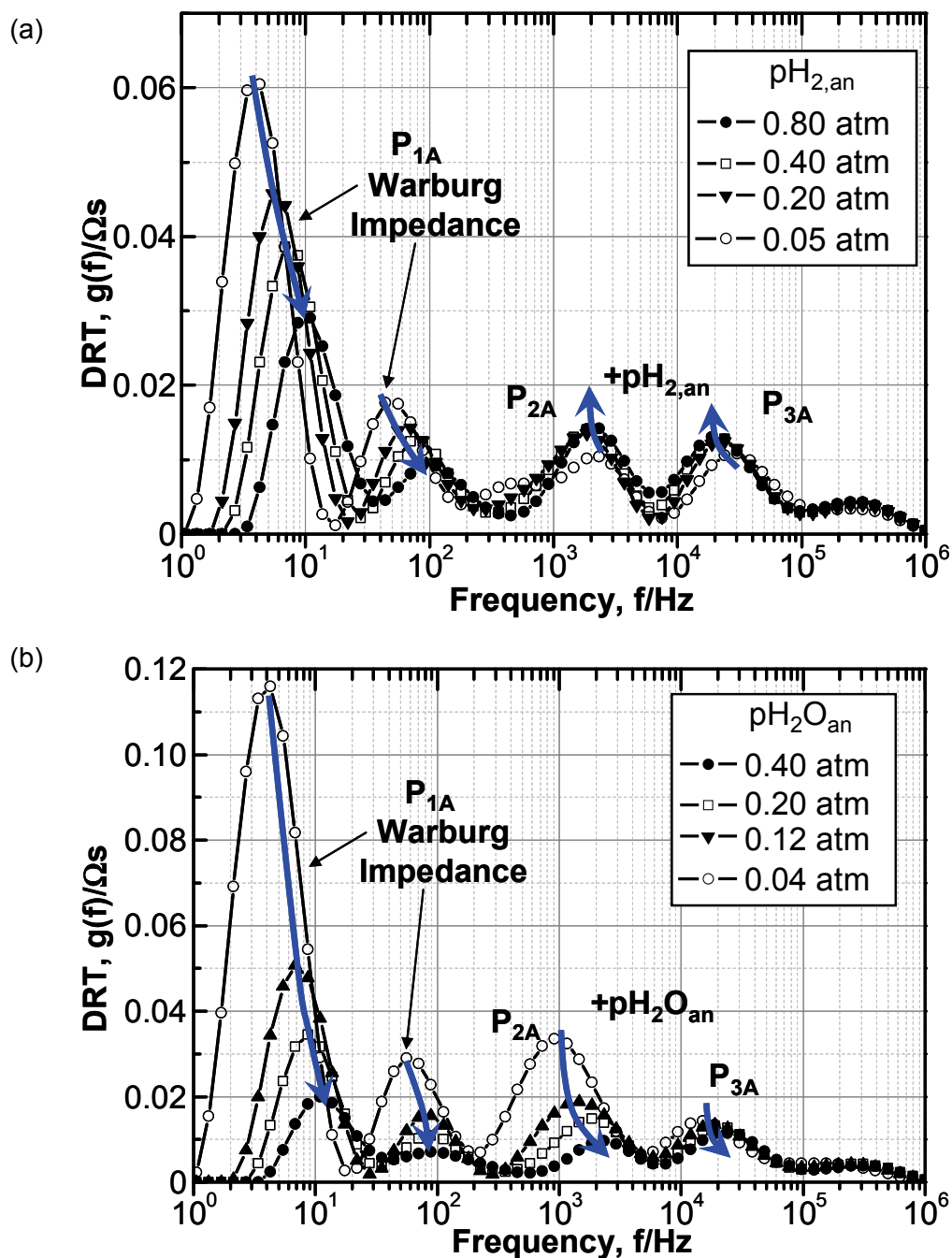
Fig. 43: DRTs calculated from the impedance curves. (a) DRTs at various hydrogen partial pressures at the anode ($pH_{2,an}$ = 0.05, 0.20, 0.40, 0.80 atm) and constant pH_2O_{an} = 0.20 atm, $pO_{2,cat}$ = 0.21 atm (air) and T = 800 °C (b) DRTs at various water partial pressures at the anode (pH_2O_{an} = 0.04, 0.12, 0.20, 0.40 atm) and constant $pH_{2,an}$ = 0.60 atm, $pO_{2,cat}$ = 0.21 atm (air) and T = 800 °C) [cell# Z1_188].

As can be seen, the anodic gas diffusion process P_{1A} shows a significant dependency on the water and hydrogen partial pressure respectively. This strong dependency of the gas diffusion overpotential on the partial pressures can be explained by Eq. 4.20 which reveals a reciprocal relationship between the gas diffusion resistance $R_{conc,an}$ and the according gas partial pressures ($pH_{2,an}$ and pH_2O_{an}, respectively).

In contrast to P_{1A}, the processes P_{2A} and P_{3A} exhibit a subordinate dependence on pH_2O_{an} and $pH_{2,an}$, respectively. P_{2A} and P_{3A} decrease with increasing pH_2O_{an}, but increase a bit with increasing $pH_{2,an}$. These observations are in agreement with the quantitative results of the according CNLS fits, as shall be shown in the following.

From Eq. 4.25 which relates the resistance of the activation polarisation to the activation overpotential one can derive (Eq. 4.26) a relationship between the exchange current densities and the resistance.

$$\left.\frac{d\eta_{act,el}}{dj}\right|_{j=0} = \frac{RT}{2F \cdot j_{0,el}} = R_{act,el} \qquad \text{Eq. 4.25}$$

$$j_{0,el} = \frac{1}{R_{act,el}} \cdot \frac{RT}{2F} \qquad \text{Eq. 4.26}$$

With the help of Eq. 4.26 the parameters a and b could be determined – for the first time separately on anode supported cells – by fitting Eq. 4.23 to the data obtained from impedance analyses ($R_{act,an}(pH_{2,an})$ and $R_{act,an}(pH_2O_{an})$ with $R_{act,an} = R_{2A} + R_{3A}$). In Fig. 44a and Fig. 44b the resistances $R_{act,an}(pH_{2,an})$ and $R_{act,an}(pH_2O_{an})$ are plotted, respectively, as a function of hydrogen / water partial pressure on a double-logarithmic scale.

The parameters a = -0.10 and b = 0.33 can be extracted from the negative value of the slope of the linear fit, in each case. The negative sign is a result of the inverse proportionality between exchange current density and the resistance (Eq. 4.26).

Similarly, the parameter m could also be determined using the equivalent circuit presented in this work and the data from open-circuit impedance measurements with specifically varied oxygen partial pressures at the cathode. As already discussed in chapter 4.1, the diffusion process P_{1C} can only be observed for very low oxygen partial pressures in the DRT below 3 Hz (Fig. 45a). Simultaneously, a further change in the DRT is indicated between 4 and 1000 Hz. This can be attributed to an enhancement of the activation polarisation losses (R_{2C}) in the cathode by decreasing $pO_{2,cat}$. In Fig. 45b the resistance $R_{2C} = R_{act,cat}(pO_{2,cat})$ derived from the CNLS fit is plotted as a function of oxygen partial pressure on a double-logarithmic scale. The negative value of the slope of the linear fit, in turn, yields the parameter m = 0.22.
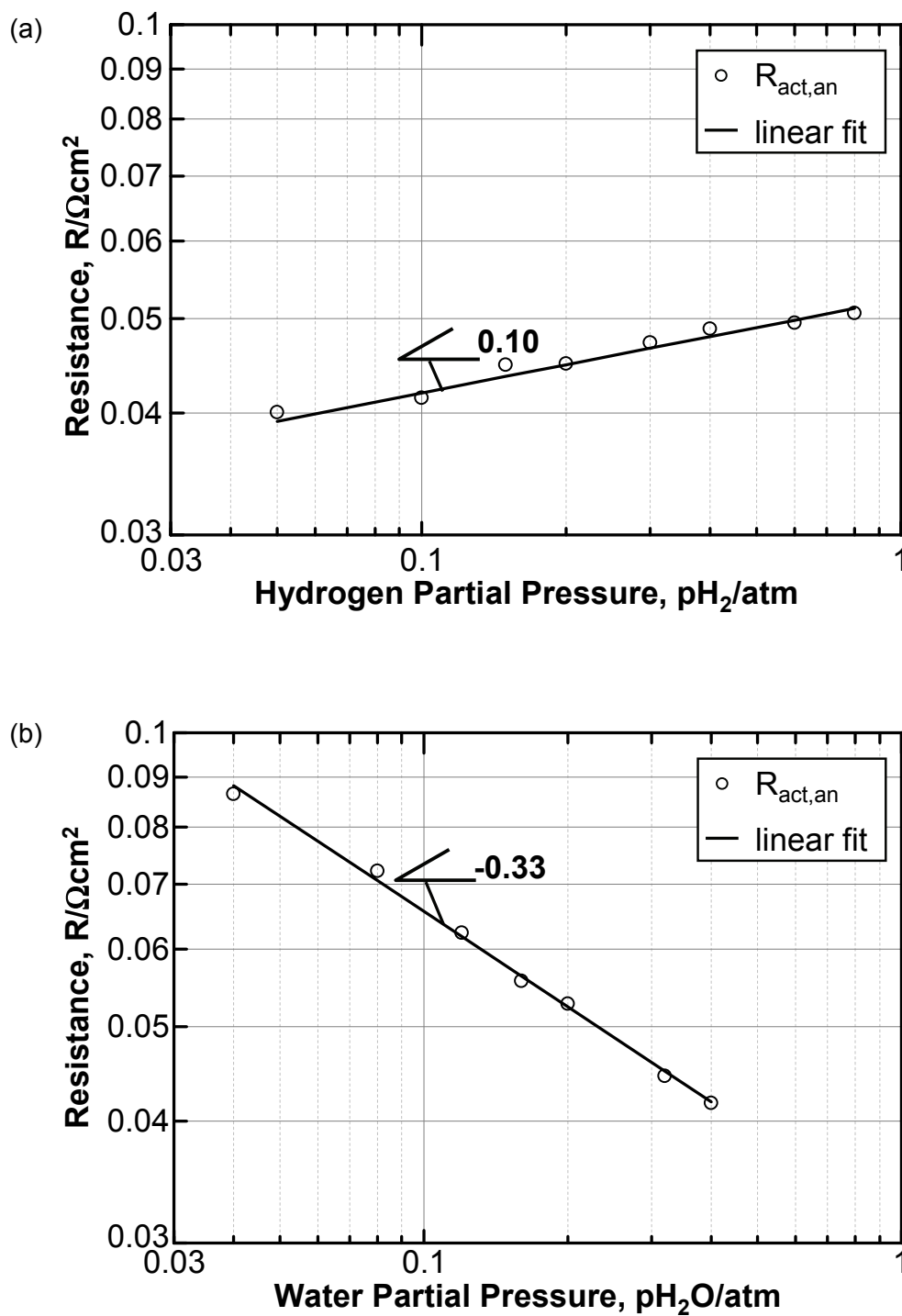
Fig. 44: Determination of parameters *a* and *b* from Eq. 4.23. (a) $R_{act,an}$ [Ω·cm²] as a function of hydrogen partial pressure on a double-logarithmic scale. (b) $R_{act,an}$ [Ω·cm²] as a function of water partial pressure on a double-logarithmic scale [cell# Z1_188].
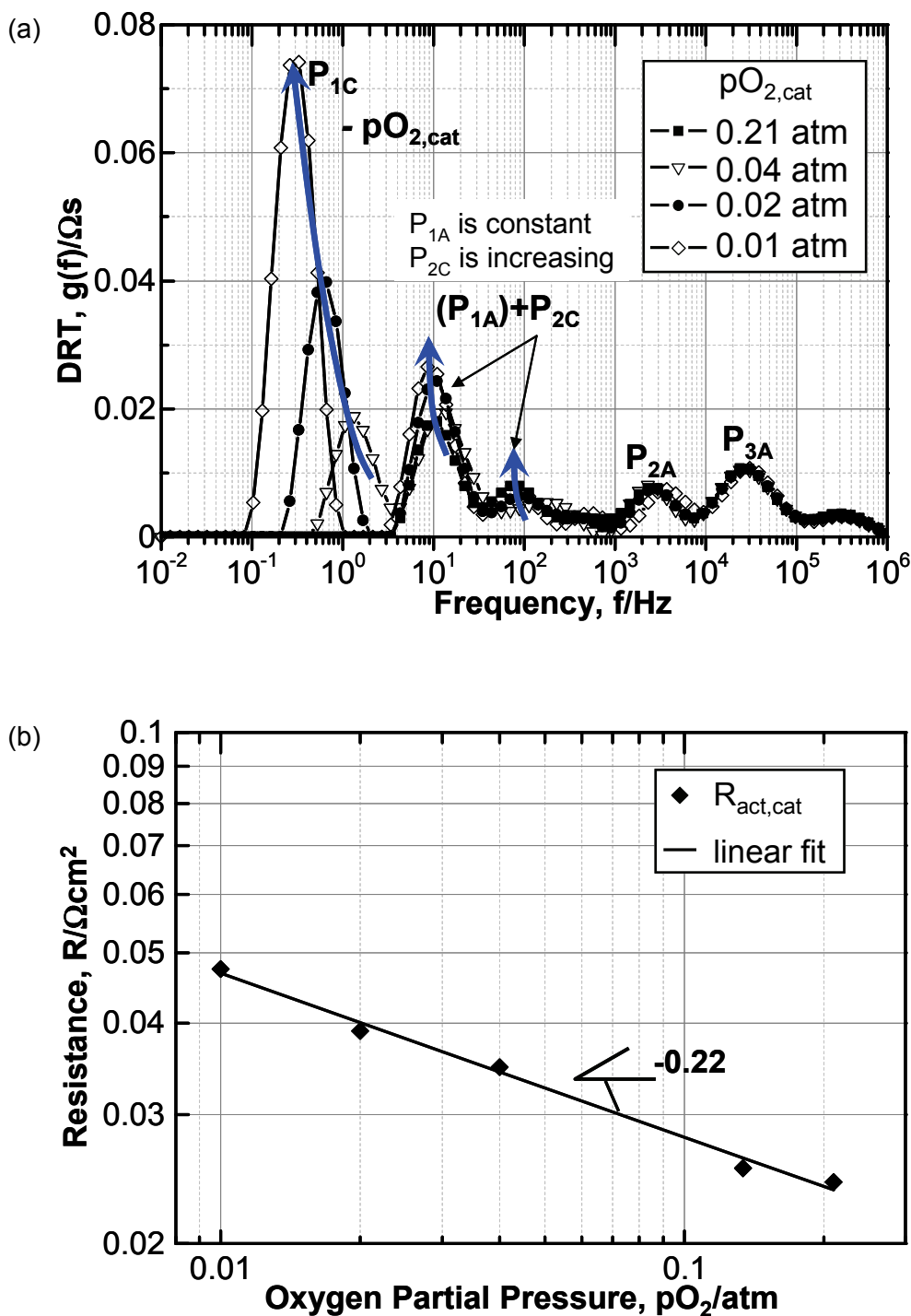
Fig. 45: Determination of parameter *m* from Eq. 4.24. (a) DRTs at various oxygen partial pressures at the cathode ($pO_{2,cat}$ = 0.01, 0.02, 0.04, 0.21 atm) and constant pH_2O_{an} = 0.60 atm, $pH_{2,an}$ = 0.40 atm and temperature *T* = 800 °C. (b) $R_{act,cat}$ [$\Omega \cdot cm^2$] as a function of oxygen partial pressure on a double-logarithmic scale [cell# Z1_188].

Determination of Activation Energies $E_{act,an}$ and $E_{act,cat}$

The parameters γ_{an} and γ_{cat} as well as $E_{act,an}$ and $E_{act,cat}$ from Eqs. 4.23 and 4.24 have to be determined from open-circuit impedance measurements as well. The activation energies $E_{act,an}$ and $E_{act,cat}$ of the anodic and the cathodic exchange current densities can be derived from measurements of the activation polarisation resistances of anode ($R_{act,an}(T)$) and cathode ($R_{act,cat}(T)$) as a function of temperature (571…871 °C).

Fig. 46a shows the DRTs calculated from impedance measurements for five different temperatures. As can be seen immediately, the two processes P_{2A} and P_{3A} are combined to one single peak with decreasing temperature. In the low-frequency regime of the DRTs, a strong temperature dependency of process P_{2C} (activation polarisation of the cathode) can be observed. At temperatures below 671 °C, this process already covers the anodic gas diffusion process P_{1A} completely.

In order to determine the unknown parameters γ_{el} and $E_{act,el}$, the resistances $R_{2A}(T) + R_{3A}(T) = R_{act,an}(T)$ and $R_{2C}(T) = R_{act,cat}(T)$ derived from a CNLS fit of the impedance curves were, in turn, fitted with the Arrhenius equation (Eq. 4.27) (see Fig. 46b).

$$R_{act,el}\left(T\right) = B_{el}\exp\left(\frac{E_{act,el}}{RT}\right)$$

Eq. 4.27

The very high quality (R² > 0.998) of these fits shown in Fig. 46b confirms that the Arrhenius ansatz (Eqs. 4.23 and 4.24) is a valid one for modelling the temperature behaviour of the exchange current densities.

From these fits the following activation energies and prefactors can be extracted:

• $E_{act,an}$ = 105.04 kJ/mol (1.09 eV) and B_{an} = 3.827·10^{-7} $\Omega \cdot cm^2$ for the anode.

• $E_{act,cat}$ = 139.86 kJ/mol (1.45 eV) and B_{cat} = 4.032·10^{-9} $\Omega \cdot cm^2$ for the cathode.

In literature, activation energies between 0.7 eV and 1.1 eV are reported for technical Ni/YSZ anodes ([105] gives an overview). The value determined in this work ($E_{act,an}$ = 1.09 eV) is in good agreement with results by DeBoer [106], Geyer [107] and Brown [108], who found activation energies ranging from 1 to 1.1 eV.

It should, however, be stated here that all these values are *apparent* activation energies. As Sonn et al. [44] showed in great detail for symmetrical anodes (electrolyte-supported cells), the thermal behaviour of the activation polarisation in fact depends on two coupled processes: on the one hand, this is the oxygen ion transport within the YSZ matrix of the anode, on the other hand, the charge transfer resistance at the TPB Ni/YSZ/gas phase. By using a transmission line model instead of two serial RQ-elements (RQ_{2A}, RQ_{3A}), as in the present study, Sonn et al. were able to determine separate values for the activation energy of the ionic transport losses (0.904 eV) and of the charge transfer resistance (1.35 eV).

However, the results presented above show that the use of two RQ-elements in the equivalent circuit is a more than sufficient means to precisely and unambiguously determine the operating parameter dependency of the anodic activation polarisation resistance within the scope of this work.

In comparison with the anode, the activation energy of the L58SCF cathode shows a significantly higher value. Moreover, the values reported in the literature vary very strongly from 1.2 up to 1.6 eV [42, 48, 109-111]. The best agreement with the value determined in this work is found by Esquirol et al. [42] who reported an activation energy of 1.39±0.09 eV. It should be briefly noted here, that there may be a strong influence of the cathode microstructure in this respect. As recently shown, e.g. by Peters et al. [112], the (mean) porosity and the (mean) grain size of chemically similar cathodes can strongly differ, thus leading to a scatter of the activation energy.
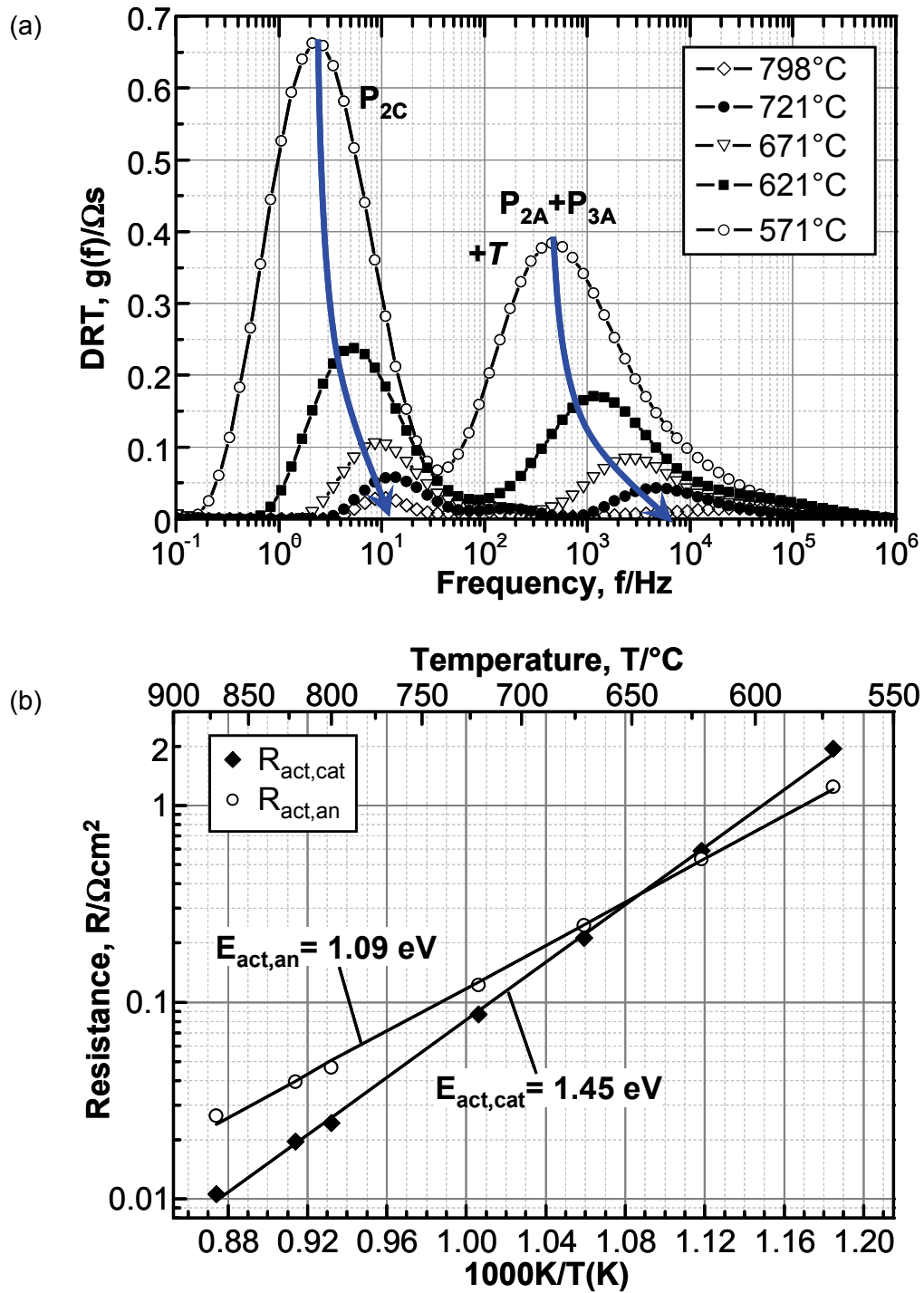
Fig. 46: (a) DRTs at different temperatures (T = 798, 721, 671, 621, 571 °C) and constant pH_2O_{an} = 0.20 atm, $pH_{2,an}$ = 0.80 atm and $pO_{2,cat}$ = 0.21 atm (air). (b) Activation polarisation resistances $R_{act,an}$ and $R_{act,cat}$ [$\Omega \cdot cm^2$] as a function of temperature T [cell# Z1_188].

Determination of Prefactors γ_{an} and γ_{cat}

With the help of Eq. 4.26, which relates $R_{act,el}$ to $j_{0,el}$, and by inserting Eqs. 4.23 and 4.24, respectively, into Eq. 4.27 one obtains

$$\gamma_{an}\left(pH_{2,an}\right)^{a}\left(pH_2O_{an}\right)^{b} \equiv \frac{RT}{2FB_{an}}$$

<div align="right">Eq. 4.28</div>

$$\gamma_{cat}\left(pO_{2,cat}\right)^{m} \equiv \frac{RT}{2FB_{cat}}$$

<div align="right">Eq. 4.29</div>

The temperature dependent prefactors γ_{an} and γ_{cat} of the exchange current densities can now be calculated from Eqs. 4.28 and 4.29 using the values for B_{an} und B_{cat} determined above. By inserting the previously determined values for the exponents a, b, and m, and the constant partial pressures (chosen for the measurements at varying temperatures) $pH_{2,an} = 0.80$ atm, $pH_2O_{an} = 0.20$ atm, and $pO_{2,cat} = 0.21$ atm (air), the expressions for γ_{an} and γ_{cat} are determined to be $\gamma_{an} = (1.83 \cdot 10^6 \cdot T)$ A/m^2 and $\gamma_{cat} = (1.52 \cdot 10^8 \cdot T)$ A/m^2.

In contrast to the findings shown here, in the existing literature [75-77, 80] the pre-exponential factors γ_{an} and γ_{cat} of Eqs. 4.23 and 4.24 are assumed to be independent of temperature. Thus, generally a constant value is used over the entire temperature range of simulation. Nevertheless, values for these parameters reported in literature [75-77, 80] vary by up to two orders of magnitude which makes a comparison difficult. Values ranging from $\gamma_{an} = 5.5 \cdot 10^{10}$ A/m^2 to $5.5 \cdot 10^8$ A/m^2 can be found, and for γ_{cat} the values vary over a range of one decade as well ($7 \cdot 10^8$ A/m$^2 < \gamma_{cat} < 7 \cdot 10^9$ A/m^2). The literature values for γ_{cat} are smaller than those determined by us. Considering the influence of the parameters a, b, and m (which were for the first time experimentally determined in this study and take on significantly smaller values than previously assumed in literature) on the calculation of γ_{an} and γ_{cat}, the values for the latter prefactors, and thus also for the exchange current densities, are much larger than those found in literature. This implies that the anode-supported cells with screen-printed L58SCF cathode analysed in this work have very low activation resistances.

Determination of Charge Transfer Coefficients α_{an} and α_{cat}

The sole remaining parameters to be determined are the charge transfer coefficients α_{an} and α_{cat}. Different to the previous procedure, these are obtained by impedance measurements under load, since the charge transfer coefficients affect the current-dependent behaviour of the activation overpotential. These impedance measurements were carried out at a high degree of fuel utilization $\beta = 62$ % (i. e. at $pH_{2,an} = 0.38$ atm and $pH_2O_{an} = 0.62$ atm), $pO_{2,cat} = 0.21$ atm (air), and at a temperature of 800 °C. The load current density was increased stepwise ($j = 0, 0.2, 0.4, 0.6, 1.0, 1.4, 1.8, 2.2$ A/cm²). The maximum current

density chosen (2.2 A/cm²) under the given operating conditions can only be reached in cells with very low anodic and cathodic polarisation losses.

The DRTs calculated from the resulting impedance curves and the current-dependent differential resistances $d\eta_{act,an}/dj = dR_{act,an}$ and $d\eta_{act,cat}/dj = dR_{act,cat}$ derived from the CNLS fit of the equivalent circuit from Fig. 26, are shown in Fig. 47.
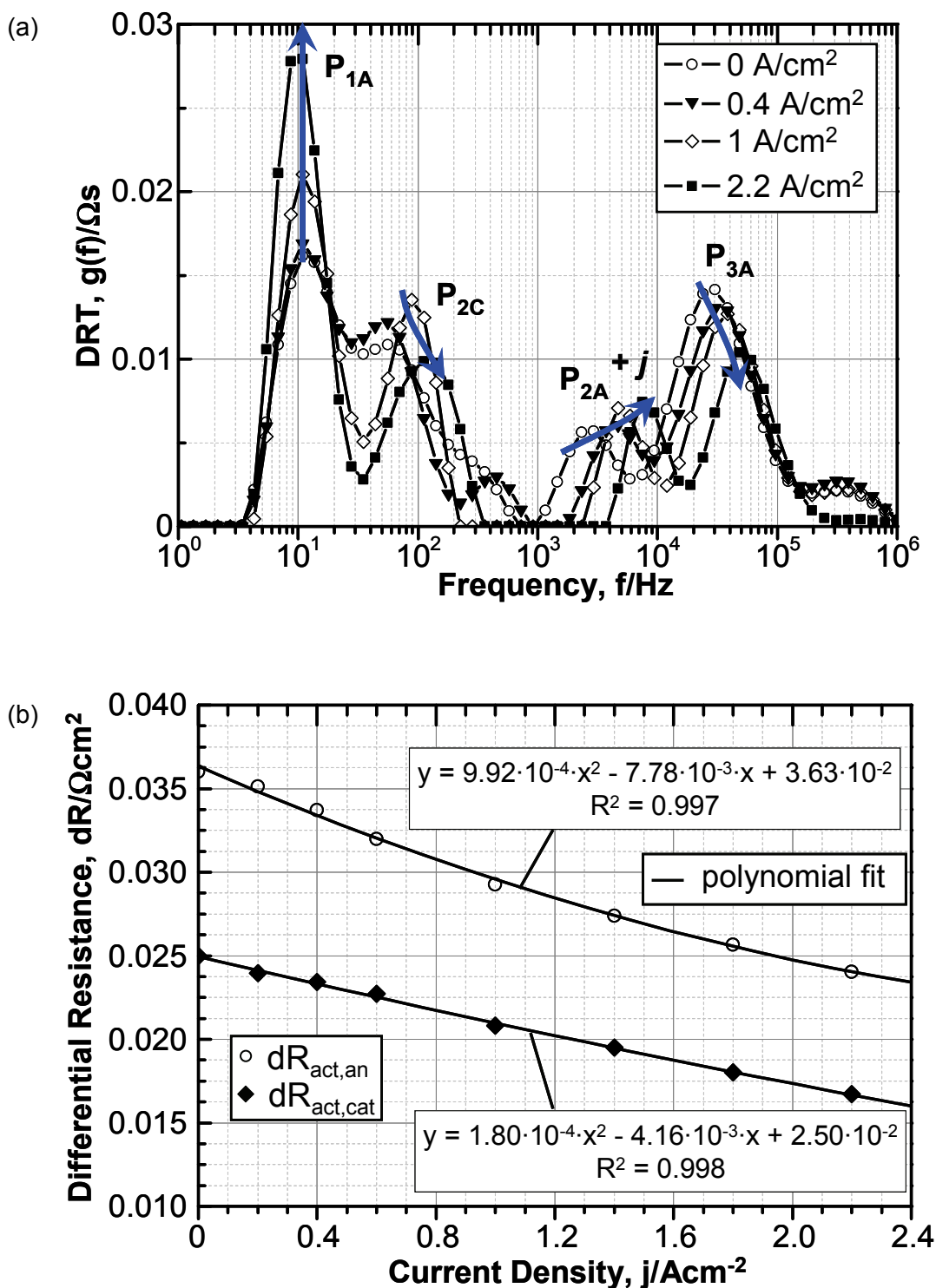
Fig. 47: Determination of charge transfer coefficients α_{el}: (a) DRTs at various current densities (j = 0.0, 0.4, 1.0, 2.2 A/cm^2) and constant pH_2O_{an} = 0.62 atm, $pH_{2,an}$ = 0.38 atm, $pO_{2,cat}$ = 0.21 atm (air) and T = 800 °C. (b) $dR_{act,an}$ and $dR_{act,cat}$ [mΩ·cm^2] as a function of current density j, together with the two 2nd-order polynomial fits [cell# Z1_188].

In order to calculate the current-dependent activation overpotential $\eta_{act,el}(j)$, one has to integrate the function $dR_{act,el}(j)$ with respect to the electrical current density j. To this end, $dR_{act,an}(j)$ and $dR_{act,cat}(j)$, both obtained from the measurements, are, in a first step, fitted by a second-order polynomial. Both fit results are shown in Fig. 47b. Both, $dR_{act,an}(j)$ and $dR_{act,cat}(j)$ can obviously be described very well by a second-order polynomial in the load range investigated here. The according polynomial equations read:

$$dR_{act,an}(j) = \frac{d\eta_{act,an}(j)}{dj} = 9.92 \cdot 10^{-4} j^2 - 7.78 \cdot 10^{-3} j + 3.63 \cdot 10^{-2} \qquad \text{Eq. 4.30}$$

$$dR_{act,cat}(j) = \frac{d\eta_{act,an}(j)}{dj} = 1.80 \cdot 10^{-4} j^2 - 4.16 \cdot 10^{-3} j + 2.50 \cdot 10^{-2} \qquad \text{Eq. 4.31}$$

Integration of Eqs. 4.30 and 4.31 with respect to the current density j yields the following expressions for the current-dependent activation overpotentials $\eta_{act,an}$ and $\eta_{act,cat}$:

$$\eta_{act,an}(j) = \left(\frac{1}{3}\right) 9.92 \cdot 10^{-4} j^3 - \left(\frac{1}{2}\right) 7.78 \cdot 10^{-3} j^2 + 3.63 \cdot 10^{-2} j + c_{an} \qquad \text{Eq. 4.32}$$

$$\eta_{act,cat}(j) = \left(\frac{1}{3}\right) 1.80 \cdot 10^{-4} j^3 - \left(\frac{1}{2}\right) 4.16 \cdot 10^{-3} j^2 + 2.50 \cdot 10^{-2} j + c_{cat} \qquad \text{Eq. 4.33}$$

Due to the boundary condition $\eta_{act,el}(j = 0) = 0$, the integration constants c_{el} are both zero.

By simply inserting the current densities adjusted during the measurements into Eqs. 4.32 and 4.33, the corresponding activation overpotentials can be calculated for these operating points. In a last step, the Butler-Volmer equation of both electrodes (Eq. 4.22) can be fitted to the corresponding data $j(\eta_{act,el})$. Fig. 48 shows the current densities as a function of the calculated overpotentials $\eta_{act,an}$ und $\eta_{act,cat}$ as well as the fitted Butler-Volmer curves. It can easily be seen that the anodic and cathodic overpotentials can very well be described by a Butler-Volmer ansatz in the load current range investigated here. The fit results yield the charge transfer coefficients $\alpha_{an} = 0.590$ and $\alpha_{cat} = 0.650$.
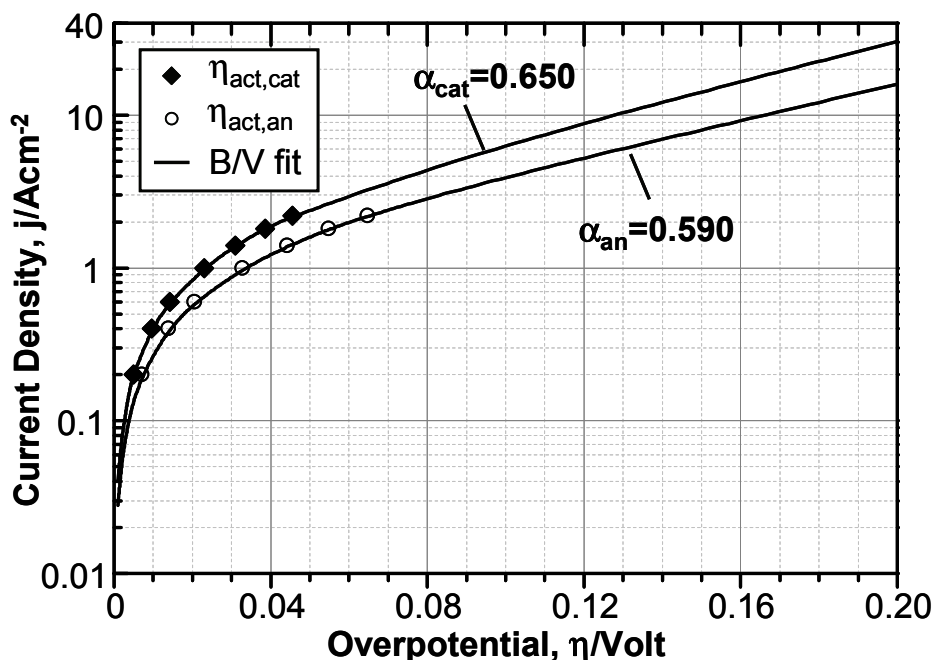
Fig. 48: Determination of charge transfer coefficients α_{el}: current density j as a function of activation overpotential $\eta_{act,an}$ and $\eta_{act,cat}$, together with the according Butler-Volmer fits [cell# Z1_188].

These values lie within the range ($0.5 < \alpha_{an/cat} < 1$) reported in literature [80, 98-101, 103, 113] for the technical electrode structures investigated in this work. These coefficients can alternatively be determined by fitting the Tafel equation to the measured I-U curves [13]. This, however, is only valid if the gas diffusion losses in the flow field of the experimental setup and within the porous electrode structure can be neglected as compared to the activation losses. Furthermore, it must be kept in mind that the Tafel equation is only a valid approximation of the Butler-Volmer equation for current densities $j > 4\,j_{0,el}$. Such fairly high current densities, however, do not occur in technical electrode structures. Nevertheless, the validity of these assumptions is frequently not sufficiently scrutinised in literature [103, 114]. This can lead to an estimate for the charge transfer coefficient which is too small, as can easily be seen from the Butler-Volmer equation (Eq. 20). Besides, due to the lack of experimental data, α_{an} and α_{cat} are quite often generally assumed to be $\alpha_{an} = 0.50$ and $\alpha_{cat} = 0.50$ [80, 98, 99].

The parameters ψ_{an}, ψ_{cat}, a, b, m, γ_{an}, γ_{cat}, B_{ohm}, $E_{act,ohm}$, $E_{act,an}$, $E_{act,cat}$, as well as α_{an} and α_{cat}, all determined in this section, are summarised in Table 12.

Table 12: Modelling parameters determined from open-circuit impedance measurements (with the exception of α_{an} and α_{cat}, which are obtained from EIS measurements under load).

Parameter	Value/Expression	Unit
B_{ohm}	$4.1879 \cdot 10^{12}$	$S \cdot K/m^2$
$E_{act,ohm}$	90.31	kJ/mol
a	-0.10	-
b	0.33	-
m	0.22	-
γ_{an}	$1.82527 \cdot 10^6 \cdot T$	A/m^2
γ_{cat}	$1.51556 \cdot 10^8 \cdot T$	A/m^2
$E_{act,an}$	105.04	kJ/mol
$E_{act,cat}$	139.86	kJ/mol
α_{an}	0.59	-
α_{cat}	0.65	-
ψ_{an}	0.13	-
ψ_{cat}	0.022	-

4.3.2 Simulation Results

This section contains an investigation and subsequent discussion of the effect of the operating temperature and gas compositions at anode and cathode, respectively, on the model prediction of the current-voltage characteristics. This includes the validation of I-U curves predicted by the model with experimentally determined data, as well as the comparison of the present simulation results with the results of previous modelling attempts.

Temperature Dependence

At high operating temperatures the electrochemical reactions at the electrodes are faster, as a result the overpotentials due to activation polarisation are lower. Moreover, the temperature dependence of the ohmic losses $R_{ohm}(T)$ exhibit an Arrhenius-type behaviour (Eq. 4.6), which also leads to lower ohmic losses at high temperatures. However, higher temperatures also yield lower open-circuit voltages (Eq. 4.3). These temperature-dependent characteristics typical of the I-U curves can be observed for all predicted curves (Fig. 49). Furthermore, for all operating temperatures within the temperature range investigated (621-821 °C) and for all current densities, the deviation Δ between simulated I-U curves and measured data lies within a range of 0.01 % $\leq \Delta \leq$ 4.75 % (see Table 13). This suggests that the modelling approaches chosen are correct and also that the determination of the modelling parameters (activation energies $E_{act,an}$, $E_{act,cat}$ of anode and cathode, prefactor B_{ohm}, as well as activation energy $E_{act,ohm}$ of the temperature-dependent ohmic resistance) is precise.
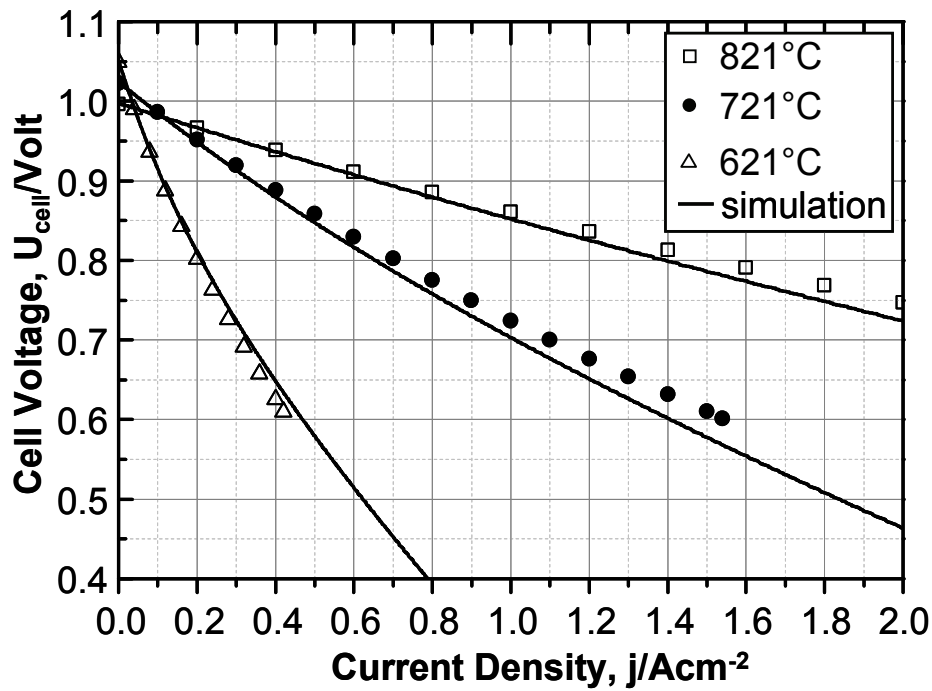
Fig. 49: Simulated (with the model presented in chapter 4.3.1 as well as the modelling parameters from Table 12; lines) and measured (symbols) I-U curves for three different temperatures T **= 821, 721, 621 °C and constant** $pO_{2,cat}$ **= 0.21 atm (air),** $pH_{2,an}$ **= 0.80 atm, and** pH_2O_{an} **= 0.20 atm [cell# Z1_188].**

Table 13: Simulated current-voltage data pairs ($U_{cell,simu}$) (j = 0, 0.2, 0.4 and 1.4 A/cm²) and their deviation (Δ) from measured data ($U_{cell,meas}$) (curves shown in Fig. 49).

Measured and Simulated Value and Deviation Δ	T=821°C	T=721°C	T=621°C
$U_{cell,meas}$ at 0.2 A/cm^2	0.967 V	0.952 V	0.801 V
$U_{cell,simu}$ at 0.2 A/cm^2	0.967 V	0.948 V	0.810 V
Deviation Δ (%)	<0.01 %	-0.42 %	+1.12 %
$U_{cell,meas}$ at 0.4 A/cm^2	0.938 V	0.888	0.625 V
$U_{cell,simu}$ at 0.4 A/cm^2	0.936 V	0.880 V	0.648 V
Deviation Δ (%)	-0.2 %	-0.90 %	+3.7 %
$U_{cell,meas}$ at 1.4 A/cm^2	0.813 V	0.631 V	-
$U_{cell,simu}$ at 1.4 A/cm^2	0.799 V	0.601 V	-
Deviation Δ (%)	-1.72 %	-4.75 %	-

Diffusion Overpotential at the Cathode

The model behaviour with respect to variations of the gas composition at the cathode is analysed for various oxygen partial pressures $pO_{2,cat}$ (0.21 atm (air), 0.13 atm, 0.04 atm, 0.02 atm, and 0.01 atm). Hydrogen partial pressure ($pH_{2,an} = 0.40$ atm), water partial pressure ($pH_2O_{an} = 0.60$ atm), and temperature ($T = 800$ °C) were kept constant. At low oxygen partial pressures the limiting current at the cathode decreases [75, 79], which leads to expect a significant drop in the cell voltage already at fairly small current densities. As a comparison between the measured I-U curves at different cathodic oxygen partial pressures shows (Fig. 50), diffusion polarisation may indeed not be neglected for $pO_{2,cat} < 0.04$ atm.

Initially, the structural parameter $\psi_{cat} = 0.022$ derived in the previous section was used for the simulation. However, as Fig. 50 shows, the recorded cell voltage drop cannot be achieved using this value of $\psi_{cat} = 0.022$ (at least for the cases where $pO_{2,cat} < 0.04$ atm).
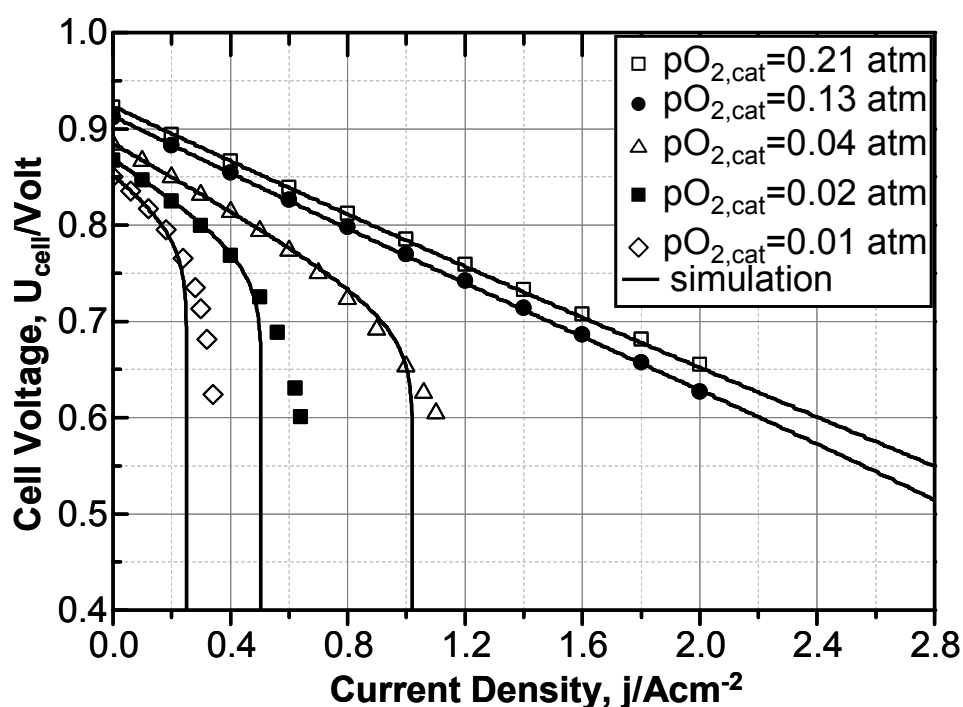
Fig. 50: Simulated (with the model presented in chapter 4.3.1 as well as the modelling parameters from Table 12; lines) and measured (symbols) I-U curves at five different cathode oxygen partial pressures ($pO_{2,cat} = 0.01, 0.02, 0.04, 0.13, 0.21$ atm). For all curves shown in this figure $pH_{2,an} = 0.40$ atm, $pH_2O_{an} = 0.60$ atm and $T = 800$ °C were set constant [cell# Z1_188].

For a more detailed discussion of this phenomenon the measured and simulated (solid line) I-U curve at $pO_{2,cat} = 0.01$ atm are shown again separately in Fig. 51. For the measured I-U curve at $pO_{2,cat} = 0.01$ atm a limiting current density of $j_{lim,cat,measured} \approx 0.34$ A/cm^2 is estimated. The fact that the voltage drop in the simulated curve occurs at lower current densities ($j_{lim,cat,model} \approx 0.25$ A/cm^2), as compared to the measured curve, could be an indication that the actual value of ψ_{cat} should be higher than the one derived in the previous section of this work.

Nevertheless, it is believed that the factor ψ_{cat} derived in this work is correct. The higher limiting current ($j_{lim,cat,measured} \approx 0.34$ A/cm^2) of the recorded curve is most probably caused by the pO_2 - dependent penetration depth of the ionic current density inside the cathode structure. When considering a LSCF MIEC-cathode, a decrease in $pO_{2,cat}$ results in an increased penetration depth of the ionic current [21, 23]. This, in turn, implicates that the effective diffusion length of the oxygen gas molecules from the gas channel to the electrochemical active region must decrease. Hence the limiting current density rises.

In summary, this means that for such fairly low oxygen partial pressures the proposed model breaks down and a separate treatment of gas diffusion and charge transfer is no more allowed. However, here it should be noted, that these low oxygen partial pressures ($pO_{2,cat} < 0.04$ atm) are far away from values reached in real operating systems. Real systems are generally operated with overstoichiometric air flow rates (the excess air in the cathode is necessary for cooling the cell). Therefore $pO_{2,cat}$ never goes below a value of 0.1 atm.

Even thought the model limitation described above should be addressed carefully in a future work, in the following an empirical ("provisory") tentative of solution to this problem will be presented.

It can be easily shown [75, 79] that the limiting current density ($j_{lim,cat}$) is directly proportional to ψ_{cat}. Therefore, to reach the recorded limiting current density $j_{lim,cat,measured} \approx 0.34$ A/cm^2 the parameter ψ_{cat} needs to be multiplied by the factor $j_{lim,cat,measured}/j_{lim,cat,model} = 1.36$. The corrected structural parameter is therefore equal to $\psi_{cat,corr} = 1.36 \cdot \psi_{cat} = 0.03$.

In Fig. 51 the simulated I-U curve, using the corrected structural parameter, is shown (dashed line). As can be seen, this time, the measured limiting current density is reached by the simulated curve. However, now the simulation deviates significantly from the measured data in the lower current density range. By multiplying the actual current dependent concentration overpotential with a factor of two ($\eta_{conc,cat,corr} = 2 \cdot \eta_{conc,cat}$) a good agreement between simulated and measured curve is finally reached (cf. dotted line in Fig. 51).

Fig. 52 shows the simulated I-U curves (for $pO_{2,cat} \in \{0.21, 0.13, 0.04, 0.02, 0.01\}$ atm) using the corrected structural parameter and the doubled cathode diffusion overpotential ($\psi_{cat,corr} = 0.03$ and $\eta_{conc,cat,corr} = 2 \cdot \eta_{conc,cat}$). The curves at $pO_{2,cat} \in \{0.02, 0.01\}$ atm are now in good agreement. However, the empirical approach looses validity for higher values of $pO_{2,cat} \geq 0.04$ atm, where a better agreement is observed when applying the original model (developed in chapter 4.3.1) (see results in Fig. 50).
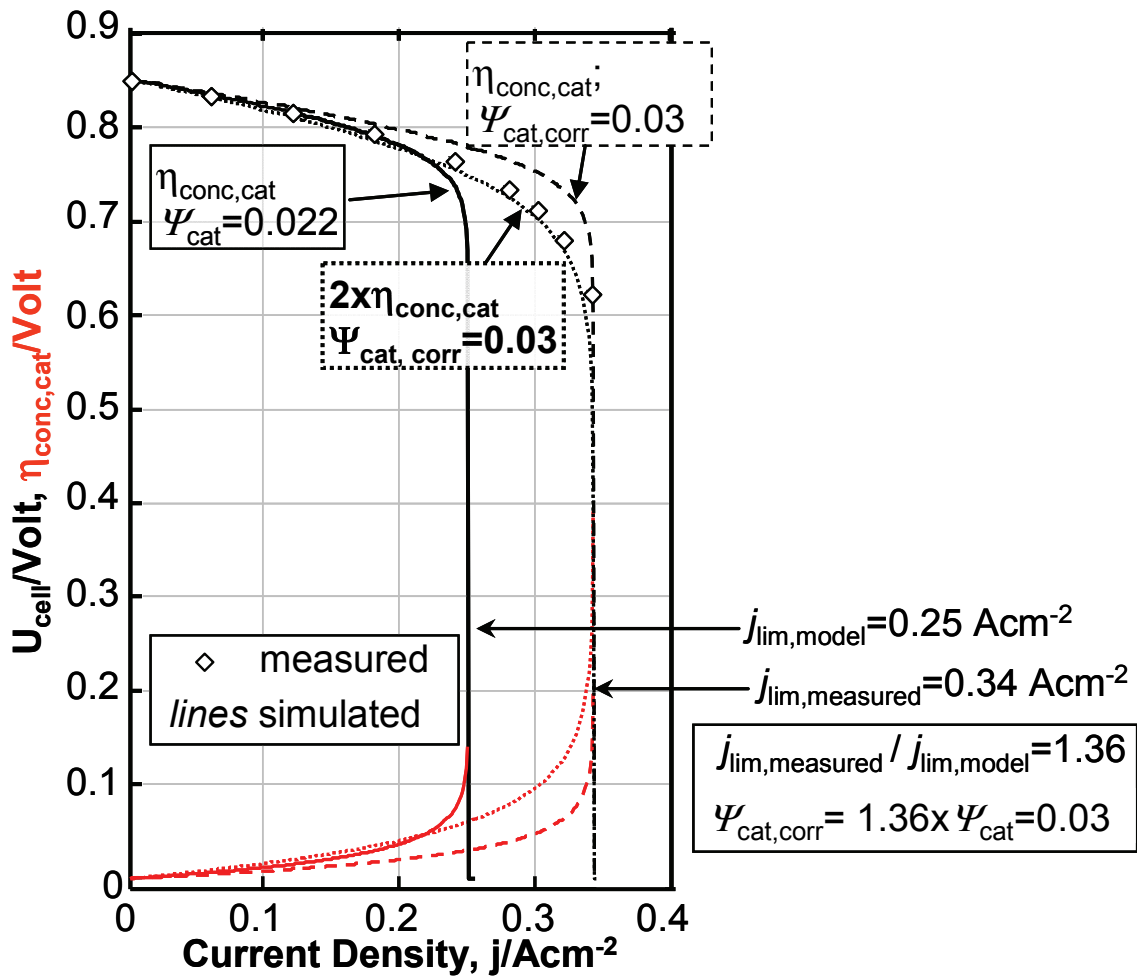
Fig. 51: Simulated [with the model presented in chapter 4.3.1 as well as the modelling parameters from Table 12 (continuous line); with corrected $\psi_{cat,corr}$ = 0.03 (dash dotted line); with $\psi_{cat,corr}$ = 0.03 and $\eta_{conc,cat,corr}$ = 2·$\eta_{conc,cat}$ (dotted line)] and measured (symbols) I-U curves at $pO_{2,cat}$ = 0.01 atm, $pH_{2,an}$ = 0.40 atm, pH_2O_{an} = 0.60 atm and T = 800 °C [cell# Z1_188].
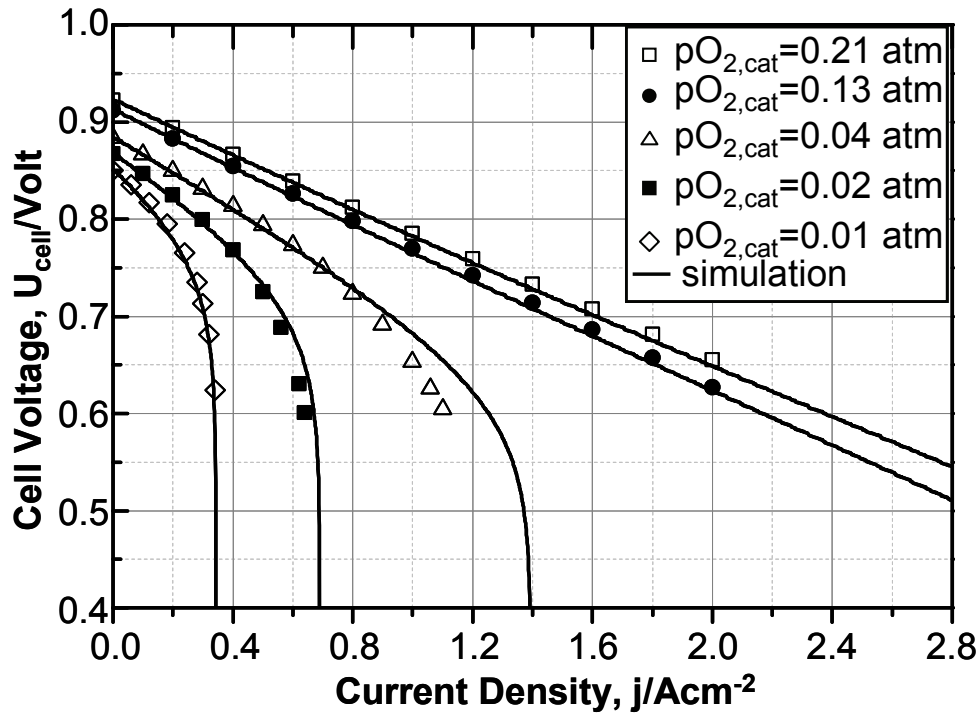
Fig. 52: Simulated (with the model presented in chapter 4.3.1 as well as the modelling parameters from Table 12, with the exception of $\psi_{cat,corr}$ = 0.03 and $\eta_{conc,cat,corr}$ = 2·$\eta_{conc,cat}$; lines) and measured (symbols) I-U curves. For all curves shown in this Figure $pH_{2,an}$ = 0.40 atm, pH_2O_{an} = 0.60 atm and T = 800 °C were set constant.

<u>Diffusion Overpotential at the Anode</u>

The validation of the model for a variation of the gas composition at the anode follows the same procedure as in the case of the cathode. Fig. 53 shows the simulation results for different hydrogen and water partial pressures ($pH_{2,an}$ = 0.08…0.3 atm, pH_2O_{an} = 0.17…0.19 atm, balance N$_2$) at a constant temperature (T = 800 °C) and oxygen partial pressure at the cathode ($pO_{2,cat}$ = 0.21 atm (air)). Low hydrogen partial pressures were approached appositely to validate the model within the diffusion limitation regime of the I-U characteristics.

For the cell type investigated, gas diffusion polarisation at the anode becomes predominant only at very low hydrogen partial pressures $pH_{2,an}$ < 0.2 atm and for current densities j > 2 A/cm². A comparison between simulated and measured I-U curves at $pH_{2,an}$ = 0.08 atm and pH_2O_{an} = 0.17 atm (balance nitrogen) clearly shows that the diffusion overpotential at the anode predicted by the model is sufficiently precise. Therefore, the structural parameter ψ_{an} of the anode has obviously been correctly determined.
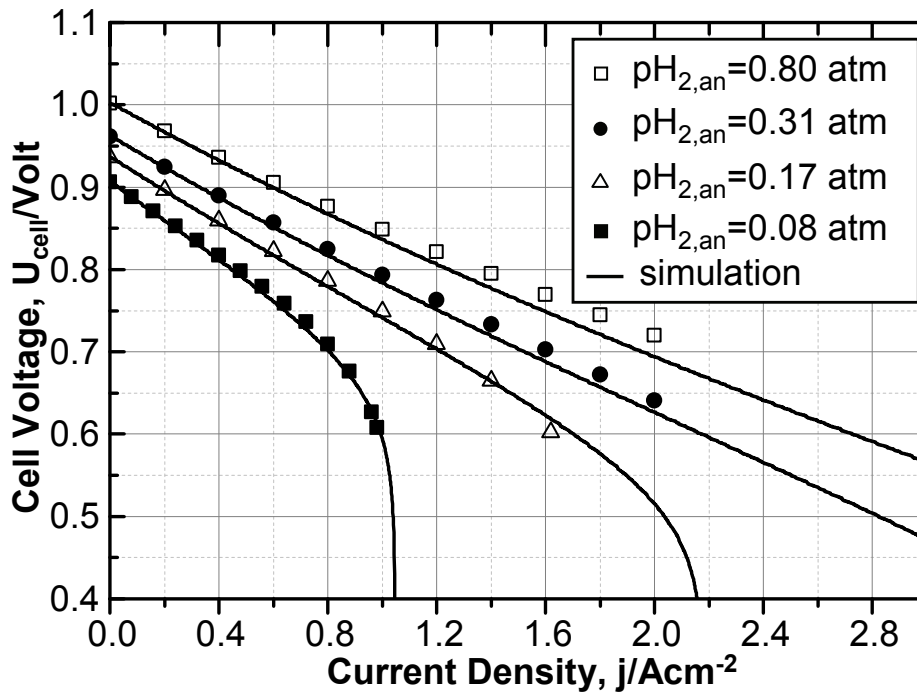
Fig. 53: Simulated (with the model presented in chapter 4.3.1 as well as the modelling parameters from Table 12; lines) and measured (symbols) I-U curves at four different hydrogen and water partial pressures at the anode ($pH_{2,an};pH_2O_{an}$) = [(0.08;0.17), (0.17;0.18), (0.31;0.19), (0.80;0.20)] atm, balance N$_2$) and constant $pO_{2,cat}$ = 0.21 atm (air), and T = 800 °C [cell# Z1_188].

Activation Overpotential

The predicted activation overpotential at the anode was examined by varying the anodic gas compositions $pH_{2,an} \in$ {0.904, 0.856, 0.6, 0.4} atm and $pH_2O_{an} \in$ {0.096, 0.144, 0.4, 0.6} atm for the simulations, thereby keeping $pO_{2,cat}$ = 0.21 atm (air) at the cathode and the temperature (T = 800 °C) constant. First of all, Fig. 54a shows simulation results predicting the activation overpotential at the anode for both models from literature that use estimated values for the parameters a = 1 and b = 1 [75, 77, 80] as well as a = 1 and b = -0.5 [82]. However, neither of the two simulations is in good agreement with the experimental data for the operating points under consideration. Even an appraisal as to which approach leads to a better agreement with the experimental data, as done by Costamagna et al. [84], seems rather difficult. Hence, the parameters a and b had to be determined separately following the procedure described above (see chapter 4.3.1 "Model Description and Parameter Identification"). Evaluation of the impedance measurements already showed that the value of a must be considerably smaller than the value used so far (a = 1). As already specified in Table 12, the values determined separately within this study were a = -0.1 and b = 0.33.

Fig. 54b compares the results from simulations using the models from literature cited above (with a = 1, b = 1, and a = 1, b = -0.5, respectively) with the new simulations using a = -0.1

and $b = 0.33$. The new ansatz presented in this work, with separately determined parameters, clearly yields the best agreement with the measured data.

In the following, the activation overpotential at the cathode is calculated for arbitrarily chosen parameters $m = 1$ and $m = 0.5$ as well as for the value $m = 0.22$ determined in this study. Fig. 55 presents simulated I-U curves at the operating conditions $T = 721\,°C$, $pH_{2,an} = 0.8$ atm, $pH_2O_{an} = 0.2$ atm, and $pO_{2,cat} = 0.21$ atm. The best agreement with the measured data is achieved by the simulation using $m = 0.22$. This value is close to the one ($m = 0.25$) frequently reported in literature [42, 76, 77, 80, 81, 83, 104]. This value confirms the assumption that adsorption and surface exchange constitute the rate-determining step during reduction of O_2 to O^{2-} and subsequent incorporation of the ions into the cathode material [42, 115]. By comparing the simulated curves (Fig. 55) for different parameters m, it can be concluded that values of $m \in [0.15\ 0.5]$ have little influence at low current densities ($j < 0.3$ A/cm^2).

(a)

(b)
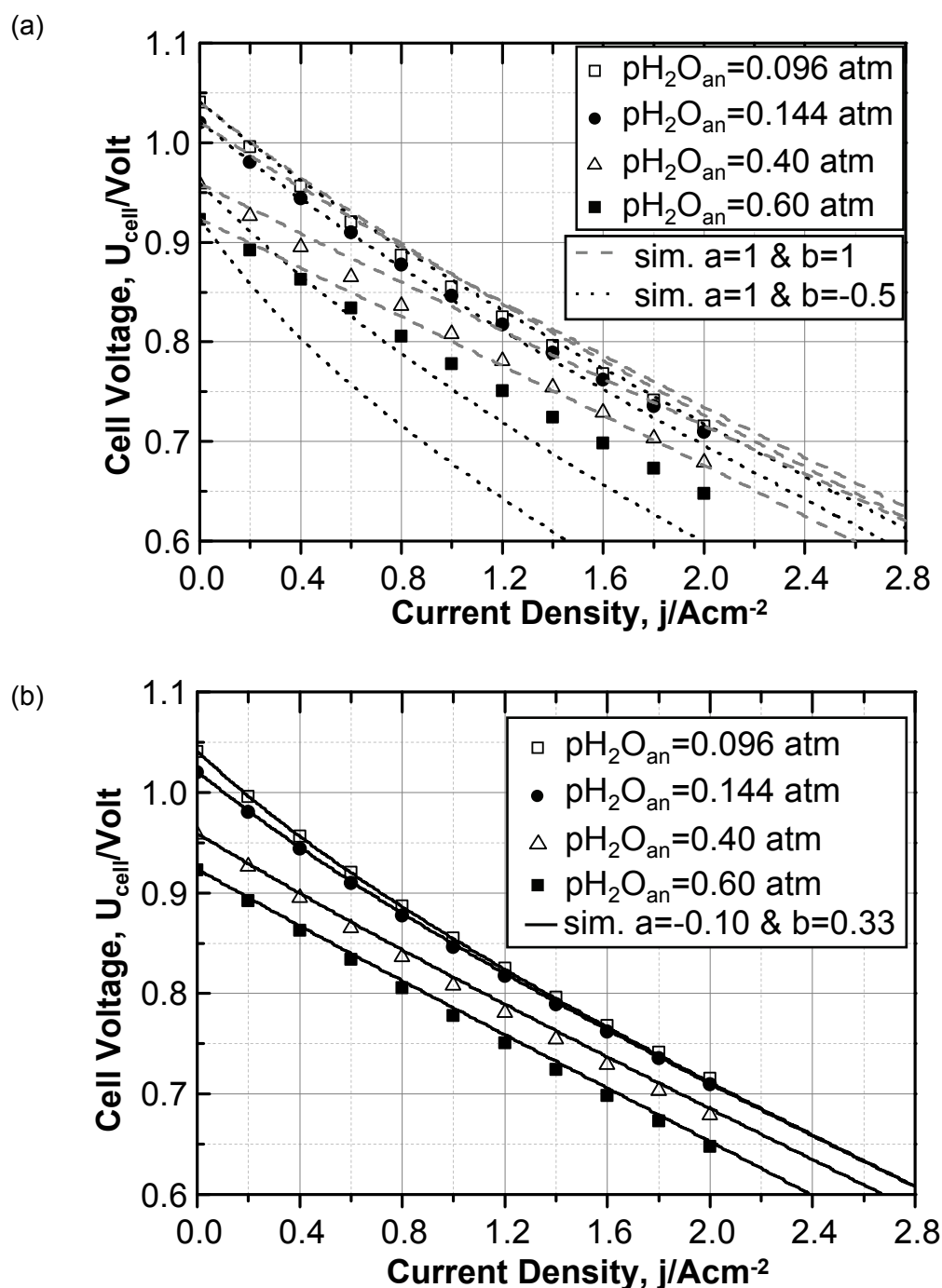
Fig. 54: (a) Simulated (lines; with the model presented in chapter 4.3.1 as well as the modelling parameters $a = 1$ & $b = 1$ (according to [75, 77, 80]) and $a = 1$ & $b = -0.5$ (according to [82]), respectively; all the other parameters taken from Table 12) and measured (symbols) I-U curves for four different humidifications at the anode (pH_2O_{an} = 0.096, 0.144, 0.40, 0.60 atm, balance H_2) and constant $pO_{2,cat}$ = 0.21 atm (air) and T = 800 °C. (b) Simulated (lines; with the model presented in chapter 4.3.1 as well as the modelling parameters from Table 12) and measured (symbols) I-U curves for four different humidifications at the anode (pH_2O_{an} = 0.096, 0.144, 0.40, 0.60 atm) and constant $pO_{2,cat}$ = 0.21 atm (air) and T = 800 °C [cell# Z1_188].
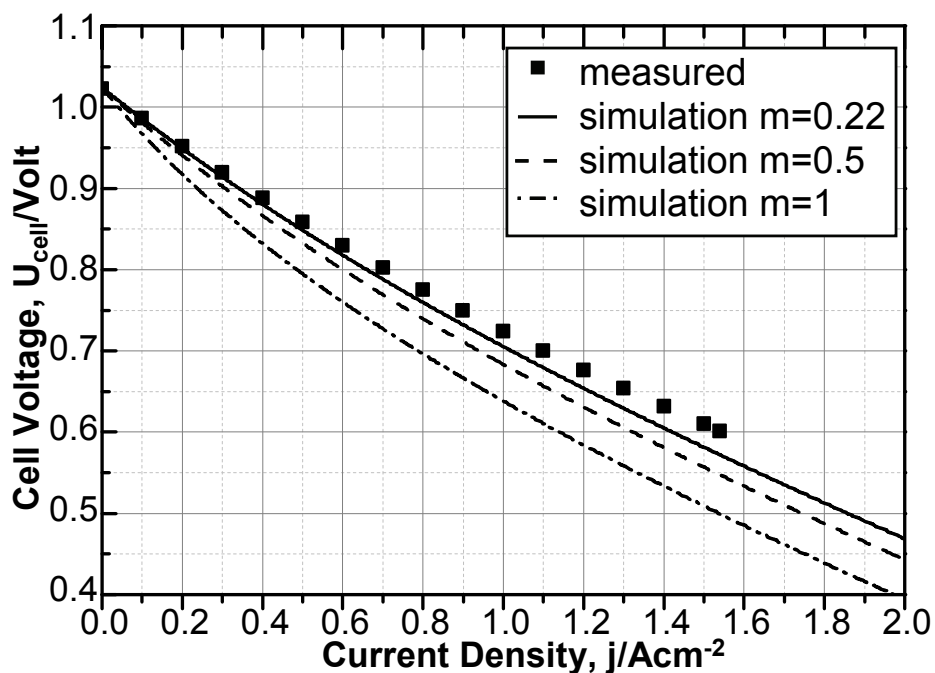
Fig. 55: Simulated (lines; with the model presented in chapter 4.3.1 as well as the modelling parameters from Table 12, with the exception of the parameter *m*) and measured (symbols) I-U curves for *T* = 721 °C, *pH*$_{2,an}$ = 0.80 atm, *pH*$_2$*O*$_{an}$ = 0.20 atm, and *pO*$_{2,cat}$ = 0.21 atm. The solid line marks the model prediction for *m* = 0.22, the dashed line for *m* = 0.5, and the dot and dash line for *m* = 1 [cell# Z1_188].

4.4 Further Applications

4.4.1 Electrochemical Model for SOFC-Stacks

In a recent paper Klotz et al. [116] (IWE) presented an electrochemical 1-D stack plane model consisting of a stationary and a dynamic part. The prerequisite was the equivalent circuit model (ECM) developed and presented in this thesis (Fig. 26). The stack was discretised along the length of the gas channel and the ECM was assigned to each single discrete element (cf. Fig. 56).
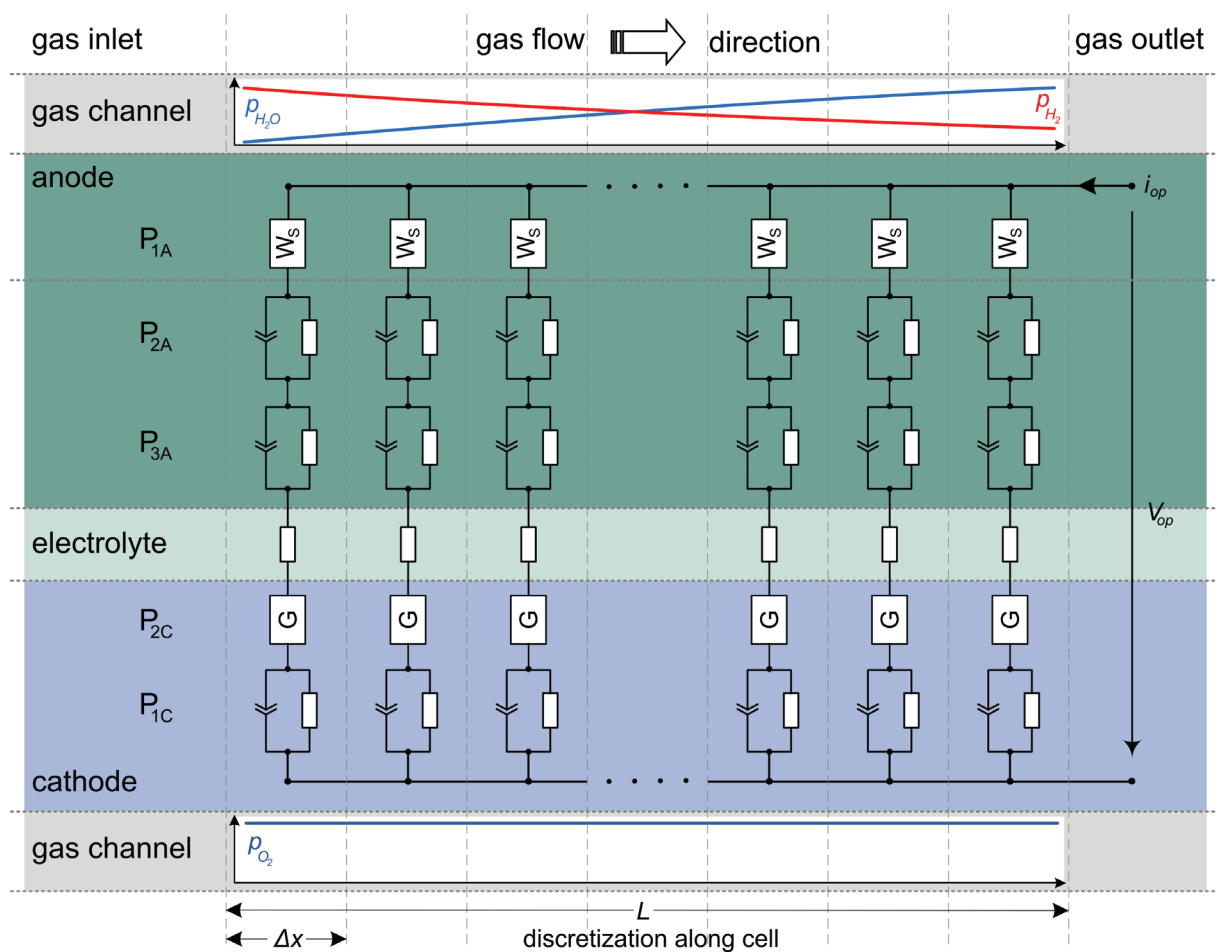
Fig. 56: Loss separation on the stack level: Scheme of the 1-D model discretised along the gas channel with an equivalent circuit for every element [116].

In this way the loss contributions of (i) ohmic resistance (R_0), (ii) gas phase polarisation within the anode substrate (P_{1A}), (iii) electrochemistry in the anode functional layer ($P_{2A}+P_{3A}$) and (iv) oxygen reduction reaction at the cathode (P_{2C}) could be simulated (i. e. separated) as a function of operating voltage and fuel gas composition along the gas channel. Finally, the power loss density per unit area $P_{loss,PX}$ (x)/dA caused by each single polarisation process

(index PX=P1A, P2A…) could be evaluated as a function of flow channel position (x) (Fig. 57a-d). The resulting simulations give essential information to what extend the polarisation processes (P_{1A}, P_{2A}, P_{3A}, P_{1C}, P_{2C}) participate to the overall power loss in a stack. This knowledge is of crucial importance for a targeted cell and system-development.
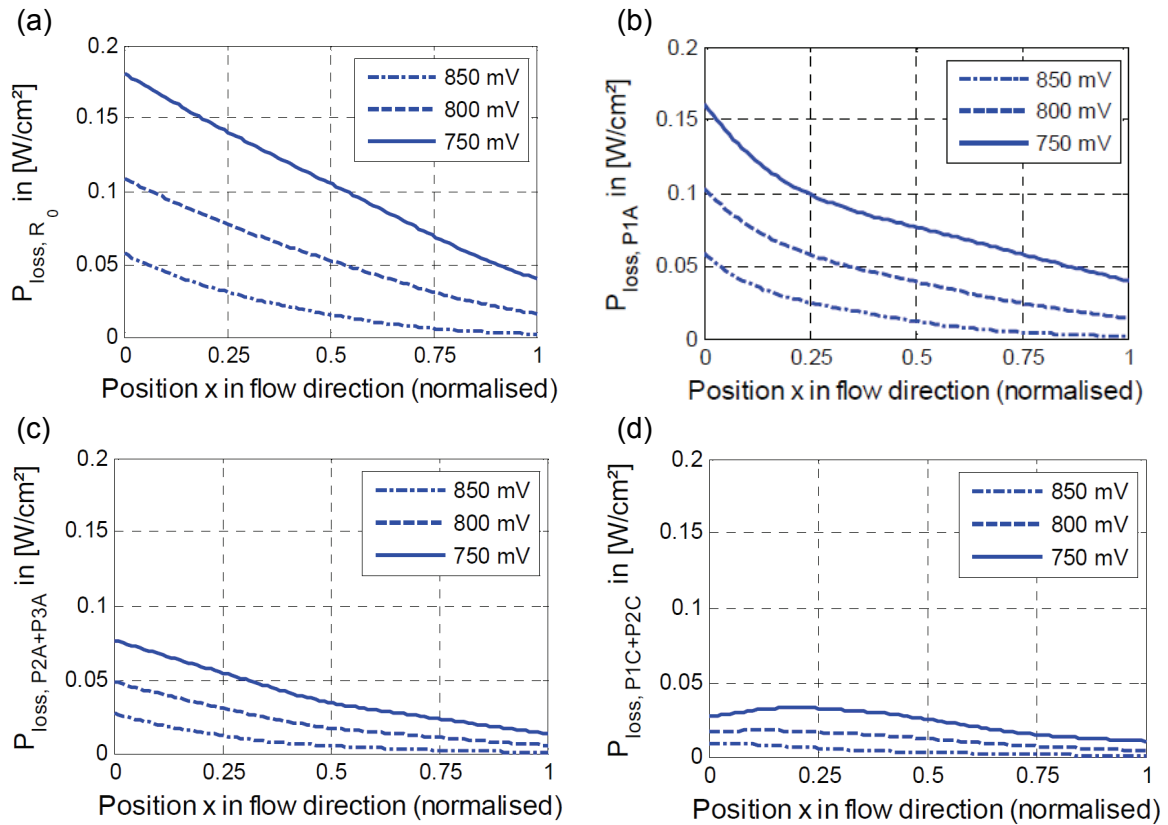
Fig. 57: **Calculated power loss distributions per unit area for the circuit elements at different operating voltages (800 °C): (a) Power loss caused by the ohmic resistance (R_0). (b) power loss caused by gas diffusion in the anode substrate (R_{1A}), (c) power loss caused by activation polarisation in the anode functional layer ($R_{2A}+R_{3A}$), (d) power losses caused by the cathode ($R_{1C}+R_{2C}$); as cathode losses are very low compared to the other losses the losses of the two processes P_{1C} and P_{2C} were summed up for this diagram) [116].**

4.4.2 Degradation Analysis

A detailed understanding of degradation phenomena taking place at cell level is essential for a profound improvement of intermediate temperature SOFCs. In a recent paper published by Endler et al. (IWE) [67] the ECM presented in this thesis has been applied successfully to evaluate degradation effects in anode supported single cells. The aforementioned paper presents the time dependent change of each single polarisation loss contribution at a level of detail never presented before. In Fig. 58 the essential findings are shown. As can be seen, the resistance R_{2C} is identified as the main cause for the performance loss of state-of-the-art IT-SOFCs if a MIEC cathode material such as $La_{0.58}Sr_{0.4}Co_{0.2}Fe_{0.8}O_{3-\delta}$ is chosen. The authors

ascribe the pronounced increase in R_{2C} to the slow depletion of Sr from the surface of the LSCF-particles with operation time [117, 118].
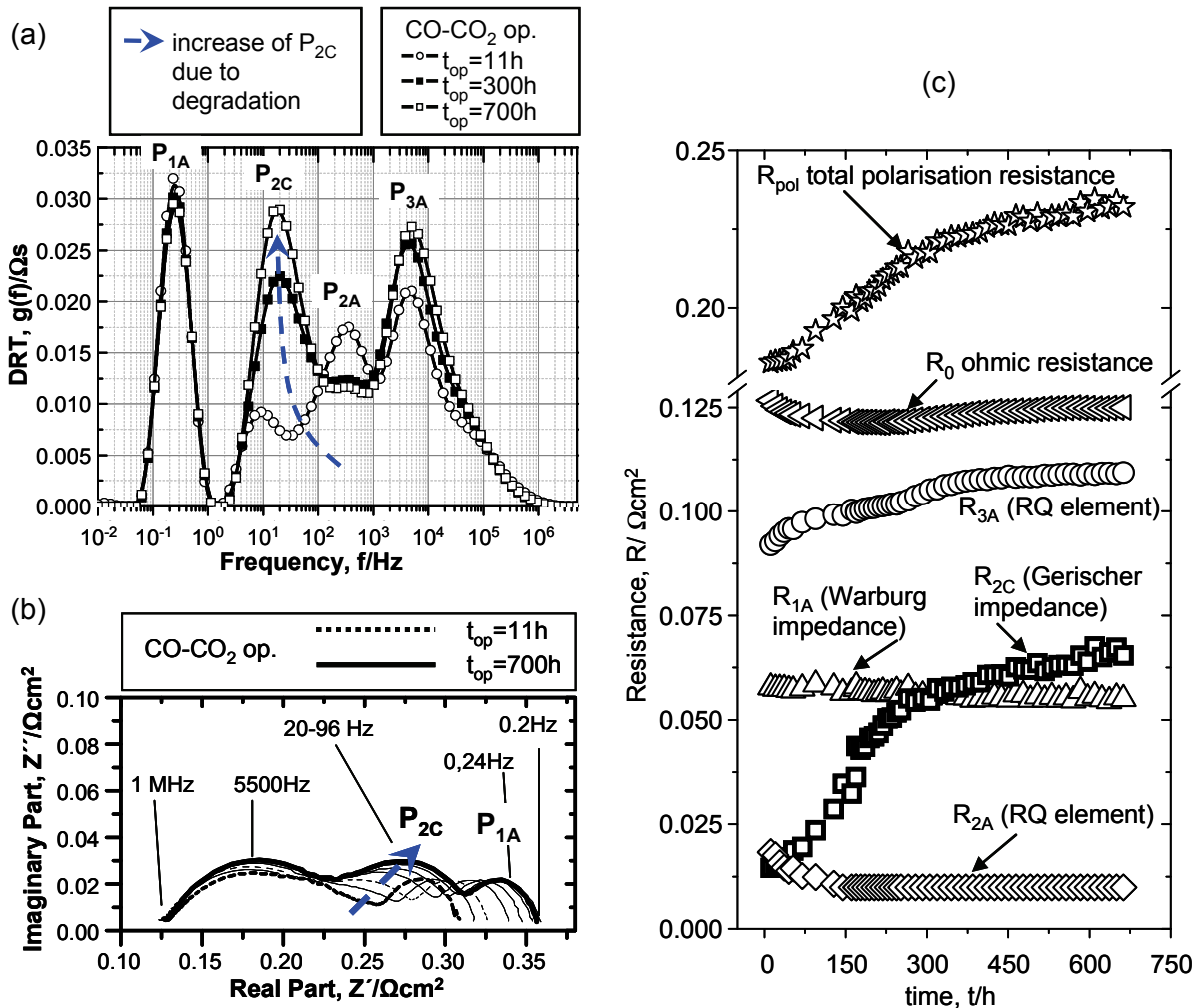
Fig. 58: (a) Series of DRT curves for the CO–CO₂ operation (circle and square DRTs, t = 11, 300, and 700 h) showing the increase in cathode impedance P_{2C} with time. (b) Impedance spectra of an ASC recorded each 100 h at T = 750°C applying a CO–CO₂ gas mixture at the anode. A third semicircle at 20…96 Hz (associated with P_{2C}) becomes evident with time. (c) Characteristic time dependence of the ohmic and polarisation resistances obtained by the CNLS fit of the impedance spectra to the equivalent circuit developed in this thesis (cf. Fig. 26) [67].

5 Summary

Interest in solid oxide fuel cells (SOFC), which combine potentially efficient energy production with flexible fuel composition, has significantly increased in the past few years. Amongst the most important development goals is, besides long-term stability, the single-cell performance which is limited by three loss mechanisms: (i) ohmic losses, (ii) polarisation losses through gas diffusion, and (iii) losses by activation polarisation.

However, to this day the progress for a further improvement of anode supported cells has been partly constrained by an incomplete understanding of the physical origin and share of the individual polarisation processes controlling the cell performance.

Therefore, the main goal of this work was the identification and physical interpretation of the polarisation processes occurring in an anode supported cell.

Equivalent Circuit Development

A high resolution electrochemical impedance spectroscopy study on anode supported single cells (ASC) with thin electrolytes (< 20 µm) was presented. The cells were characterised at OCV over a broad range of operating conditions, including different temperatures and various cathode and anode gas compositions. By calculating the distribution of relaxation times (DRT) up to five different processes contributing to the total polarisation loss of a complete anode supported cell could be identified. The high resolution of the DRT combined with the numeric accuracy of the CNLS fit enabled the identification of oxygen surface exchange kinetics, diffusivity of oxygen ions in the bulk and gas phase diffusion in the mixed conducting LSCF cathode. At the anode side three limiting processes were identified. One process is attributed to the gas diffusion within the anode substrate, whereas the other two are related to gas diffusion coupled with charge transfer reaction and ionic transport in the Ni/YSZ anode functional layer structure.

Evaluation of Oxygen Exchange and Diffusion Coefficients

The equivalent circuit model developed in this work has been applied for assessing the performance of mixed electronic ionic conducting (MIEC) cathode materials. It could be shown that the chemical surface and diffusion coefficients (k^δ and D^δ) of MIEC cathode materials can be obtained directly from impedance data measured on ASC cells. As a prerequisite, the Gerischer-type impedance contribution of the cathode was identified by applying the combined DRT and equivalent circuit fitting approach presented in chapter 4.1. In this way, the area specific resistance and the characteristic time constant (R_{chem} and t_{chem}), related to the thermodynamic, surface kinetic and transport properties of the MIEC cathode

could be determined. k^δ and D^δ were calculated from R_{chem} and t_{chem} based on essential structural and compositional parameters (ε, a_S, τ_s, c_O, c_{mc}) and the thermodynamic enhancement factor γ_{TD}.

The uncertainties in k^δ are mainly caused by the variation range of the electrochemical active surface area (a_S). However, recent work on SOFC electrode microstructure modelling, based on high-resolution FIB/SEM data, e.g. by [12, 13, 26, 27], strongly suggests that in the near future structural parameters of "real" electrodes will become more readily accessible. On the other side, the error range of D^δ is mainly caused by the thermodynamic enhancement factor γ_{TD}.

In this work, the developed method is applied on two alternative cathode material compositions (L68SCF: La-rich, and LSF: without Co). The results are compared to the state-of-the-art $La_{0.58}Sr_{0.4}Co_{0.2}Fe_{0.8}O_{3-\delta}$ (L58SCF) cathode, which shows a strong increase of the polarisation resistance at 750 °C by up to 310 % within 700 hrs [67].

The obtained results confirm the lowest ASR for the unaged state-of-the-art L58SCF cathode when compared to the two proposed alternatives. However, after 700h of operation the ASR value of L58SCF is a factor of 2 larger than the unaged LSF. In contrary, the ASR value of L68SCF is about 30% larger when compared to the aged L58SCF.

Hence, the LSF composition could represent a potential cathode for intermediate temperature SOFC (IT-SOFC). However, only future long term studies on LSF will allow a conclusive statement.

The evaluation of the surface exchange coefficient (k^δ) and bulk diffusion coefficient (D^δ) of the analysed cathodes showed the following:

1. The strong degradation of the L58SCF cathode is mainly caused by the strong decrease of D^δ (almost 1 order of magnitude).

2. The relatively high activation energies of the ASRs determined for LSF (1.8 eV) and L68SCF (1.69 eV) are caused by the extraordinary high activation energies (> 2.46 eV) of the bulk diffusion coefficients D^δ.

3. The initially lower performance of LSF and L68SCF compared to the L58SCF cathode is mainly attributed to their lower bulk diffusion coefficient.

Furthermore, this approach also holds potential to disclose degradation phenomena correlated to microstructural changes and/or compositional changes evaluated on "real" cathodes, not on bulk samples.

Modelling of the Current Voltage Characteristics

A zero-dimensional stationary model for the prediction of current-voltage characteristics of anode-supported cells for intermediate temperature SOFC has been developed. Simulation results were validated with experimental data determined in the temperature range from 621°C to 821°C, current densities up to 2 A/cm^2 and cell voltages not below a limit of 0.6 V. The model includes the Butler-Volmer equation for the determination of activation polarisation, Fick's model for describing the diffusion polarisation, and, lastly, Ohm's law for calculating the ohmic overpotential. The necessary modelling parameters (with the exception of the charge transfer coefficients α_{an} and α_{cat}) were obtained from impedance measurements under open-circuit conditions, thereby specifically varying the operating conditions (gas compositions and temperature).

The measured impedance curves were fitted by means of the detailed equivalent-circuit model developed in this work (chapter 4.1). Using the resistances obtained in this way, the partial pressure and temperature dependencies of the cathodic and anodic exchange current density could be determined by fitting semi-empirical modelling equations (power law ansatz). The parameters a and b, representing the exponents of the dependency of the anodic exchange current density on the partial pressures of H_2 and H_2O, respectively, could be determined independently of each other for the first time. In the same way, the parameter m, the exponent of the oxygen partial pressure dependency of the cathodic exchange current density, could be obtained. The charge transfer coefficients were determined differently by impedance measurements under load and subsequent fitting of the Butler-Volmer equation to the resulting current-dependent activation overpotentials. By using the parameters a, b, and m ($a = -0.10$, $b = 0.33$, $m = 0.22$), α_{an} and α_{cat} ($\alpha_{an} = 0.590$, $\alpha_{cat} = 0.650$) as well as the temperature-dependent prefactors γ_{an} and γ_{cat} ($\gamma_{an} = 1.82527 \cdot 10^6 \cdot T$ A/m^2, $\gamma_{cat} = 1.51556 \cdot 10^8 \cdot T$ A/m^2) the model facilitates a better predictability of the activation polarisation over a wide range of temperature and gas composition. Within the temperature range investigated (621-821 °C) and for all current densities, the deviation Δ between simulated I-U curves and measured data lies within a range of 0.01 % $\leq \Delta \leq$ 4.75 %.

Contrary to other common modelling approaches, a separate treatment of each single loss mechanism (diffusive or electrochemical losses at the anode/cathode, or ohmic losses) is rendered possible throughout the whole current range without the necessity of having too grossly estimate parameters. This facilitates an assessment of the optimization potential of a cell at any arbitrary operating point, or a comparison between different cells at a given operating point. The identified parameters (listed in Table 12) and the modelling equations support future SOFC system modelling.

However, the model only yields precise results assuming a spatially constant current density and temperature distribution throughout the active electrode area which requires cells with a sufficiently small cross-sectional area (1 cm² electrodes in our case). According to our

experience so far, a total number of approximately 25 impedance measurements, thereby varying the operating parameters temperature and fuel composition, are necessary to determine the modelling parameters for a reliable prediction.

In a next step, the model is to be applied to reformate conditions; to this end, a series of impedance measurements with CO/CO_2 and H_2/H_2O are in preparation. Moreover, in the future the model shall be employed for the prediction of the performance of larger single cells (stack-„repeating units"). For this purpose, it has to be expanded into a two-dimensional model in order to consider a spatially resolved current density and the resulting in-plane temperature distribution of the cell.

6 Appendix

6.1 Variation of Anode Functional Layer Thickness

High performance anode-supported solid oxide fuel cells (SOFC) with MIEC cathodes (Ni/8YSZ anode; $La_{0.58}Sr_{0.4}Co_{0.2}Fe_{0.8}O_{3-\delta}$ cathode; 8YSZ electrolyte; area = 1 cm²) have been evaluated with respect to the anode functional layer thickness by means of impedance spectroscopy and current voltage characteristic.

The SOFC single cells analysed are based on 50 x 50 mm² anode substrates (Ni/8YSZ) with an average thickness of about 1.5 mm. On these substrates, an anode functional layer (AFL) (Ni/8YSZ) with a variable thickness ranging from 1 to 22 μm and an electrolyte (8YSZ, approx. 10 μm) are deposited and co-fired at 1400 °C.

The cathode (approx. 45 μm thick, active area 10 x 10 mm^2) was made of L58SCF ($La_{0.58}Sr_{0.4}Co_{0.2}Fe_{0.8}O_{3-\delta}$). The formation of insulating secondary phases (lanthanum and strontium zirconates) at the LSCF cathode /electrolyte interface was prevented by a screen-printed ceria (CGO: $Ce_{0.8}Gd_{0.2}O_{2-\delta}$) interlayer (cf. chapter 3 of this thesis).

The dependence of the power output density (at 0.8 V) on the anode functional layer thickness (t_{AFL}) is shown in Fig. 59. When disregarding the points at 3 und 5 micrometers a clear trend is visible (cp. line connected points), i.e. the power density decreases by increasing AFL thickness. As we will see later this trend is more or less distorted by unwanted inhomogeneities in the (nominally identical) anode substrates causing a large scatter on the anode gas diffusion polarisation within the analysed samples. Especially the 3, 5 and 22 μm AFL samples show an increased gas diffusion limitation in the substrate, which explains their discrepancy from the above mentioned general trend. It is worth mentioning that the 22 μm sample is less affected by that circumstance because of its higher overall polarisation resistance.
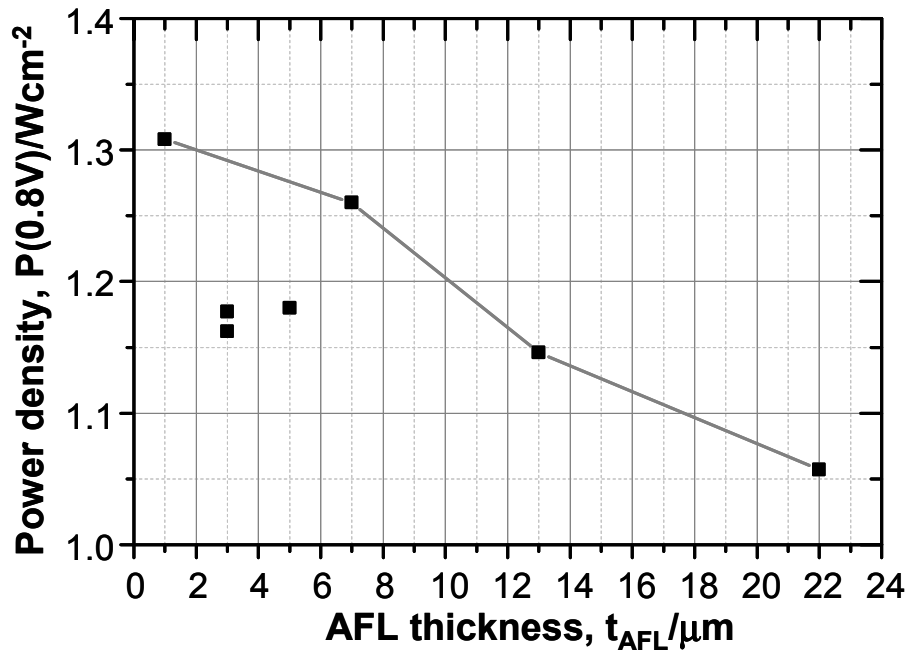
Fig. 59: Dependency of the power output density on the anode functional layer thickness t_{AFL}. The power output increases by decreasing t_{AFL} (line connected points). The values between 3 and 5 µm deviate from the general trend, [T = 800 °C; pH_2O_{an} = 0.055 atm in hydrogen; cathode gas: air].

In Fig. 60 the effect of the AFL extension on the distribution of relaxation times is shown. As can be clearly seen the AFL thickness affects strongly the polarisation contribution caused by P_{2A} whereas P_{3A} shows no mentionable change.

Due to the fact that all cells analysed within this study had a nominally identical anode substrate, no dependence of the gas diffusion polarisation process P_{1A} on the AFL extension was expected. Although Fig. 60 shows a big scatter of the (first) peak related to P_{1A}. This is most probably related to inhomogeneities in the microstructure of the anode substrates caused by the manufacturing procedure.
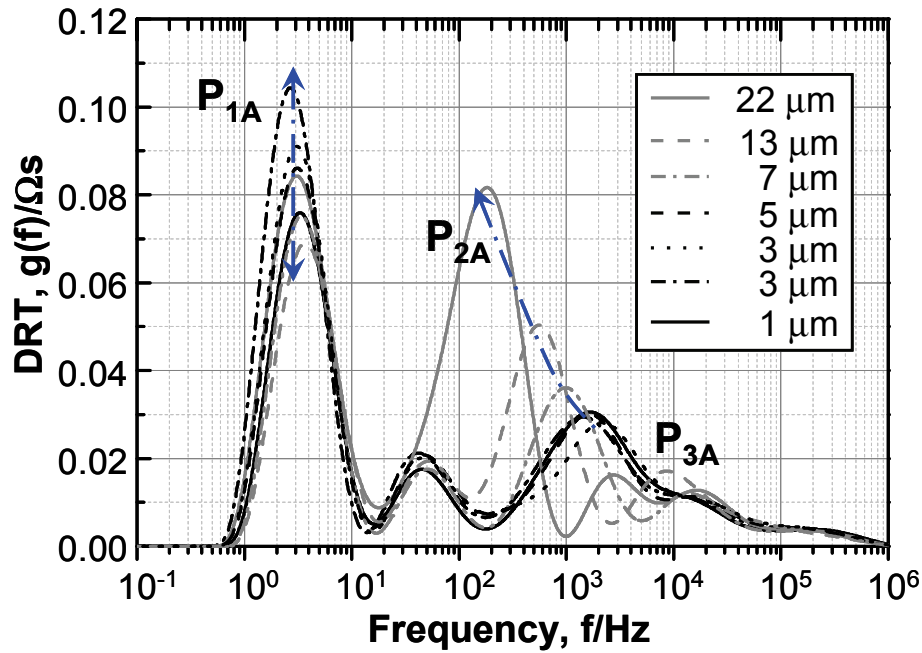
Fig. 60: Series of DRTs for different AFL thicknesses. Process P_{2A} shows a distinctive dependency on the AFL extension. The large scatter of P_{1A} is caused by microstructural inhomogeneities of the anode substrate, [$T = 800\ °C$; $pH_2O_{an} = 0.055$ atm in hydrogen; cathode gas: air].

The quantitative dependence of the anodic polarisation contributions and the ohmic resistance R_0 on the AFL thickness is depicted in Fig. 61. These values were obtained by a CNLS fit of the equivalent circuit developed in this thesis and shown in Fig. 26 before. The overall anode polarisation at 5.5 % fuel utilization is dominated by the gas phase diffusion resistance R_{1A}, which exhibits a large scatter but no dependency on the AFL extension. In the same graph the sum of R_{2A} and R_{3A} is shown. The dependence of the summarised polarisation resistance $R_{2A}+R_{3A}$ on the AFL thickness shows two distinctive ranges. For values between 22 and 7 μm the increase of $R_{2A}+R_{3A}$ is proportional to the increase of the AFL thickness, whereas in the range between 8 and 1 μm no mentionable dependence is noticeable. This behaviour can be explained by the fact that with increasing AFL thickness the gas diffusion inside the pores of the AFL becomes the dominant limiting factor. This is in accordance with the expectation of a linear increase of the diffusion resistance with increasing diffusion length, i.e. AFL thickness. On the other side, in the range between 1 and 7 μm the resistance is controlled by the charge transfer reaction at the triple phase boundary and the ionic transport in the Ni/YSZ structure. Concerning the ohmic resistance R_0, no dependency on the AFL extension is found.
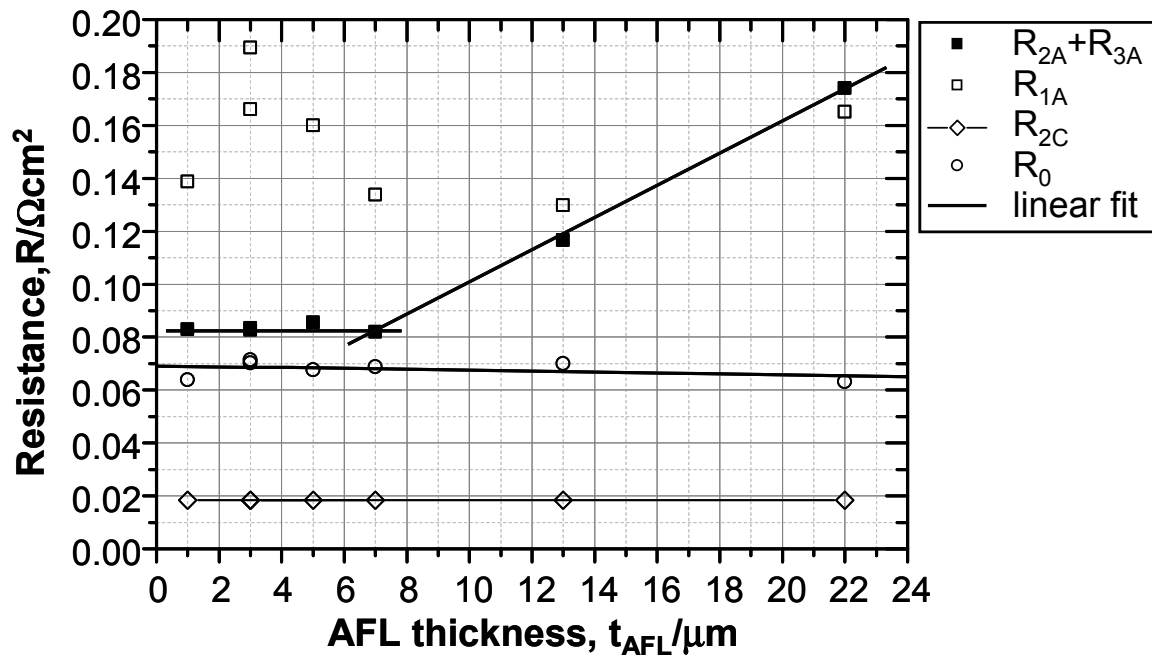
Fig. 61: Dependency of each single polarisation contribution on the AFL thickness. The cathodic polarisation resistance R_{2C} has been fixed to a value of 18 mΩcm^2, [T = 800 °C; pH_2O_{an} = 0.055 atm in hydrogen; cathode gas: air].

Conclusions

High performance anode-supported solid oxide fuel cells (SOFC) with varied anode functional layer (AFL) thickness have been evaluated by means of impedance spectroscopy and current voltage characteristics.

The AFL extension shows a pronounced effect on the area specific power output density. When decreasing the AFL thickness from 22 to 1 μm an increase of about 20 % in the power output is measured.

Extensive impedance spectroscopy measurements in combination with a high-resolution calculation of the distribution of relaxation times (DRT) enabled the identification of a gas diffusion limitation inside the pores of the AFL as an additional performance limiting factor. An increase of the AFL thickness leads to an increased effective diffusion length of the molecules inside the AFL, thus enlarging the polarisation loss caused by the gaseous mass transport. However, this limitation can be neglected for cells with an AFL thickness t_{AFL} < 8 μm (i.e. for the FZJ state-of-the-art cell with a nominal t_{AFL} = 7 μm).

6.2 List of Samples

Cell#	FZJ ID#	Description	Comment (varied cell part)
Z1_153	FZJ ASC 3809	state-of-the-art FZJ ASC	
Z1_154	FZJ ASC 7719	state-of-the-art FZJ ASC	
Z1_157	FZJ ASC PS26/9100	PSE cathode PS26	$La_{0.68}Sr_{0.3}Ru_{0.2}Fe_{0.8}O_{3-\delta}$ cathode
Z1_158	FZJ ASC PS01/9106	L68SCF cathode PS01	$La_{0.68}Sr_{0.3}Co_{0.2}Fe_{0.8}O_{3-\delta}$ cathode
Z1_159	FZJ ASC 4901	state-of-the-art FZJ ASC	
Z1_160	FZJ ASC PS24/9070	L68SF cathode PS24	$La_{0.68}Sr_{0.3}FeO_{3-\delta}$ cathode
Z1_161	FZJ ASC PS07/9087	PSE cathode PS07	$La_{0.68}Sr_{0.3}Cu_{0.2}Fe_{0.8}O_{3-\delta}$ cathode
Z1_164	FZJ ASC PS13/9080	PSE cathode PS13	$La_{0.68}Sr_{0.3}Mg_{0.2}Fe_{0.8}O_{3-\delta}$ cathode
Z1_166	FZJ ASC 9104	L68SCF cathode PS01/9104	$La_{0.68}Sr_{0.3}Co_{0.2}Fe_{0.8}O_{3-\delta}$ cathode
Z1_177	FZJ ASC 7906/3	state-of-the-art FZJ ASC	
Z1_178	FZJ ASC 7905/16	varied anode functional layer	AFL thickness = 13µm
Z1_179	FZJ ASC 9964	varied anode functional layer	AFL thickness = 1µm
Z1_180	FZJ ASC 9425	varied anode functional layer	AFL thickness = 3µm
Z1_181	FZJ ASC 10516	state-of-the-art FZJ ASC	
Z1_182	FZJ ASC 7904/2	varied anode functional layer	AFL thickness = 18µm
Z1_183	FZJ ASC 9445	varied anode functional layer	AFL thickness = 5µm
Z1_184	FZJ ASC 9426	varied anode functional layer	AFL thickness = 3µm
Z1_185	FZJ ASC 7903/9	varied anode functional layer	AFL thickness = 22µm
Z1_186	FZJ ASC 11034	state-of-the-art FZJ ASC	
Z1_187	FZJ ASC 7906/13	state-of-the-art FZJ ASC	
Z1_188	FZJ ASC 10539	state-of-the-art FZJ ASC	
Z2_144	FZJ ASC 5770	state-of-the-art FZJ ASC	
Z2_157	FZJ ASC 10537	state-of-the-art FZJ ASC	
Z2_158	FZJ ASC 10525	state-of-the-art FZJ ASC	
Z2_164	FZJ ASC 10524	state-of-the-art FZJ ASC	
Z2_165	FZJ ASC 10523	state-of-the-art FZJ ASC	
Z2_166	FZJ ASC 10477	state-of-the-art FZJ ASC	
Z2_168	FZJ ASC 10515	state-of-the-art FZJ ASC	
Z2_170	FZJ ASC 10633/1	PSCF-cathode	$Pr_{0.58}Sr_{0.4}Co_{0.2}Fe_{0.8}O_{3-\delta}$ cathode
Z2_174	FZJ ASC 10529	state-of-the-art FZJ ASC	
Z2_177	FZJ ASC 12044-1	tapecasted anode substrate	500µm anode substrate & LSM/YSZ cathode
Z2_178	FZJ ASC SE-RC-6F-FG2-LB-3-2	tapecasted anode substrate	500µm anode substrate & LSM/YSZ cathode
Z2_179	FZJ ASC SE-RC-1-2	tapecasted anode substrate	500µm anode substrate & LSM/YSZ cathode
Z2_180	FZJ ASC SFE-RC-NZ-6-1	tapecasted anode substrate	500µm anode substrate & LSM/YSZ cathode
Z2_181	FZJ ASC 10510	state-of-the-art FZJ ASC	
Z2_184	FZJ ASC 10535	state-of-the-art FZJ ASC	
Z2_186	FZJ ASC 10514	state-of-the-art FZJ ASC	

6.3 Indices

6.3.1 Symbols

Symbol	Description	Unit
ASR_{anode}	overall anode polarisation resistance ($ASR_{anode} = R_{1A} + R_{2A} + R_{3A}$)	$\Omega \cdot m^2$
B_{ohm}	material-specific prefactor	$S \cdot K/m^2$
c_{mc}	concentration of oxygen lattice sites	mol/m^3
c_O	is the concentration of oxygen ions	mol/m^3
$D_{bulk,i}$	bulk diffusion coefficient of gas component i	m^2/s
D_i^{eff}	effective diffusion coefficient of gas component i	m^2/s
$D_{Knudsen,i}$	Knudsen diffusion coefficient of gas component i	m^2/s
$D_{mol,i}$	molecular diffusion coefficient of gas component i	m^2/s
D^{δ}	chemical diffusion coefficient	m^2/s
$E_{act,an}$	activation energy of anodic exchange current density	J/mol
$E_{act,cat}$	activation energy of cathodic exchange current density	J/mol
$E_{act,ohm}$	activation energy of ohmic losses	J/mol
F	Faraday constant	C/mol
f	frequency	Hz
f_{max}	characteristic frequency (summit frequency)	Hz
$g(x)$	distribution function of relaxation times (DRT) with $x = \ln(\omega/\omega_0)$	$\Omega \cdot s$
I_{load}	bias current	A
$i(t)$	sinusoidal current of small amplitude	A
j	current density (or imaginary unit)	A/m^2
$j_{0,an}$	anodic exchange current density	A/m^2
$j_{0,cat}$	cathodic exchange current density	A/m^2
k^{δ}	chemical surface exchange coefficient	m/s

L_{an}	anode thickness	m
L_{cat}	cathode thickness	m
M_i	molar mass of gas component i	kg/mol
n_e	number of exchanged electrons	-
n_Q	exponent of CPE impedance expression	-
n_W	exponent of G-FLW impedance expression	-
P	absolute atmospheric pressure in the gas channel	atm
P_0	conversion factor from [atm] to [Pa]. P_0 = 101330 Pa/atm	Pa/atm
$pH_{2,an}$	hydrogen partial pressure at the anode	atm
$pH_{2,an}^{TPB}$	hydrogen partial pressure at the three-phase boundary of the anode	atm
pH_2O_{an}	water partial pressure at the anode	atm
$pH_2O_{an}^{TPB}$	water partial pressure at the three-phase boundary of the anode	atm
pO_2	oxygen partial pressure	atm
$pO_{2,cat}$	oxygen partial pressure at the cathode	atm
$pO_{2,cat}^{TPB}$	oxygen partial pressure at the three-phase boundary of the cathode	atm
ps	particle size	m
R	universal gas constant	J/mol·K
R_{chem}	characteristic resistance of Gerischer element	Ω
R_0, R_{ohm}	overall (area specific) ohmic resistance	Ω·m²
R_{pol}	overall (area specific) polarisation resistance	Ω·m²
R_W	$\omega \rightarrow 0$ limit of $\underline{Z}_{G\text{-}FLW}(\omega)$.	Ω
$r_{Por,el}$	mean pore radius of the electrode	m
T	temperature	K or °C
t_{chem}	characteristic time constant of Gerischer element	s
T_W	characteristic time constant of G-FLW element (corresponds to l_d^2/D_i^{eff} with l_d the effective diffusion thickness and D_i^{eff} the effective diffusion coefficient of the diffusing species i)	s

$u(t)$	sinusoidal voltage response	V
U_0	theoretical standard cell voltage	V
U_{cell}	cell voltage (operating voltage)	V
U_N	Nernst voltage	V
U_{OCV}	open-circuit voltage	V
U_{th}	theoretical cell voltage	V
$\underline{Z}_{cell}$	generic internal cell impedance	Ω
$\underline{Z}_G$	impedance of a Gerischer element	Ω
$\underline{Z}_{G\text{-}FLW}$	impedance of a G-FLW element	Ω
$\underline{Z}_{RQ}$	impedance of a RQ element	Ω
Δ	deviation	%
$\Delta G(T)$	temperature dependent Gibbs free energy	J/mol
$\Delta G_0(T)$	temperature dependent standard free energy	J/mol
α_{an}	charge transfer coefficient of the anode	-
α_{cat}	charge transfer coefficient of the cathode	-
β	fuel utilization / humidification	%
γ_{an}	prefactor of the anodic exchange current density	A/m²
γ_{cat}	prefactor of the cathodic exchange current density	A/m²
$\chi(\tau)$	distribution function of relaxation times (DRT)	Ω/s
γ_{TD}	thermodynamic enhancement factor	-
δ	fraction of oxygen vacancies	-
$\varepsilon, \varepsilon_p$	volumetric porosity	-
$\eta_{act,an}$	activation overpotential at the anode	V
$\eta_{act,cat}$	activation overpotential at the cathode	V
$\eta_{conc,an}$	concentration overpotential at the anode	V
$\eta_{conc,cat}$	concentration overpotential at the cathode	V
η_{ohm}	ohmic overpotential	V

σ	conductivity	S/m
σ_{ij}	average collision diameter	Å
τ	(generic) relaxation time	s
τ_{RQ}	characteristic time constant of a RQ-element	s
τ_s	solid phase tortuosity	-
$\tau_{tortuosity}$	gas phase tortuosity	-
ψ_{an}	structural parameter of the anode	-
ψ_{cat}	structural parameter of the cathode	-
Ω_D	collision integral	-
ω	angular frequency	s^{-1}

6.3.2 Abbreviations

8YSZ	yttria-stabilised zirconia (8 mol% Y_2O_3-doped ZrO_2)
AFL	anode functional layer
ASC	anode supported cell
ASR	area specific resistance
CNLS	complex nonlinear least squares
CPE	constant phase element
DRT	distribution of relaxation times
EB-PVD	electron-beam physical vapour deposition
ECM	equivalent circuit model
EIS	electrochemical impedance spectroscopy
e.m.f.	electromotoric force
FEM	finite element method
FIB	focused ion beam
FRA	frequency response analyser
FZJ	Forschungszentrum Jülich
GDC	Gd-doped CeO_2
G-FLW	generalised finite length Warburg
IT-SOFC	intermediate temperature solid oxide fuel cell
I-U	current-voltage
IWE	Institute of Materials for Electrical and Electronical Engineering
L58SCF	$La_{0.58}Sr_{0.4}Co_{0.2}Fe_{0.8}O_{3-\delta}$
L60SCF	$La_{0.60}Sr_{0.4}Co_{0.2}Fe_{0.8}O_{3-\delta}$
L68SCF	$La_{0.68}Sr_{0.3}Co_{0.2}Fe_{0.8}O_{3-\delta}$
LSCF	$(La_x,Sr_{1-x})(Co_y,Fe_{1-y})O_{3-\delta}$
LSF	$(La_x,Sr_{1-x})Fe_{1-y}O_{3-\delta}$ here: $La_{0.68}Sr_{0.3}FeO_{3-\delta}$ $La_{0.6}Sr_{0.4}FeO_{3-\delta}$
L60SF	$La_{0.6}Sr_{0.4}FeO_{3-\delta}$

LSM	$La_{0.65}Sr_{0.3}MnO_{3-\delta}$
MFC	mass flow controller
MIEC	mixed ionic-electronic conducting
Ni/YSZ	nickel/yttria-stabilised zirconia
NLS	nonlinear least squares
OCV	open circuit voltage
Q	constant phase element (see CPE)
R	resistor
RC	resistor R connected in parallel with a capacitance C
RQ	resistor R connected in parallel with a constant phase element Q
SEM	scanning electron microscopy
SOFC	solid oxide fuel cell
TEM	transmission electron microscopy
TPB	triple phase boundary

6.4 List of Figures

6.5 List of Tables

6.6 Supervised Diploma Theses and Study Projects

- Sandrine Ngo-Dinh, „Simulation und Modellierung des dynamischen Verhaltens einer SOFC-Einzelzelle", Diploma Thesis, IWE, Universität Karlsruhe (TH), 2009.

- Alexander Kromp, „Modellbildung und Simulation der internen Reformierung an SOFC-Anoden bei Betrieb mit Kohlenwasserstoffhaltigen Brenngasen", Diploma Thesis, IWE, Universität Karlsruhe (TH), 2008.

- Yannick Apel, „Modellierung und Simulation des Strom- Spannungsverhalten von anodengestützten SOFC-Einzelzellen", Diploma Thesis, IWE, Universität Karlsruhe (TH), 2008.

- Michael Schumacher, „Elektrochemische Untersuchungen an SOFC-Anoden bei Betrieb mit regenerativen Brenngasen aus hydrothermaler Vergasung", Diploma Thesis, IWE, Universität Karlsruhe (TH), 2008.

- Lennart Luckert, „Betriebsverhalten der SOFC mit Biogas", Study Projekt, IWE, Universität Karlsruhe (TH), 2008.

- Michael Kornely, „Einfluss der Flowfield-Geometrie auf die Leistungsfähigkeit anodengestützter SOFC-Einzelzellen", Diploma Thesis, IWE, Universität Karlsruhe (TH), 2007.

- Vincent Weynandt and Yannick Apel, „Erarbeitung und Aufbau der Versuche für ein Brennstoffzellen und Batterien Praktikum", Team Study Projekt, IWE, Universität Karlsruhe (TH), 2007.

6.7 Own Publications

6.7.1 Publications

- V. Sonn, A. Leonide and E. Ivers-Tiffée, "An Impedance Study of Ni/YSZ and Ni/ScSZ Cermet Anodes in a Broad Range of Operating Conditions", in J. A. Kilner and U. Bossel (Eds.), Proceedings of the 7th European Solid Oxide Fuel Cell Forum, pp. P0723-164 (2006).

- A. Leonide, V. Sonn, A. Weber and E. Ivers-Tiffée, "Evaluation and Modelling of the Cell Resistance in Anode Supported Solid Oxide Fuel Cells", *ECS Trans.*, **7**, pp. 521-531 (2007).

- V. Sonn, A. Leonide and E. Ivers-Tiffée, "Towards Understanding the Impedance Response of Ni/YSZ Anodes", *ECS Trans.*, **7**, pp. 1363-1372 (2007).

- A. Leonide, V. Sonn, A. Weber and E. Ivers-Tiffée, "Evaluation and modeling of the cell resistance in anode-supported solid oxide fuel cells", *J. Electrochem. Soc.,* **155**, pp. B36-B41 (2008).

- V. Sonn, A. Leonide and E. Ivers-Tiffée, "Combined Deconvolution and CNLS Fitting Approach Applied on the Impedance Response of Technical Ni/8YSZ Cermet Electrodes", *J. Electrochem. Soc.,* **155**, pp. B675-B679 (2008).

- A. Leonide, S. Ngo Dinh, A. Weber and E. Ivers-Tiffée, "Performance limiting factors in anode supported SOFC", in R. Steinberger-Wilckens and U. Bossel (Eds.), Proceedings of the 8th European Solid Oxide Fuel Cell Forum, p. A0501 (2008).

- E. Ivers-Tiffée, H. Timmermann, A. Leonide, N. H. Menzler and J. Malzbender, "Methane reforming kinetics, carbon deposition, and redox durability of Ni/8 yttria-stabilised zirconia (YSZ) anodes", in W. Vielstich, H. Yokokawa, and H. A. Gasteiger (Eds.), Handbook of Fuel Cells - Fundamentals, Technology and Applications, Vol. 6, Chichester: John Wiley & Sons Ltd, pp. 933-956 (2009).

- A. Leonide, Y. Apel and E. Ivers-Tiffée, "SOFC Modeling and Parameter Identification by means of Impedance Spectroscopy", *ECS Trans.,* **19**, pp. 81-109 (2009).

- M. Kornely, A. Leonide, A. Weber and E. Ivers-Tiffée, "Impact of Flowfield Design on Solid Oxide Fuel Cell Performance", *ECS Trans.,* **25**, pp. 815-824 (2009).

- A. Utz, H. Störmer, A. Leonide, A. Weber and E. Ivers-Tiffée, "Degradation Effects of Ni Patterned Anodes in H2/H2O Atmosphere", *ECS Trans.* **25**, pp. 2013-2021 (2009).

- D. Klotz, A. Leonide and E. Ivers-Tiffée, "Recovery of Anode Performance by Reverse Current Treatment", *ECS Trans.* **25**, pp. 2049-2056 (2009).

- C. Endler, A. Leonide, A. Weber, F. Tietz and E. Ivers-Tiffée, "Long-Term Study of MIEC Cathodes for intermediate temperature Solid Oxide Fuel Cells", *ECS Trans.,* **25**, pp. 2381-2390 (2009).

- A. Leonide, B. Rüger, A. Weber, W. A. Meulenberg and E. Ivers-Tiffée, "Performance Study of Alternative $(La,Sr)FeO_3$-δ and $(La,Sr)(,Fe)O_3$-δ MIEC Cathode Compositions", *ECS Trans.* **25**, pp. 2487-2496 (2009).

- A. Leonide, B. Rüger, A. Weber, W. A. Meulenberg and E. Ivers-Tiffée, "Impedance Study of Alternative $(La,Sr)FeO_3$-δ and $(La,Sr)(,Fe)O_3$-δ MIEC Cathode Compositions", *J. Electrochem. Soc.,* **157**, pp. B234-B239 (2010).

- C. Endler, A. Leonide, A. Weber, F. Tietz, and E. Ivers-Tiffée, "Time-Dependent Electrode Performance Changes in Intermediate Temperature Solid Oxide Fuel Cells", *J. Electrochem. Soc.*, **157**, pp. B292-B298 (2010).

6.7.2 Conference Contributions

- V. Sonn, A. Leonide, E. Ivers-Tiffée, "An Impedance Study of Ni/YSZ and Ni/ScSZ Cermet Anodes in a Broad Range of Operating Conditions", 7th EUROPEAN SOFC FORUM (Lucerne, Switzerland), 03.07. - 07.07.2006.

- V. Sonn, A. Leonide, E. Ivers-Tiffée, A. Weber, "Towards Understanding the Impedance Response of Ni-YSZ Anodes", SOFC X (Nara, Japan), 03.06. - 08.06.2007.

- A. Leonide, V. Sonn, A. Weber, E. Ivers-Tiffée, "Evaluation and Modeling of the Cell Resistance in Anode Supported Solid Oxide Fuel Cells", SOFC X (Nara, Japan), 03.06. - 08.06.2007.

- A. Leonide, A. Weber, E. Ivers-Tiffée, "Diffusion Limitations in SOFC Anode Cermet Structures", 16th International Conference on Solid State Ionics (SSI-16) (Shanghai, China), 01.07.- 06.07.2007.

- A. Leonide, V. Sonn, A. Weber, E. Ivers-Tiffée, "Polarisation Effects in Anode-Supported Solid Oxide Fuel Cells", Euromat (Nürnberg, Germany), 10.09. - 13.09.2007.

- B. Rüger, T. Diepolder, A. Leonide, M. Kornely, E. Ivers-Tiffée, "Combined Experimental and Modelling Study for a Variation of Flow Field Geometry", 5th Symposium on Fuel Cell Modelling and Experimental Validation (Winterthur, Switzerland), 11.03. - 12.03.2008.

- A. Weber, A. Leonide, V. Sonn, E. Ivers-Tiffée, "Analysis of Anode Supported SOFCs by Impedance Spectroscopy", ETH Seminar (Zürich, Switzerland), 24.04. - 24.04.2008.

- B. Rüger, T. Diepolder, A. Leonide, M. Kornely, E. Ivers-Tiffée, "SOFC Single Cell Flow Field Modelling and Experimental Validation/Evaluation", 11th UECT Ulm ElectroChemical Talks 2008 (Ulm, Germany), 10.06. - 12.06.2008.

- A. Weber, T. Diepolder, B. Rüger, A. Leonide, M. Kornely, E. Ivers-Tiffée, "Combined Experimental and Modelling Study for a Variation of Flow Field Geometry", 2nd Mini Symposium on Solid Oxide Fuel Cells (Karlsruhe, Germany), 27.06. - 27.06.2008.

- A. Leonide, S. Ngo Dinh, A. Weber, E. Ivers-Tiffée, "Performance Limiting Factors in Anode Supported SOFC", 8th EUROPEAN SOFC FORUM (Lucerne, Switzerland), 30.06. - 04.07.2008.

- A. Leonide, A. Weber, E. Ivers-Tiffée, X.W. Huang, R. Reimert, N. Boukis, E. Dinjus, "SOFC für regenerative Brennstoffe aus hydrothermaler Vergasung", f-cell 2008 (Stuttgart, Deutschland), 29.09. - 30.09.2008.

- A. Weber, A. Leonide, V. Sonn, E. Ivers-Tiffée, "Electrochemical Characterization of Solid Oxide Fuel Cells by Impedance Spectroscopy", Impedance Spectroscopy - A Versatile Tool in Electrochemistry (Eindhoven University of Technology, The Netherlands), 14.11. - 14.11.2008.

- A. Leonide, Y. Apel, A. Weber, E. Ivers-Tiffée, "Performance Simulation of an Anode-supported SOFC by means of Detailed Impedance Analysis", ZING Electrochemistry Conference 2009 (Playa del Carmen, Mexico), 08.02. - 11.02.2009.

- A. Utz, V. Sonn, A. Leonide, H. Störmer, D. Gerthsen, A. Weber, E. Ivers-Tiffée, "Ni/YSZ Patterned Anodes: Microstructure and Electrochemical Properties", Bunsentagung (Köln, Germany), 21.05. - 23.05.2009.

- A. Leonide, Y. Apel, E. Ivers-Tiffée, "SOFC Modeling and Parameter Identification by means of Impedance Spectroscopy", 215th Meeting of The Electrochemical Society (San Francisco, USA), 24.05. - 29.05.2009.

- A. Leonide, Y. Apel, A. Weber, E. Ivers-Tiffée, "Performance Simulation of an Anode-supported SOFC by Means of Detailed Impedance Analysis", 8th Pacific Rim Conference on Ceramic and Glass Technology (Vancouver, Canada), 31.05. - 05.06.2009.

- C. Endler, A. Leonide, B. Rüger, A. Weber, E. Ivers-Tiffée, "Time-Dependent Study of k^{δ}- and D^{δ}-Values of Mixed Ionic-Electronic Conducting Cathodes", 17th International Conference on Solid State Ionics (SSI-17) (Toronto, Canada), 28.06. - 03.07.2009.

- C. Endler, A. Leonide, A. Weber, E. Ivers-Tiffée, F. Tietz, "Long-Term Study of MIEC Cathodes for intermediate temperature Solid Oxide Fuel Cells", SOFC XI (Vienna, Austria), 04.10. - 09.10.2009.

- M. Kornely, A. Leonide, A. Weber, E. Ivers-Tiffée, "Impact of Flowfield Design on Solid Oxide Fuel Cell Performance", SOFC XI (Vienna, Austria), 04.10. - 09.10.2009.

- A. Leonide, B. Rüger, A. Weber, W.A. Meulenberg, E. Ivers-Tiffée, "Performance Study of Alternative MIEC Cathode Compositions", SOFC XI (Vienna, Austria), 04.10. - 09.10.2009.

- A. Utz, H. Störmer, A. Leonide, A. Weber, E. Ivers-Tiffée, "Degradation Effects of Ni Patterned Anodes in H2/H2O Atmosphere", SOFC XI (Vienna, Austria), 04.10. - 09.10.2009.

- D. Klotz, A. Leonide, E. Ivers-Tiffée, "Recovery of Anode Performance by Reverse Current Treatment", SOFC XI (Vienna, Austria), 04.10. - 09.10.2009.

7   Reference List

1. P. Timakul, S. Jinawath, and P. Aungkavattana, *Ceram. Int.*, **34**, 867 (2008).

2. J.H. Song, N.M. Sammes, S.I. Park, S. Boo, H.S. Kim, H. Moon, and S.H. Hyun, *J. Fuel Cell Sci. Technol.*, **5**, 021003-1 (2008).

3. S.C. Singhal, *Solid State Ionics*, **152**, 405 (2002).

4. A.C. Müller, J.R. Opfermann, and E. Ivers-Tiffée, *Thermochim. Acta*, **414**, 11 (2004).

5. A. Mai, V.A.C. Haanappel, F. Tietz, and D. Stöver, *Solid State Ionics*, **177**, 2103 (2006).

6. J.R. Macdonald, *Impedance spectroscopy*, Wiley Interscience, New York (1987).

7. B.A. Boukamp, *Solid State Ionics,* **20**, 31 (1986).

8. P. Holtappels, and U. Stimming, *Solid Oxide Fuel Cells (SOFC)*, in W. Vielstich et al. (Eds.), *Handbook of Fuel Cells: Fundamentals, Technology and Applications*, Vol. 1, Chichester, England: John Wiley & Sons Ltd., p. 335-354 (2003).

9. S.C. Singhal, and K. Kendall, *High Temperature Solid Oxide Fuel Cells*, Elsevier Ltd., New York (2003).

10. C. Peters, *Grain-Size Effects in Nanoscaled Electrolyte and Cathode Thin Films for Solid Oxide Fuel Cells*, Ph.D. Thesis, Universitätsverlag Karlsruhe, Karlsruhe (2009).

11. E. Ivers-Tiffée, *Brennstoffzellen und Batterien*, lecture notes, Institut für Werkstoffe der Elektrotechnik (IWE), Karlsruher Institut für Technologie (KIT), Germany (2009).

12. M.E. Orazem, and B. Tribolett, *Electrochemical Impedance Spectroscopy*, John Wiley & Sons, New York (2008).

13. A.J. Bard, and L.R. Faulkner, *Electrochemical Methods*, John Wiley & Sons, New York (2001).

14. S. Primdahl, and M. Mogensen, *J. Electrochem. Soc.*, **146**, 2827 (1999).

15. J. Kim, A.V. Virkar, K. Fung, K. Mehta, and S.C. Singhal, *J. Electrochem. Soc.,* **146**, 69 (1999).

16. E. Ivers-Tiffée, and A. V. Virkar, *Electrode Polarisations*, in S.C. Singhal and K. Kendall (Eds.), *High Temperature Solid Oxide Fuel Cells - Fundamentals, Design and Applications*, Oxford, UK: Elsevier Ltd, p. 229-260 (2003).

17. A. Weber, *Entwicklung und Charakterisierung von Werkstoffen und Komponenten für die Hochtemperatur-Brennstoffzelle SOFC*, ph.D. Thesis, Universität Karlsruhe (TH), Karlsruhe, Germany (2002).

18. A. Müller, *Mehrschicht-Anode für die Hochtemperatur-Brennstoffzelle (SOFC)*, ph.D. Thesis, Universität Karlsruhe (TH), Karlsruhe, Germany (2005).

19. H. Schichlein, *Experimentelle Modellbildung für die Hochtemperatur-Brennstoffzelle SOFC*, ph.D. Thesis, Universität Karlsruhe (TH), Verlag Mainz, Aachen (2003).

20. V. Brichzin, J. Fleig, H.-U. Habermeier, G. Cristiani, and J. Maier, *Solid State Ionics*, **152**–**153**, 499–507 (2002).

21. S.B. Adler, *Solid State Ionics*, **135**, 603 (2000).

22. S.B. Adler, J.A. Lane, and B.C.H. Steele, *J. Electrochem. Soc.*, **143**, 3554 (1996).

23. B. Rüger, *Mikrostrukturmodellierung von Elektroden für die Festelektrolyt-brennstoffzelle*, Ph.D Thesis, Universitätsverlag Karlsruhe, Karlsruhe (2009).

24. M. Søgaard, P. Vang Hendriksen, and M. Mogensen, *J. Solid State Chem.*, **180**, 1489 (2007).

25. D. Johnson, "ZPlot, ZView Electrochemical Impedance Software, Version 2.3b", Scribner Associates, Inc. (2000).

26. A. Leonide, Diplomarbeit (Master Thesis), Institut für Werkstoffe der Elektrotechnik, Universität Karlsruhe (TH), Germany (2005).

27. M. Mogensen, and P. V. Hendriksen, in *High Temperature Solid Oxide Fuel Cells. Fundamentals, Design and Applications*, S. C. Singhal and K. Kendall, Editors, Elsevier Advanced Technology (2003).

28. H. Schichlein. A.C. Müller, M. Voigts, A. Krügel, and E. Ivers-Tiffée, *J. Appl. Electrochem.*, **32**, 875 (2002).

29. H. Schäfer, and E. Sternin, *Phys. Can.*, **3**/**4**, 77 (1997).

30. A.K. Louis, *Invers und Schlecht gestellte Probleme*, Teubner, Stuttgart (1989).

31. A.N. Tikhonov, and V.Y. Arsenin, *Solution of ill-posed problems*, J. Wiley & Sons, New York (1977).

32. A.N. Tikhonov, A.V. Goncharsky, V.V. Stepanov, and A.G. Yagola, *Numerical methods for the solution of ill-posed problems*, Kluwer, Dordrecht, (1995).

33. Service group Scientific Data Processing at Freiburg Materials Research Center, "User Manual FTIKREG: A program for the solution of Fredholm integral equations of the first kind", (2008).

34. R.M. Fuoss, and J.G. Kirkwood, *J. Am. Chem. Soc.*, **63**, 385 (1941).

35. D. Stöver, H.P. Buchkremer, and J.P.P. Huijsmans, in *Handbook of Fuel Cells, Volume 4: Fuel Cell Technology and Applications Part 2*, W. Vielstich, A. Lamm, H.A. Gasteiger, Editors, pp. 1013-1031, John Wiley and Sons Ltd., Chichester, UK (2003).

36. D. Stöver, H.P. Buchkremer, F. Tietz, and N.H. Menzler, in *5th European Solid Oxide Fuel Cell Forum*, J. Huijsmans Editor, pp. 1–9, European Fuel Cell Forum, Oberrohrdorf, Switzerland (2002).

37. M. Becker, A. Mai, E. Ivers-Tiffée, and F. Tietz, in *Solid Oxide Fuel Cells IX*, S.C. Singhal and J. Mizusaki, Editors, PV 2005-07, p. 514, The Electrochemical Society Proceeding Series, Pennington, NJ (2005).

38. B.A. Boukamp, *J. Electrochem. Soc.*, **142**, 1885 (1995).

39. B.A. Boukamp, *Solid State Ionics*, **169**, 65 (2004).

40. A. Leonide, V. Sonn, A. Weber, and E. Ivers-Tiffée, *J. Electrochem. Soc.*, **155**, B36 (2008).

41. S.B. Adler, *Chem. Rev.*, **104**, 4791 (2004).

42. A. Esquirol, N.P. Brandon, J.A. Kilner, and M. Mogensen, *J. Electrochem. Soc.*, **151**, A1847 (2004).

43. T. Ackmann, L.G.J. de Haart, W. Lehnert, and D. Stolten, *J. Electrochem. Soc.*, **150**, 783 (2003).

44. V. Sonn, A. Leonide, and E. Ivers-Tiffée, *J. Electrochem. Soc.*, **155**, B675 (2008).

45. A. Leonide, S. Ngo Dinh, A. Weber, and E. Ivers-Tiffée, in *8th European Solid Oxide Fuel Cell Forum*, R. Steinberger-Wilckens, Editor, p. A0501, European Fuel Cell Forum, Lucerne, Switzerland, June 30-July 4 (2008).

46. J. Maier, *Solid State Ionics*, **112**, 197 (1998).

47. A. Esquirol, J. Kilner, and N. Brandon, *Solid State Ionics*, **175**, 63 (2004).

48. B.C.H. Steele, and J.-M. Bae, *Solid State Ionics*, **106**, 255 (1998).

49. J.A. Lane, P.H. Middleton, H. Fox, B.C.H. Steele, and J.A. Kilner, in *Second International Symposium on Ionic and Mixed Conducting Ceramics*, T.A. Ramanarayanan, W.L. Worrel, H.L. Tuller, Editors, PV 94-12, p. 489, The Electrochemical Society Proceedings Series, Pennington, NJ (1994).

50. B. Rüger, A. Weber, and E. Ivers-Tiffée, *ECS Trans.*, **7**, 2065 (2007).

51. S.R. Wang, M. Katsuki, M. Dokiya, and T. Hashimoto, *Solid State Ionics*, **159**, 71 (2003).

52. D. Mantzavinos, A. Hartley, I.S. Metcalfe, and M. Sahibzada, *Solid State Ionics*, **134**, 103 (2000).

53. H.J.M. Bouwmeester, M.W. den Otter, and B.A. Boukamp, *J. Solid State Electrochem.*, **8**, 599 (2004).

54. M.W. den Otter, Ph.D. Thesis, Universiteit Twente, Enschede (2000).

55. M. Søgaard, P.V. Hendriksen, T. Jacobsen, and M. Mogensen, in 7th *European Solid Oxide Fuel Cell Forum*, J.A. Kilner, Editor, p. 1, European Fuel Cell Forum, Lucerne, Switzerland, July 3-7 (2006).

56. P. Ried, E. Bucher, W. Preis, W. Sitte, and P. Holtappels., *ECS Trans.*, **7**, 1217 (2007).

57. N.H. Menzler, personal communication (2008).

58. *The CRC Handbook of Solid State Electrochemistry*, P. Gellings, and H. Bouwmeester, Editors, CRC, Boca Raton, FL (1997).

59. M. Søgaard, P.V. Hendriksen, M. Mogensen, F.W. Poulsen, and E. Skou, *Solid State Ionics*, **177**, 3285 (2006).

60. M. Lankhorst, Ph.D. Thesis, Universiteit Twente, Enschede (1997).

61. M. Søgaard, P.V. Hendriksen, and F.W. Poulsen, in *Proceedings of the 26th Risø International Symposium on Materials Science 1*, 355 (2005).

62. B.T. Dalslet, M. Søgaard, and P. Vang Hendriksen, *J. Electrochem. Soc.*, **154**, B1276 (2007).

63. M. Søgaard, Ph.D. Thesis, Risø National Laboratory, Roskilde, Denmark (2006).

64. B. Rüger, J. Joos, A. Weber, T. Carraro, and E. Ivers-Tiffée, *ECS Trans.*, **25**, 1211 (2009).

65. J.R. Wilson, J.S. Cronin, S. Rukes, A. Duong, D. Mumm, and S. Barnett, *ECS Trans.*, **25**, 2283 (2009).

66. H. Galinski, J. Reuteler, J.L.M. Rupp, A. Bieberle-Hütter, and L.J. Gauckler, *ECS Trans.*, **25**, 2057 (2009).

67. C. Endler, A. Leonide, A. Weber, F. Tietz, and E. Ivers-Tiffée, *J. Electrochem. Soc.*, **157**, B292 (2010).

68. F.S. Baumann, ph.D. Thesis, Max Planck Institut für Festkörperforschung, Stuttgart (2006).

69. V.G. Sathe, S.K. Paranjpe, V. Siruguri, and A.V. Pimpale, *J. Phys. Condens. Matter*, **10**, 4045 (1998).

70. M.V. Patrakeev, I.A. Leonidov, V.L. Kozhevnikov, and K.R. Poeppelmeier, J. *Solid State Chem.*, **178**, 921 (2005).

71. J.E. ten Elshof, M.H.R. Lankhorst, and H.J.M. Bouwmeester, *J. Electrochem. Soc.*, **144**, 1060 (1997).

72. S. Uhlenbruck, T. Moskalewicz, N. Jordan, H.-J. Penkalla, and H.P. Buchkremer, *Solid State Ionics*, **180**, 418 (2009).

73. A.V. Virkar, J. Chen, C.W. Tanner, and J.W. Kim, *Solid State Ionics*, **131**, 189 (2000).

74. P. Aguiar, C.S. Adjiman, and N.P. Brandon, *J. Power Sources*, **138**, 120 (2004).

75. A.V. Akkaya, *Int. J. Energy Res.*, **31**, 79 (2007).

76. S. Campanari, and P. Iora, *J. Power Sources*, **132**, 113 (2004).

77. Y. Wang, F. Yoshiba, T. Watanabe, and S.L. Weng, *J. Power Source*s, **170**, 101 (2007).

78. D.A. Noren, and M.A. Hoffman, *J. Power Sources*, **152**, 175 (2005).

79. W. Jiang, R.X. Fang, J.A. Khan, and R.A. Dougal, *J. Power Sources*, **162**, 316 (2006).

80. D. Sanchez, R. Chacartegui, A. Munoz, and T. Sanchez, *J. Power Sources*, **160**, 1074 (2006).

81. M. Ni, M.K.H. Leung, and D.Y.C. Leung, *Int. J. Hydrogen Energy*, **32**, 2305 (2007).

82. T. Yamamura, H. Tagawa, T. Saito, J. Mizusaki, K. Kamitani, K. Hirano, S. Ehara, T. Takagi, Y. Hishinuma, H. Sasaki, T. Sogi, Y. Nakamura, and K. Hashimoto, in *Solid Oxide Fuel Cells IV*, M. Dokiya, O. Yamamoto, H. Tagawa and S.C. Singhal, Editors, PV 95-1, p. 741, The Electrochemical Society Proceeding Series, Pennington, NJ (1995).

83. P. Costamagna, A. Selimovic, M. Del Borghi, and G. Agnew, *Chem. Eng. J.*, **102**, 61 (2004).

84. P. Costamagna, and K. Honegger, *J. Electrochem. Soc.*, **145**, 3995 (1998).

85. H. Schichlein, M. Feuerstein, A.C. Müller, A. Weber, A. Krügel, and E. Ivers-Tiffée, in *Solid Oxide Fuel Cells VI*, S.C. Singhal and M. Dokiya, Editors, PV 99-19, pp. 1069-1077, The Electrochemical Society Proceeding Series, Pennington, NJ (1999).

86. P. Ried, C. Lorenz, A. Bronstrup, T. Graule, N.H. Menzler, W. Sitte, and P. Holtappels, *J. Eur. Ceram. Soc.*, **28**, 1801 (2008).

87. T.H. Etsell, and S.N. Flengas, *Chem. Rev.*, **70**, 339 (1970).

88. A. Tsoga, A. Naoumidis, W. Jungen, and D. Stöver, *J. Eur. Ceram. Soc.*, **19**, 907 (1999).

89. E. Hernandez-Pacheco, D. Singh, P.N. Hutton, N. Patel, and M.D. Mann, *J. Power Sources*, **138**, 174 (2004).

90. E.A. Mason, and A.P. Malinauskas, *Gas Transport in Porous Media: The Dusty Gas Model*, Elsevier, Amsterdam (1983).

91. R. Jackson, *Transport in Porous Catalysts*, Elsevier, Amsterdam (1977).

92. E.L. Cussler, *Diffusion: Mass Transfer in Fluid Systems*, Cambridge University Press, Cambridge (1995).

93. D.F. Fairbanks, and C.R. Wilke, *Ind. Eng. Chem.*, **42**, 471 (1950).

94. R. Reid, J. Prausnitz, and T. Sherwood, *The Properties of Gases and Liquids*, 3rd ed., p. 548, McGraw-Hill, New York (1977).

95. P. Fott, and G. Petrini, *Appl. Catal.*, **2**, 367 (1982).

96. J. Valus, and P. Schneider, *Appl. Catal.*, **1**, 355 (1981).

97. S.H. Chan, K.A. Khor, and Z.T. Xia, *J. Power Sources*, **93**, 130 (2001).

98. W. G. Bessler, *Solid State Ionics*, **176**, 997 (2005).

99. A. Bieberle, and L.J. Gauckler, *Solid State Ionics*, **146**, 23 (2002).

100. J. Mizusaki, H. Tagawa, T. Saito, T. Yamamura, K. Kamitani, K. Hirano, S. Ehara, T. Takagi, T. Hikita, M. Ippommatsu, S. Nakagawa, and K. Hashimoto, *Solid State Ionics*, **70**, 52 (1994).

101. J.B. Liu, A.C. , S. Paulson, and V.I. Birss, *Solid State Ionics*, **177**, 377 (2006).

102. H. Wendt, and G. Kreysa, *Electrochemical Engineering*, Springer, Berlin (1999).

103. P. Holtappels, L.G.J. de Haart, and U. Stimming, *J. Electrochem. Soc.*, **146**, 1620 (1999).

104. E. Achenbach, *J. Power Sources*, **49**, 333 (1994).

105. S. Primdahl, and M. Mogensen, *J. Electrochem. Soc.*, **144**, 3409 (1997).

106. B. de Boer, *SOFC Anode Hydrogen oxidation at porous nickel and nickel/yttriastabilised zirconia cermet electrodes*, ph.D. Thesis, Enschede, Netherlands (1998).

107. J. Geyer, H. Kohlmuller, H. Landes, and R. Stubner, in *Solid Oxide Fuel Cells V*, U. Stimming, S.C. Singhal, H. Tagawa, and W. Lehnert, Editors, PV 97-18, pp. 585-593, The Electrochemical Society Proceeding Series, Pennington, NJ (1997).

108. M. Brown, S. Primdahl, and M. Mogensen, *J. Electrochem. Soc.*, **147**, 475 (2000).

109. M. Sahibzada, S.J. Benson, R.A. Rudkin, and J.A. Kilner, *Solid State Ionics*, **115**, 285 (1998).

110. J.M. Bae, and B.C.H. Steele, *Solid State Ionics*, **106**, 247 (1998).

111. S. P. Jiang, *Solid State Ionics*, **146**, 1 (2002).

112. C. Peters, A. Weber, and E. Ivers-Tiffée, *J. Electrochem. Soc.*, **155**, B730 (2008).

113. P. Holtappels, L.G.J. de Haart, U. Stimming, I.C. Vinke, and M. Mogensen, *J. Appl. Electrochem.*, **29**, 561 (1999).

114. H.M. Xiao, T.L. Reitz, and M.A. Rottmayer, *J. Power Sources*, **183**, 49 (2008).

115. Y. Takeda, R. Kanno, M. Noda, Y. Tomida, and O. Yamamoto, *J. Electrochem. Soc.*, **134**, 2656 (1987).

116. D. Klotz, A. Weber, and E. Ivers-Tiffée, *ECS Trans.*, **25**, 1331 (2009)

117. F. Tietz, A. Mai, and D. Stöver, *Solid State Ionics*, **179**, 1509 (2008).

118. L. Dieterle, D. Bach, R. Schneider, H. Störmer, D. Gerthsen, U. Guntow, E. Ivers-Tiffée, A. Weber, C. Peters, and H. Yokokawa, *J. Mater. Sci.*, **43**, 3135 (2008).

Interest in solid oxide fuel cells (SOFC), which combine potentially efficient energy production with flexible fuel composition, has significantly increased in the past few years. Amongst the most important development goals is, besides long-term stability, the single-cell performance which is limited by three loss mechanisms: (i) ohmic losses, (ii) polarisation losses through gas diffusion, and (iii) losses by activation polarisation. However, to this day the progress for a further improvement of anode supported cells has been partly constrained by an incomplete understanding of the physical origin and share of the individual polarisation processes controlling the cell performance. In this regard the electrochemical impedance spectroscopy (EIS) is one of the most promising methods for unfolding complex electrochemical systems such as a SOFC.

Commonly the obtained impedance spectra are analysed by a Complex Nonlinear Least Squares (CNLS) approximation to a model function represented by an equivalent circuit. In this case the equivalent circuit model (ECM) needs to be defined a priori without any knowledge about the real number of polarisation processes contributing to the overall polarisation loss of the cell. This leads very often to a severe ambiguity of the adopted model.

To overcome that disadvantage an alternative approach for analysing impedance spectra has been used in this work. The ECM and the optimal starting parameters for the CNLS algorithm have been obtained by a pre-identification of the impedance response by calculating and analysing the corresponding distribution function of relaxation times (DRT).

The ECM obtained in this way is used to assess candidate cathode compositions with regard to the surface exchange kinetics and oxygen ion bulk diffusion. Furthermore, the ECM is able to deliver physical meaningful parameters for a zero-dimensional stationary model, which is valid for a wide operating range.